

Light-Matter Interactions in Quasi-Two-Dimensional Geometries

David James Lahneman

Dunkirk, Maryland

Master of Science, College of William & Mary, 2016

Bachelor of Science, Towson University, 2014

A Dissertation presented to the Graduate Faculty of The College of William &
Mary in Candidacy for the Degree of
Doctor of Philosophy

Department of Physics

College of William & Mary
August 2021

APPROVAL PAGE


This Dissertation is submitted in partial fulfillment of
the requirements for the degree of

Doctor of Philosophy




David James Lahneman


Approved by the Committee March 2021



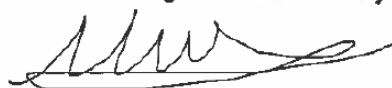
Committee Chair
M. Mumtaz Qazilbash, Associate Professor, Physics
College of William & Mary



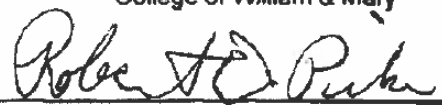
Henry Krakauer, Professor, Physics
College of William & Mary



Dennis Manos, CSX Professor, Physics and Applied Science
Vice-Provost for Research
College of William & Mary



Eugeny Mikhailov, Associate Professor, Physics
College of William & Mary



Robert D. Pike, Floyd Dewey Gottwald Sr. Professor, Chemistry
College of William & Mary

ABSTRACT

Emergent phenomena that occur at length scales smaller than approximately half the wavelength of light cannot be resolved by conventional optical techniques due to the Abbe diffraction limit. Scattering-type scanning near-field infrared microscopy (S-SNIM) can circumvent this diffraction limit allowing infrared spectroscopy at nano-scale dimensions independent of the wavelength. Additionally, there is enhanced surface sensitivity resulting from this nanoconfinement of infrared light. S-SNIM is uniquely suitable to study a diverse range of material properties inaccessible by far-field optics in the infrared such as the optical properties of ultrathin films as well as hybrid light matter surface waves called polaritons. Initially, this work describes a broadband infrared plasma light source that has been developed and implemented in our S-SNIM setup to realize broadband S-SNIM in the far- and mid-infrared. This system is then utilized to investigate propagating surface phonon polaritons (SPhPs) in bulk strontium titanate (STO). STO is a perovskite polar dielectric that has a uniquely broad range of the far-infrared in which it can support SPhPs while already having a diverse range of technologically advantageous properties. This work opens the door to envisage STO as a platform for perovskite-based broadband far-infrared and terahertz nano-photonics.

Finally, the insulator to metal transition (IMT) in ultrathin vanadium dioxide (VO_2) films is investigated. An IMT is an emergent characteristic of quantum materials. When the IMT occurs in materials with interacting electronic and lattice degrees of freedom, it is often difficult to determine if the energy gap in the insulating state is formed by Mott electron-electron correlations or by Peierls charge-density wave (CDW) ordering. To solve this problem, we investigate a representative material, VO_2 , which exhibits strong electron-electron interactions as well as CDW (Peierls) ordering. Ultrathin VO_2 films on rutile (001) TiO_2 substrates have been fabricated. These VO_2 films undergo the IMT without the CDW (Peierls) ordering. Infrared and optical measurements discover the Mott-Hubbard semiconductor gap of 0.6 eV in the rutile phase below $T_c \approx 306$ K. Above T_c , a Drude feature along with an increase in the optical conductivity due to a Mott IMT is observed. These results establish the route to a purely electronic IMT with profound implications for fundamental and applied studies of this phenomenon. Near-field infrared nano-imaging on this VO_2 film exhibits a percolative phase transition in the vicinity of T_c , a uniform fully metallic phase above T_c , and a uniformly insulating phase below T_c . Near-field infrared spectroscopy demonstrates an SPhP feature stemming primarily from the TiO_2 substrate. This SPhP feature is sensitive to the IMT in the ultrathin VO_2 film.

TABLE OF CONTENTS

Acknowledgements	iv
Dedications	v
Chapter 1. Introduction	1
1.1 Motivation for Infrared and Optical Spectroscopy	2
1.2 Strongly correlated electron systems	3
1.3 Infrared spectroscopy at nanometer length scales	4
1.4 Electromagnetic surface waves	7
1.5 Broadband sources for s-SNIM	8
1.6 Scope of the Dissertation	9
Chapter 2. Experimental Methods	11
2.1 Introduction	11
2.2 Far-field techniques	12
2.2.1 Fourier Transform Infrared (FTIR) Spectroscopy	12
2.2.2 Spectroscopic Ellipsometry	13
2.3 Near-field techniques	15
2.3.1 The Abbe-diffraction limit	15
2.3.2 Scattering-type scanning near-field infrared microscopy	17
2.3.3 Pseudo-heterodyne s-SNIM	21
2.3.4 Scattering-type scanning near-field infrared spectroscopy	24
Chapter 3. Broadband Near-field Infrared Spectroscopy with a High Temperature Plasma Light Source	27
3.1 Introduction	27
3.2 Experiment	31

3.2.1	Argon Plasma Light Source (APLS)	31
3.2.2	Broadband near-field infrared spectroscopy	36
3.3	Results with the APLS	40
3.4	APLS summary and outlook	44
3.5	Extending the APLS to the far-infrared	45
3.6	The laser sustained xenon plasma light source	49
3.7	The signal-to-noise comparison of the plasma sources	52
Chapter 4.	Far-infrared surface phonon polariton propagation in STO	55
4.1	Introduction	55
4.2	Experimental Method	62
4.3	Results & Discussion	65
4.4	Conclusion	72
Chapter 5.	Mott transition in the rutile insulator VO ₂ without Peierls ordering	73
5.1	Introduction	73
5.2	Materials & methods	76
5.3	Results & discussion	79
5.4	Conclusion	86
5.5	Continuing near-field study of ultrathin VO ₂	87
Chapter 6.	Conclusions & Outlook	91
	Appendices	94
	Appendix A: Near-field simulation methods	94
	Appendix B: Ultrathin VO ₂ film X-ray characterization	98
	Appendix C: Ultrathin VO ₂ film dielectric function	100
	Appendix D: Ultrathin VO ₂ film metallic layer analysis	101

ACKNOWLEDGEMENTS

I would like to express my sincerest gratitude to my advisor Prof. Mumtaz Qazilbash for the guidance, funding, mentorship, and continued motivation to see this project through to the end. I would also like to express gratitude to the many collaborators from all over the world I have had to joy to work with. I would like to thank my fellow graduate students I worked side by side with during my PhD including Patrick McArdle, Haoyue Jiang, Tyler Huffman, Zhen Xing, and Peng Xu. Thank you for all the help and good company during the many long experiments. I would like to express thanks to the many professors I have had the good fortune to learn from, most notably the members of my annual review committee for the helpful feedback on my projects over the years.

This PhD is dedicated to my mother, father, brother, sisters, and Elise.

Chapter 1:

Introduction

The purpose of the research conducted in this dissertation is to use infrared and optical photons to examine electronic and vibrational properties of exotic materials, especially in quasi-two-dimensional geometries. The main subjects of this dissertation are infrared and optical spectroscopy of an ultrathin film of a strongly correlated electron material vanadium dioxide (VO_2) and electromagnetic surface waves called surface phonon polaritons in strontium titanate (SrTiO_3 or STO). The structure of this chapter is to briefly describe and motivate how optical and infrared spectroscopy is an important method to study strongly correlated electron systems as well as systems that support electromagnetic surface waves. Then, due to limitations of far-field optics, provide motivation for scattering-type scanning near-field infrared microscopy (s-SNIM) in the mid- and far-infrared for studying light-matter interactions at nanometer lengths scales. Finally, the development of a broadband plasma light source will be motivated as a solution for tabletop s-SNIM.

1.1 Motivation for Infrared and Optical Spectroscopy

The interaction of photons and matter has been the natural way humans have navigated and observed our surroundings since long before the scientific method was developed. Using our eyes to resolve images across the visible spectrum is a form of spectroscopy allowing us to see leaves in the trees as green under white clouds in a blue sky. We have since been able to extend the spectrum, using scientific instrumentation, beyond the visible range of $\lambda \approx 380 \text{ nm} - 740 \text{ nm}$ to effectively the entire electromagnetic spectrum. Experimental investigation of the electromagnetic response of materials over a broad energy range allows access to the necessary energy scales to study both collective modes and elementary excitations. Photon spectroscopy on a material from the infrared through ultraviolet energy range can give the infrared lattice vibrations, metallic Drude response, insulating band gap, and optical interband transitions. This measurement alone yields information of the lattice dynamics and band structure together. In this dissertation, the far-field optical measurements are taken using a Fourier Transform Infrared (FTIR) spectrometer and a Spectroscopic Ellipsometer. Figure 1.1 shows the energy range covered by both of these instruments as well as indicating the relevant excitations each energy range contains.

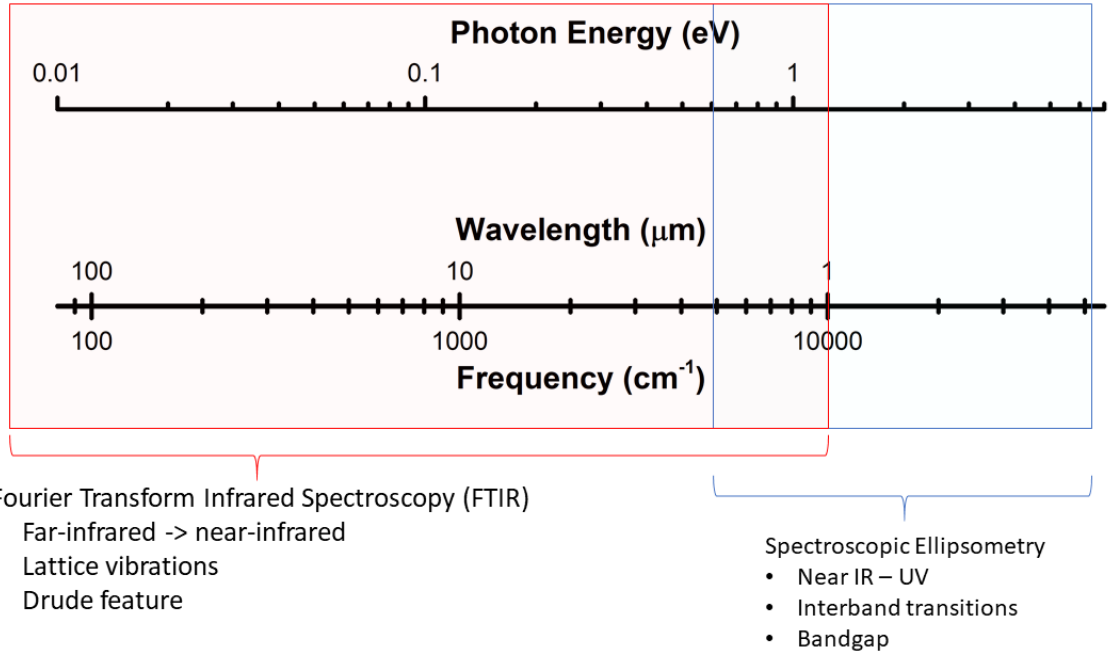


Fig. 1.1 Energy range of far-field spectroscopy discussed in this dissertation.

1.2 Strongly correlated electron systems

In the 1920's, the quantum mechanical description of electrons in solids called band theory, gave significant insight into distinctions between insulators and metals. Within this theory, descriptions of the electronic behavior of solids was made possible without the need to invoke the local electron interactions in the system. In the late 1930's, transition metal oxides such as NiO that were expected to be metallic from band theory were experimentally known to be insulators [1]. Mott and Peierls proposed that this insulating state was due to the strong coulomb interactions between electrons [2]. This proposal began the field of strongly correlated electron systems which, to this day, is a major field of condensed matter physics spanning many classes of emergent behavior including high- T_c .

superconductivity, colossal magneto-resistance, heavy electron fluids, and insulator-metal transitions [3].

The strongly correlated electron system discussed in this dissertation is VO₂, a 3d transition metal oxide that in bulk undergoes a insulator to metal transition at ~340 K while also undergoing a structural transition from insulating monoclinic to metallic rutile [4,5]. Due to the large energy range that optical and infrared spectroscopy can cover it is well suited to uncover the complex interplay of the structural and electronic degrees of freedom in this correlated system. Interestingly, around the transition temperature VO₂ exhibits phase coexistence at the nanoscale which can be seen in Fig. 1.2 [6]. Though far-field optical and infrared spectroscopy are well suited to investigate VO₂ in its fully uniform insulating and metallic states, another newer experimental technique is emerging as a method to probe optical constants at the nanoscale.

1.3 Infrared spectroscopy at nanometer length scales

Far-field optical and infrared spectroscopy are clearly a powerful method to extract the optical constants of materials over a broad energy range. However, there are limitations to this method which stem from the far-field nature of the experiment. Due to the wave nature of light, a measurement is limited to a spot size that is on the order of the wavelength of the photon which for infrared measurements is microns large. Many transition metal oxides exhibit nanoscale phase coexistence in the vicinity of their phase transition. Figure 1.2 shows VO₂ microcrystals and thin films in the vicinity of its insulator-to-metal transition (IMT). Each example shows

how nanoscale regions of the sample become metallic in the insulating bulk. Conventional far-field diffraction limited optics in the infrared would yield an area average over these domains not allowing a complete picture of the complex nanoscale physics. To properly study the strongly correlated physics of VO₂ in the vicinity of the transition it is necessary to probe these regions directly.

In the infrared, s-SNIM is a powerful scanning probe technique allowing infrared images to be obtained from a sample surface at a wavelength independent resolution on the order of tens of nanometers [7,8]. Another advantage of s-SNIM is its high surface sensitivity for materials when compared to the penetration depth for infrared wavelengths. With a suitable broadband source, S-SNIM can become the nanoscale analog to infrared FTIR allowing the acquisition of the optical constants of materials over a broad energy range to extract the lattice dynamics along with Drude behavior in the bandgap energy range to allow a local picture of the IMT.

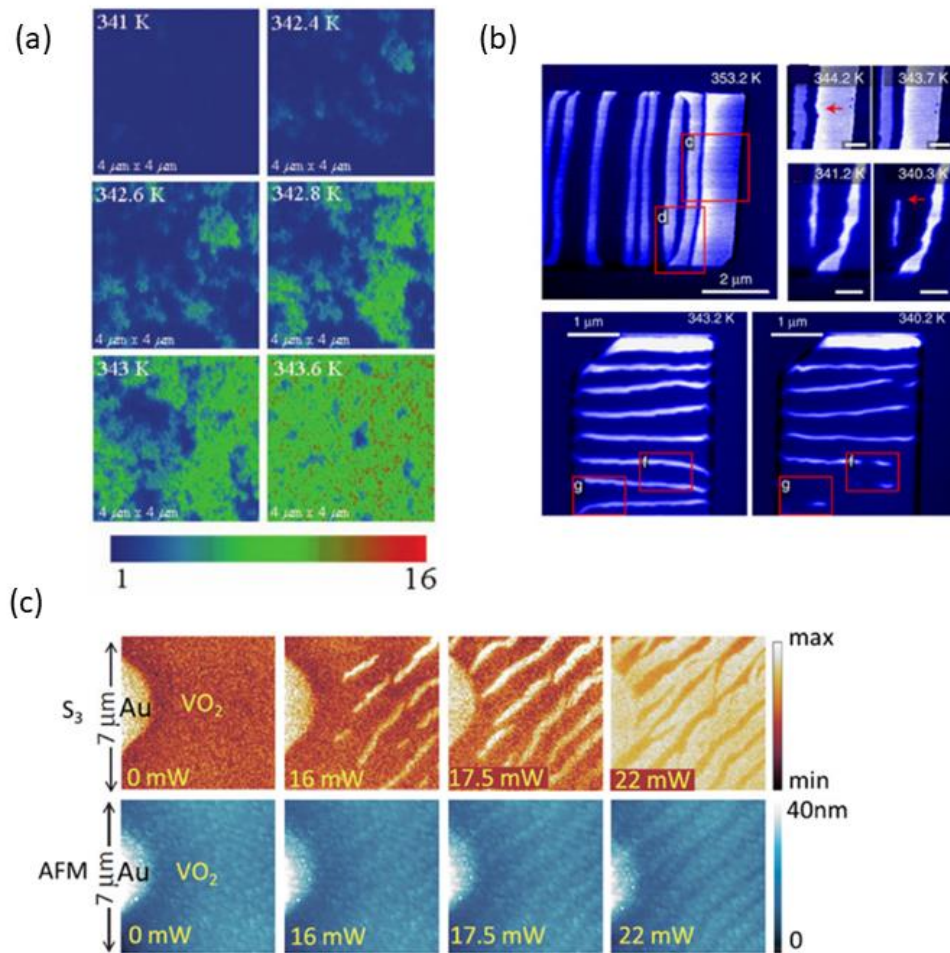


Fig. 1.2 **(a)** Temperature dependent infrared s-SNIM measurements of VO₂ on sapphire with blue indicating insulating regions and green/red indicating metallic regions. **(b)** Temperature dependent infrared s-SNIM measurements of VO₂ microcrystals with metallic (white) and insulating (blue) stripes forming perpendicular to the rutile c-axis. **(c)** Directional stripe patterns of insulating (orange) and metallic (light yellow) regions occurring in VO₂ grown on TiO₂ measured with s-SNIM in the infrared as well as the associated AFM topography below showing slight distortion due to the crystal symmetry change. The sample was heated with a near-IR pump laser. All images were obtained at a wavelength $\lambda \approx 10 \mu\text{m}$. Figure modified from Ref. [9].

1.4 Electromagnetic surface waves

Another interesting aspect of s-SNIM that will be discussed in more detail in chapter 2 is that it allows a direct probe of the near-field light-matter interactions in a sample. This means that s-SNIM can excite and probe a variety of evanescent electromagnetic surface waves called polaritons which result from a strong coupling of photons with excitations in materials such as phonons, excitons, and plasmons [10]. These surface waves manifest when the real part of the dielectric function is negative and close to zero and the imaginary part of the dielectric function is small. As will be discussed in more detail in chapters 3 and 4, s-SNIM has emerged as a method to directly image these polaritons in real space. Figure 1.3 shows a surface phonon polariton supported in the polar dielectric silicon carbide being launched from a gold edge showing how s-SNIM can directly map these surface waves [11].

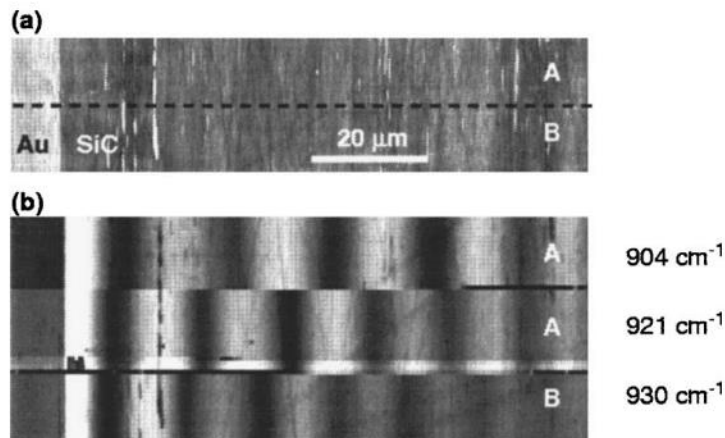


Fig. 1.3 **(a)** Atomic force microscope image of Silicon Carbide with a thin Au layer deposited on the left side. **(b)** Corresponding s-SNIM images at different wavelengths showing propagating surface phonon polaritons being launched by the Au edge. White corresponds to a high near-field signal while black corresponds to a low near-field signal. Taken from Ref. [11].

1.5 Broadband sources for s-SNIM

For all the promise that s-SNIM offers to research efforts in strongly correlated systems and polaritonic systems there is one major unresolved issue. As will be explained in Chapters 2 and 3, S-SNIM requires a combination of very high intensity light sources and very fast detectors. While conventional far-field optical and infrared spectroscopy can use basic thermal light sources such as the glowbar, s-SNIM requires much more intensity. Currently two main light sources are used for broadband s-SNIM. One is difference frequency generation (DFG), a tabletop setup that uses pulsed lasers in conjunction with a nonlinear crystal. DFG currently has a low frequency cutoff around 650 cm^{-1} due to absorptions in the nonlinear crystal [12,13]. The second is a synchrotron light source which is a large user facility that scientists must prepare proposals to apply for beam time [14]. Currently the low frequency cutoff of 330 cm^{-1} is imposed by the available detectors [15]. Most interesting strongly correlated materials, including VO_2 , have phonons far below 650 cm^{-1} . Many interesting polar dielectrics have surface phonon polaritons below that cutoff as well which could lead to interesting applications in terahertz metamaterials and coherent sources [16–18]. This dissertation encompasses a major effort to introduce an alternative plasma based light source that allows acquisition of near-field spectra down to 400 cm^{-1} , a cutoff only imposed by the detector currently available. Fig. 1.4 demonstrates how this new plasma light source compares to the two main options for broadband s-SNIM. This light source was invented to realize the potential of s-SNIM in the far- and mid-infrared for research in strongly correlated electron systems and polaritons.

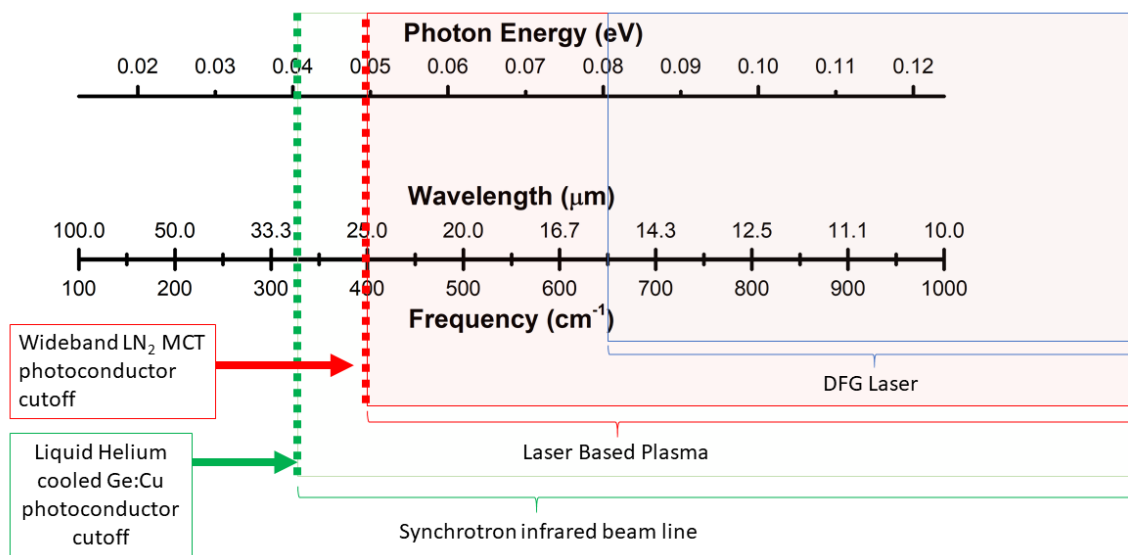


Fig. 1.4 Comparison of the low frequency cutoff of the laser based plasma developed in this dissertation with difference frequency generation and a synchrotron beam line.

1.6 Scope of the Dissertation

In chapter 2 the far-field optical and infrared spectroscopy methods are briefly reviewed before s-SNIM is introduced and covered for the case of single line imaging and broadband spectroscopy. The main contribution I have made during my time as a PhD candidate is the design and development of a high intensity broadband plasma light source for s-SNIM. This is the project I spent the majority of my time building, optimizing, repairing and improving. Chapter 3 introduces and describes this broadband plasma light source and how it is integrated into the s-SNIM experimental setup. Eventually, I made a major upgrade to this system where I utilized a high-power laser diode to sustain the plasma. This is discussed in chapter 3 as well. In chapter 4, this laser sustained light source is used in

conjunction with S-SNIM for hyper-spectral imaging of propagating surface phonon polaritons in a perovskite polar dielectric, STO. I also discuss and motivate the potential implications of this material as a far-IR nanophotonics platform. In chapter 5, an ultrathin VO₂ film is investigated in both the far- and near-field showing clear evidence of a pure Mott transition without the Peierls distortion normally seen in bulk VO₂. The bandgap of 0.6 eV is observed in the rutile insulating VO₂ film with an electronic structure not significantly changing through the insulator metal transition other than the bandgap collapsing to a weaker Drude feature than bulk VO₂. In chapter 6, I conclude and discuss future outlook of the research and experimental developments I have worked on during my PhD.

Chapter 2:

Experimental Methods

2.1 Introduction

Broadband photon spectroscopy is used to measure light-matter interactions over a broad portion of the electromagnetic spectrum to investigate the electronic and vibrational properties of a material. In photon spectroscopy, the frequency of light is expressed as inverse wavelength ($\nu/c = 1/\lambda$) in units of inverse centimeters (cm^{-1}) or as photon energy ($h\nu/e$) in units of electron-volts (eV). It is common for infrared and optical spectra to be displayed in units of inverse centimeters and/or electron-volts. Note that 1 eV is equal to 8066 cm^{-1} . Initially, this chapter will briefly review the far-field methods of Fourier transform infrared (FTIR) spectroscopy and spectroscopic ellipsometry. It will then introduce and describe scattering-type near-field infrared microscopy, or s-SNIM, the main spectroscopic technique in this dissertation.

2.2 Far-field techniques

2.2.1 Fourier Transform Infrared (FTIR) Spectroscopy

FTIR is a common technique in infrared spectroscopy which is designed around a two-arm Michelson interferometer. At the heart of this device is what is called a *beamsplitter*, which is a material where light of a certain range of wavelengths is transmitted 50% and reflected 50% when incident at a 45-degree angle of incidence. Figure 2.1 shows a basic schematic of a symmetric Michelson interferometer. Collimated broadband light is incident on this beamsplitter which sends 50% of the beam to a fixed mirror and 50% of the beam to a moving reference mirror. These mirrors reflect the beams which are recombined at the beamsplitter and together are either reflected off a sample or transmitted through a sample and incident on a detector which measures the intensity of the photons. By scanning the reference mirror through a small distance, d , an optical path difference is introduced to the light recombined at the beamsplitter. This optical path difference causes interference fringes at the detector which can be measured as intensity as a function of mirror position. By taking the Fourier transform of this signal, the intensity can be resolved as a function of photon frequency.

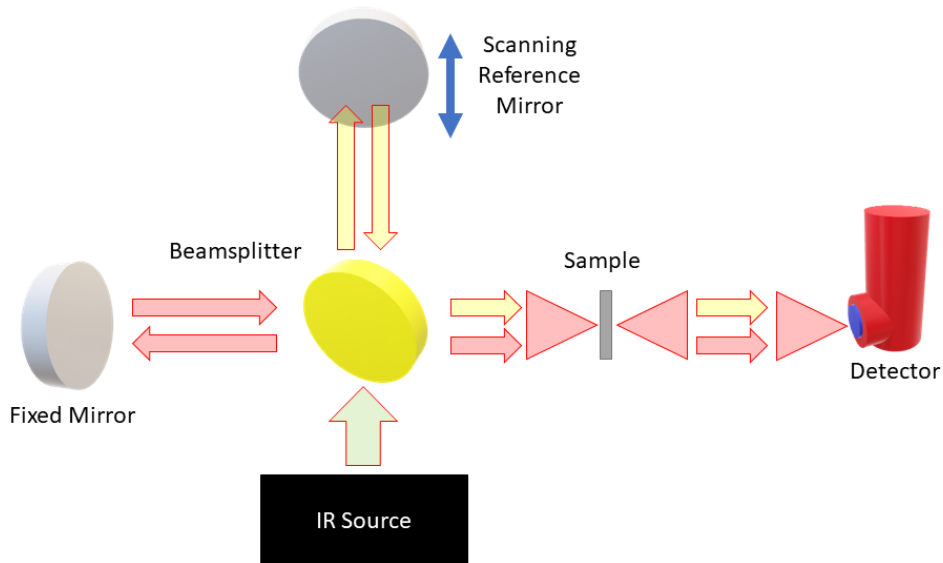


Figure 2.1 Schematic of a symmetric Michelson interferometer operating in transmission mode.

In FTIR, a normalization spectrum is needed. This is because the measured intensity at the detector is not just a function of the sample, but also a function of the optical response of the various optics, windows, beamsplitter and the detector spectral response. In transmission mode, the sample spectrum is normalized to a spectrum without a sample present to obtain absolute transmission, $T(\nu)$. In reflection mode, a spectrally featureless metal such as gold or aluminum is measured and this normalization spectrum is used to obtain the absolute reflectance of the sample, $R(\nu)$.

2.2.2 Spectroscopic Ellipsometry

Ellipsometry is a highly sensitive spectroscopic technique used to characterize thin films and surfaces as well as bulk samples. Ellipsometry measures the change in

the polarization state of light reflected off a sample. A basic schematic can be seen in Fig. 2.2. Linearly polarized light, set by a polarizer at a known polarization angle, is incident on the sample at a known angle of incidence. The unknown polarization state of the light reflected off the sample is measured by a polarizer that rotates at a known rate and is called the rotating analyzer [Fig. 2.3]. A detector after the rotating analyzer detects a time varying signal from which, combined with the known polarization angle of the incident light, two observables are measured, called Ψ and Δ . These are related to the complex Fresnel reflection coefficients by $\frac{\widetilde{R}_p}{\widetilde{R}_s} = \tan(\Psi)e^{i\Delta}$. It is from the Fresnel reflection coefficients that the complex optical constants can be solved for [19].

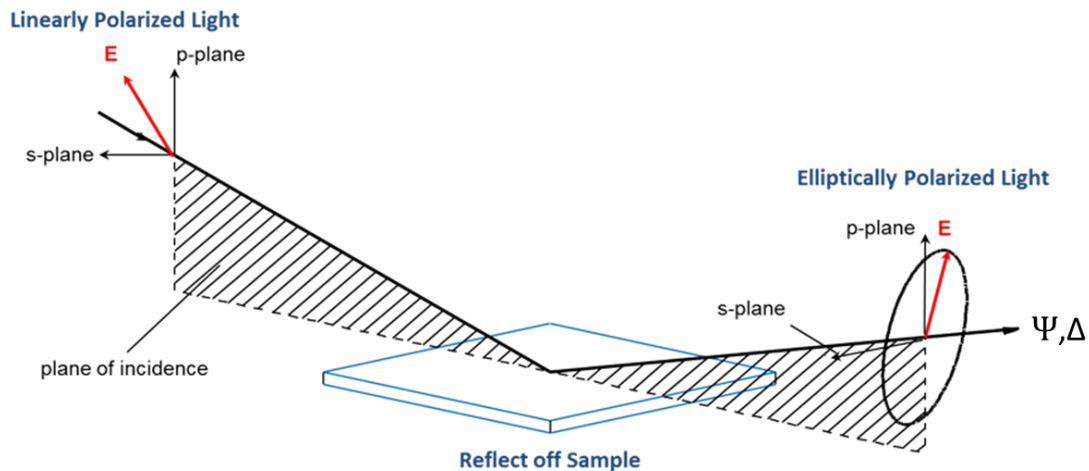


Figure 2.2 A basic schematic of Ellipsometry showing the sample, incident light and reflected light and their polarization states [20].

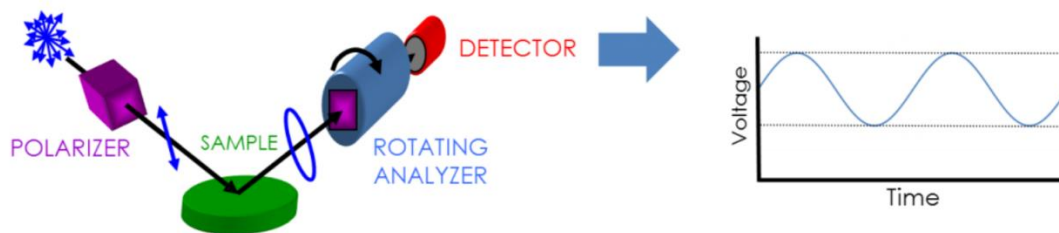


Figure 2.3 A image of how the incident light is polarized, reflected, and how the resulting polarization state is measured by the rotating analyzer. This signal is measured by a detector as a time varying voltage.

2.3 Near-field Techniques

2.3.1 The Abbe-diffraction Limit

Until now, the experiments reviewed have been far-field experimental techniques, wherein the dimensions of the scatterer are much larger than the wavelength of the incident radiation. These methods work well for uniform thin films and larger crystals. However, in the case for nanostructured samples, materials exhibiting sub-micron phase coexistence or materials that can only be grown as very small crystals there is a need to focus the light to a small spot. Infrared Microscopy is a technique in which the light from an FTIR is brought through a special microscope and focused to a small spot but even this technique is limited by the wave nature of light.

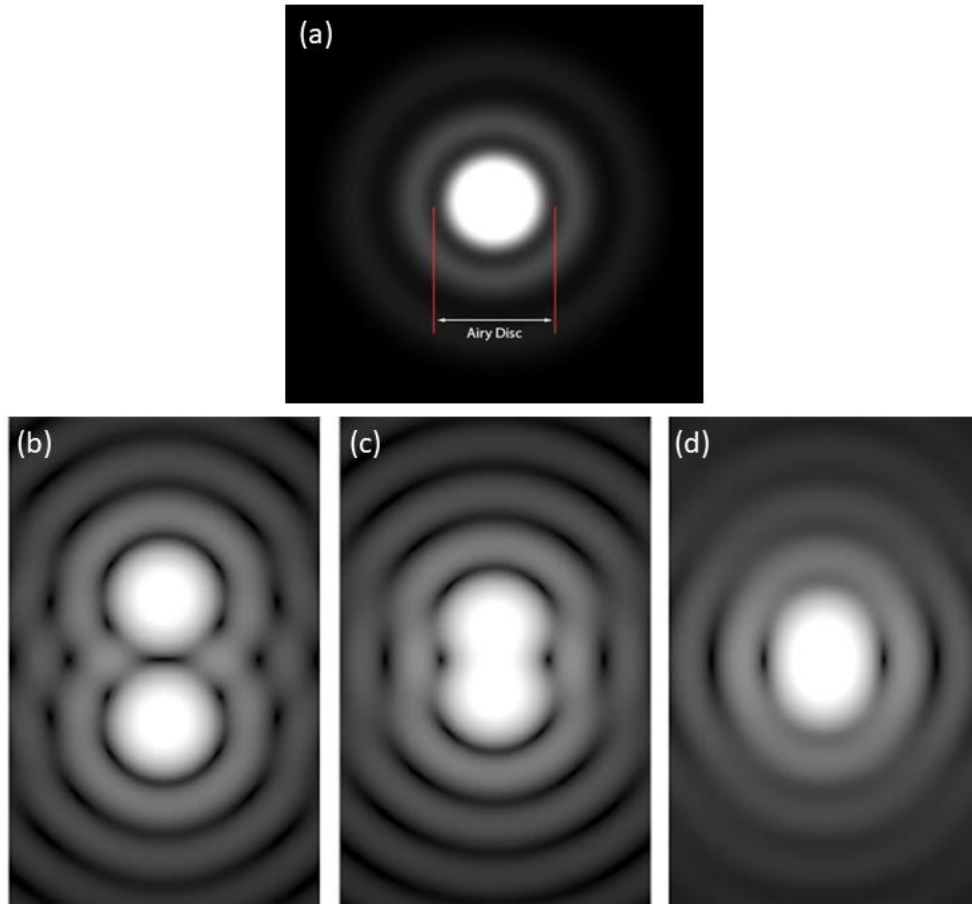


Figure 2.4 **(a)** From Ref. [21]. An Airy disk diffraction pattern due to the diffraction of a point source of light. **(b-d)** From Ref. [22]. The Rayleigh Criterion of **(b)** two resolved points, **(c)** the central peaks beginning to overlap and **(d)** the central fringes almost completely overlapping.

Due to the wave nature of light, radiation from even an infinitely small point source cannot be focused infinitely. The image of a point source of light exhibits a diffraction pattern known as the Airy disk pattern (see Fig. 2.4) in which a central peak in intensity is surrounded by concentric ring fringes [23,24]. This leads to a limit in the spatial resolution that far-field optics can achieve in which the minimum

lateral resolution is defined as the distance between two point sources where the central fringes begin to overlap. The Rayleigh diffraction criterion for an optical microscope defines the minimum distance resolvable between two point sources, Δd , defined in Eq. (2.1).

$$\Delta d = \frac{0.61\lambda}{NA} \quad (2.1)$$

In Eq. (2.1), λ is the wavelength of light and NA is the numerical aperture, defined as $NA = n \sin(2\theta_{max})$. Here, n is the refractive index of the medium the light is traveling through and $2\theta_{max}$ is the maximum collection angle of the focusing optic. For example, a practical maximum NA for a microscope is around 0.95 and the index of refraction through air is 1. At this numerical aperture the diffraction limit can be approximated to $\Delta d = \lambda/2$. For visible light at violet wavelengths ($\lambda = 400$ nm) we get a $\Delta d \approx 200$ nm. However, for longer wavelength infrared light of say $\lambda = 20 \mu\text{m}$ we only get a resolution of $10 \mu\text{m}$. This is clearly not compatible with the nanoscale systems that are becoming more and more prominent and one needs to turn to nano-optics.

2.3.2 Scattering-Type Scanning Near-field Infrared Microscopy

Scattering-type scanning near-field infrared microscopy is a technique in which light is focused to a metal coated atomic force microscope tip operated in tapping mode. The apex of this tip has a radius of curvature on the order of tens of nanometers which is sufficiently in the near-field regime when illuminated with

infrared radiation. Due to the sharp apex of the tip and metal coating, the tip acts as an antenna that concentrates the incoming electric field to the nanoscale tip apex. Resulting from the 'lighting rod' effect from electrostatics, charge is accumulated at the apex causing local high electric fields [25,26]. When the illuminated tip is brought into close contact with a sample, the local evanescent near-field interaction between the sample and tip influences the light scattered by the tip. Figure 2.3 shows a simplistic depiction of the tip over the sample with the near-field interaction more closely depicted in Fig. 2.3(b). A simple description of the near-field interaction can be illustrated with the 'simple-dipole' model [7,8,27] where the tip is approximated as a sphere with radius corresponding to the radius of the apex of the tip. The incident field, E_{inc} , focused on the tip polarizes this sphere, which induces an image dipole to be formed in the sample that has a dielectric function, ϵ . This image dipole repolarizes the tip with a polarizability, $p_z(\epsilon)$, that is encoded in the scattered field, E_{scat} . This way the information of the nanoscale dielectric function of the sample area just under the tip apex is encoded and scattered into the far-field. This backscattered light is collected and sent to a detector to yield the nano-resolved near-field signal of the area under the tip. This way, an AFM image can be taken to obtain topography while also simultaneously obtaining the nano-resolved near-field image of the same area.

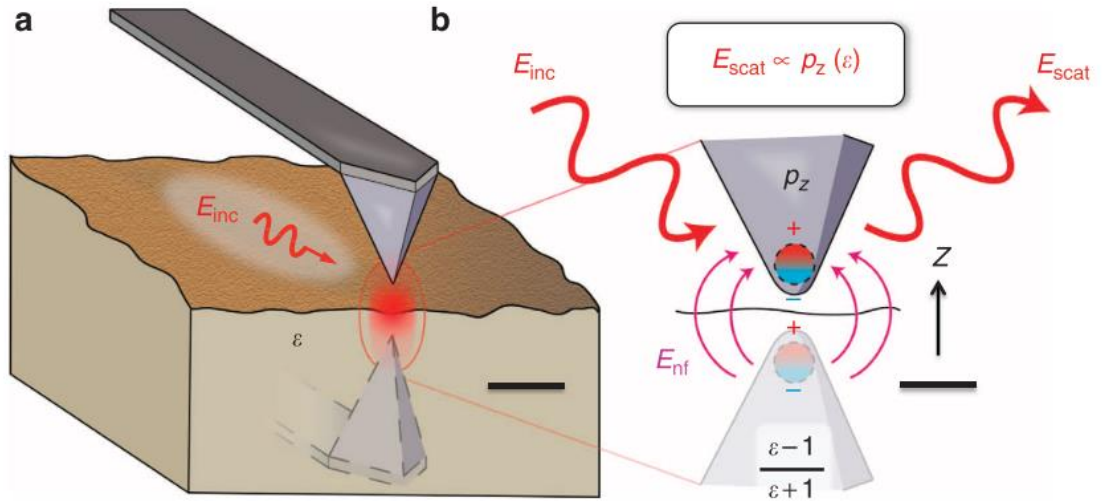


Figure 2.3 From Ref. [28]. **(a)** A Schematic of the AFM cantilever tip and sample showing the incoming radiation focusing at the tip apex. **(b)** A closeup of the tip apex showing the induced dipole at the tip with the image dipole induced in the sample.

This near-field interaction can be expressed by the complex scattering coefficient $\sigma = se^{i\varphi}$, where s is the amplitude and φ is the phase. The incident field and elastically scattered field are related by this coefficient as

$$E_{\text{scat}} = \sigma E_{\text{inc}} \quad (2.2)$$

Usually, this tip is illuminated by infrared light with a wavelength on the order of microns, which due to the diffraction limit means that the full tip tetrahedron and some of the cantilever is illuminated. This results in a dominant and unwanted noise in the signal called the ‘background’. Only a portion of the total backscattered field, E_{scat} , contains the near-field information which we will call, E_{nf} , while the rest of the scattered field is due to the background, E_{bg} . In most experimental setups, the electric field strength cannot be detected directly. Photon detectors usually

measure the currents or voltages proportional to the number of photons absorbed which we call Intensity, I , where $I \propto |E|^2$. Since the detector only measures the intensity, I_{scat} , of the scattered field we can express the signal measured by the detector as

$$\begin{aligned} I_{\text{det}} \propto I_{\text{scat}} \propto |E_{\text{scat}}|^2 &= |E_{\text{nf}} + E_{\text{bg}}|^2 \\ &= |E_{\text{nf}}|^2 + |E_{\text{bg}}|^2 + E_{\text{nf}}E_{\text{bg}}^* + E_{\text{bg}}E_{\text{nf}}^* \end{aligned} \quad (2.2)$$

In S-SNIM the AFM is operating in tapping mode where the tip is tapping at a frequency, $\tilde{\nu}$, on the order of kHz with a vertical tapping amplitude usually around 70 nm. This tapping modulates both the near-field and background scattering contributions allowing us to write E_{scat} as

$$E_{\text{scat}}(t) = E_{\text{nf}}(t) + E_{\text{bg}}(t) = \sum_{n=0}^{\infty} E_{\text{nf},n} e^{in\tilde{\nu}t} + \sum_{n=0}^{\infty} E_{\text{bg},n} e^{in\tilde{\nu}t} \quad (2.3)$$

Where $E_{\text{nf},n}$ and $E_{\text{bg},n}$ are the n^{th} order Fourier coefficients of the scattered near-field and background contributions to E_{scat} respectively. These can be expressed as $E_{\text{nf},n} = \sigma_{\text{nf},n} E_{\text{inc}}$ and $E_{\text{bg},n} = \sigma_{\text{bg},n} E_{\text{inc}}$. Since E_{nf} is due to the strong evanescent near-field interaction of the tip sample system, the act of the tip tapping introduces a large non-linear tip sample distance dependence on this scattered signal [8]. At the same time, the background scattered signal, E_{bg} , largely dependent on scattering from parts of the tip that do not exhibit strong evanescent fields, has a more linear tip-sample distance dependence. While the background scattered signal is still present to an extent at the tapping frequency, $\tilde{\nu}$, the non-linear near-field scattered signal dominates at the higher harmonics of the tapping frequency,

$n = 2, 3, 4, \dots$, allowing significant suppression of the background by demodulating the measured signal at the higher harmonics via lock-in detection. Looking at Eq. (2.2), we see that there are still multiplicative terms between the near-field and background that will persist at the higher harmonics. We call this the ‘multiplicative background’. So the act of demodulating the signal at the higher harmonics does not completely yield a background free signal.

There are multiple interferometric solutions to obtaining the completely background-free near-field signal and they are dependent on the type of data one needs to acquire. The two main ways an s-SNIM microscope is operated is in nano-imaging mode and nano-spectroscopy mode. In nano-imaging mode, single-line (monochromatic) illumination is incident on the tip while the tip raster scans over an area of the sample to create a near-field image at a single wavelength where each pixel of the image indicates the nanoscale near-field resolved signal. This enables single line near-field mapping. In nano-spectroscopy mode, the tip is brought into contact at a select area of the sample and a point spectrum is acquired by sending in broadband illumination to yield the frequency dependent near-field response, $\sigma(\nu) = s(\nu)e^{i\varphi(\nu)}$.

2.3.3 Pseudo-heterodyne s-SNIM

This section will briefly describe pseudo-heterodyne interferometric detection which is a method to obtain background-free s-SNIM images with monochromatic illumination that was first implemented by Ocelic et al. in 2006 [Ref. [29]]. By

placing the tip sample system in one arm of an asymmetric Michelson interferometer [see Fig. 2.4a] a reference arm field, E_{ref} , is introduced to the measured signal at the detector. This gives us a measured intensity at the detector of

$$\begin{aligned}
 I_{\text{det}} &\propto |E_{\text{scat}} + E_{\text{ref}}|^2 = (E_{\text{nf}} + E_{\text{bg}} + E_{\text{ref}})(E_{\text{nf}} + E_{\text{bg}} + E_{\text{ref}})^* & (2.4) \\
 &= |E_{\text{nf}}|^2 + |E_{\text{bg}}|^2 + |E_{\text{ref}}|^2 + E_{\text{nf}}E_{\text{bg}}^* + E_{\text{nf}}E_{\text{ref}}^* \\
 &\quad + E_{\text{bg}}E_{\text{nf}}^* + E_{\text{bg}}E_{\text{ref}}^* + E_{\text{ref}}E_{\text{nf}}^* + E_{\text{ref}}E_{\text{bg}}^*
 \end{aligned}$$

where the scattered field is modulated by the tip oscillation frequency, $\tilde{\nu}$, usually ~250 kHz. The position of the reference mirror is then modulated in the direction of beam propagation at a frequency M , such that $M \ll \tilde{\nu}$. Sum and difference frequencies appear as sidebands around the tip oscillation harmonics as $n\tilde{\nu} \pm mM$ due to the interference of the reference field and scattered field. The detected signal with the sidebands can be seen in Fig. 2.4b.

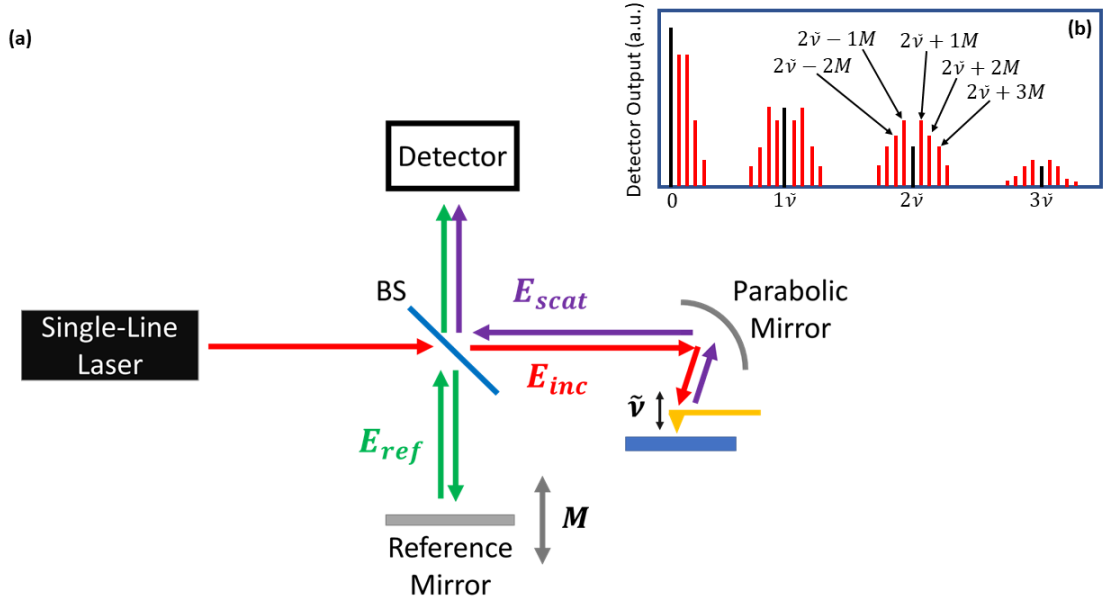


Figure 2.4 **(a)** Schematic of the pseudo-heterodyne interferometric detection scheme used in S-SNIM. **(b)** Modified from Ref. [29]. Detector spectrum from the splitting of the signal into sidebands due to modulation from the reference signal.

As can be seen in Eq. (2.4), the multiplicative background is now removed because it does not depend on the modulated reference signal. The other terms containing the background are removed by the higher harmonic demodulation and we are only left with the terms containing contributions from the near-field and reference signals. It is also notable to mention that there are methods to extract the amplitude, $s_{nf,n}$, and phase, $\varphi_{nf,n}$, by subsequent normalization between the sidebands which is covered in more detail in Ref. [29]. Through modeling these two observables can be used to solve for the complex optical constants at nanoscale resolution [7].

2.3.4 Scattering-Type Scanning Near-Field Infrared Spectroscopy

For infrared nano-spectroscopy, broadband illumination is incident on the tip-sample system in one arm of a Michelson interferometer. This makes this interferometer an asymmetric FTIR which allows the acquisition of both amplitude and phase resolved spectra [30]. This is advantageous since this gives two observables to solve for the two unknowns that are the real and imaginary parts of the optical constants (or dielectric function). Figure 2.5a shows a schematic of the broadband interferometer. It is essentially the same as the pseudo-heterodyne setup but with the reference mirror scanning over a much larger distance.

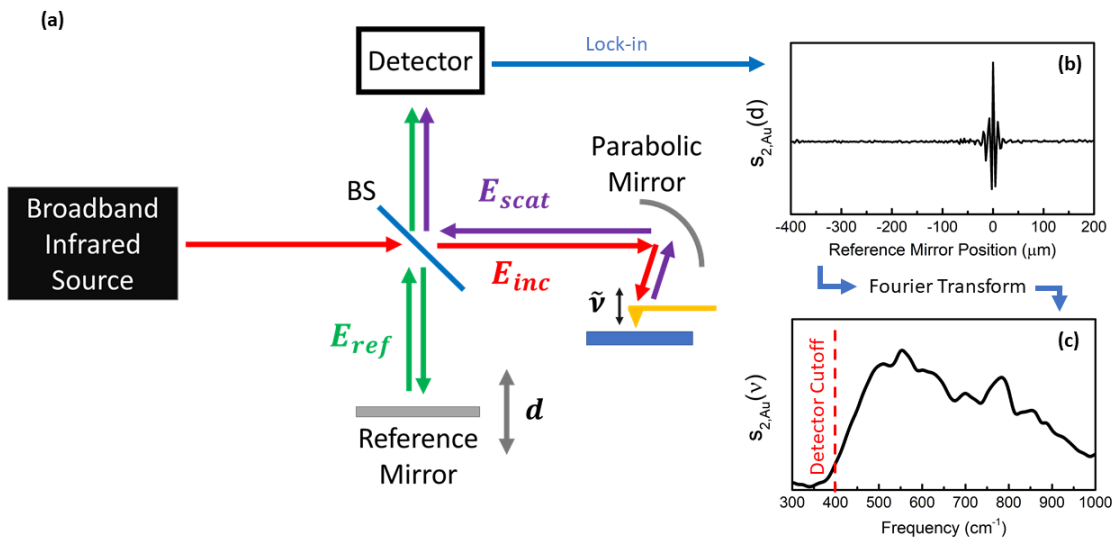


Figure 2.5 (a) Schematic of the broadband nano-spectroscopy interferometric setup. (b) An interferogram obtained with the tip over gold as well as the subsequent spectrum (c) obtained after performing the Fourier transform.

Keeping in mind that $\sigma_n = s_n e^{i\varphi_n}$, noting that the background is negligible at values of $n > 1$, and taking $n \geq 2$ we can follow simplification outlined in Ref.'s [31–33] to express Eq. (2.4) as

$$I_n \propto s_{\text{nf},n} \{s_{\text{bg},0} \cos(\varphi_{\text{nf},n} - \varphi_{\text{bg},0}) + s_{\text{ref}} \cos(\varphi_{\text{nf},n} - \varphi_{\text{ref}})\} \quad (2.5)$$

By scanning the reference mirror a distance d , through the position of equal optical path lengths called the ‘white light position’ in small mirror position increments dd , we can obtain an interferogram [Fig. 2.5(b)]. Since φ_{ref} can be expressed as $2\pi\nu d$ we can do a Fourier transform on this interferogram to get the spectrum $S_n(\nu)$ [Fig. 2.5(c)].

$$S_n(\nu) = \int_0^{\infty} s_{\text{nf},n} \{s_{\text{bg},0} \cos(\varphi_{\text{nf},n} - \varphi_{\text{bg},0}) + s_{\text{ref}} \cos(\varphi_{\text{nf},n} - 2\pi\nu d)\} e^{i2\pi\nu d} dd \quad (2.6)$$

Looking at Eq. (2.6) we can see that only the second term has a d dependence and thus the term with the background contribution is removed yielding a pure near-field spectrum. With proper modeling, the broadband amplitude and phase resolved spectrum $S_n(\nu) \propto s_{\text{nf},n}(\nu) e^{i\varphi_{\text{nf},n}(\nu)}$ can be used to solve for the broadband nanoscale optical constants the same way as the single-line, pseudoheterodyne method [7].

Using the broadband s-SNIM experimental setup developed in this dissertation with the laser sustained plasma light source (chapter 3), an interferogram [Fig. 2.5(b)] taken with the tip over a gold surface yields a spectrum [Fig. 2.5(c)]. This spectrum does not just contain features from the near-field

spectrum on gold. This spectrum is a convolution of the optics, mirror protective coatings, detector response curve and various other dispersive elements in the beam path that effect the broadband spectrum as the light travels through the interferometer. For this reason the near-field spectra from a sample need to be normalized to a spectrally featureless reference material such as silicon or gold. This way the instrumental dispersive features, which are present regardless of the sample studied, are removed. It should also be noted that the interferogram in Fig. 2.5(b) represents the real part of the complex valued signal coming from the lock-in amplifier doing the demodulation. When taking data, the complex valued interferogram is processed to obtain both the amplitude and phase.

Chapter 3:

Broadband near-field infrared spectroscopy with high temperature plasma light sources

3.1 Introduction

Circumventing the diffraction limit of light using scattering-type scanning near-field infrared microscopy (s-SNIM) has proven to be a powerful technique for probing the local nanoscale optical properties of solids. Its recent applications as a nano-imaging tool have employed mid-infrared frequencies while circumventing the diffraction limit by nearly three orders of magnitude [14,34]. By using broadband illumination with asymmetric Fourier transform infrared (FTIR) spectroscopy, local near-field spectra with nanometer scale spatial resolution have been obtained [7,8,35]. S-SNIM is based on an atomic force microscope (AFM) operated in tapping mode in which light is focused on to the metallic AFM tip in close proximity to the sample. The tip- sample interaction is encoded in the scattered optical signal which is then measured in the far-field with a photodetector. The ratio of the backscattered power compared to the incident power at the tip is $\eta_B \approx 0.02$, and the useful near-field signal is an even smaller

fraction f_N of η_B , estimated to be $f_N \approx 0.003$ for a standard tip over gold [36]. Since the ratio of the scattered near-field signal to incoming light at the tip is so small, it is necessary to use high intensity light sources.

Broadband nano-spectroscopy in the far- and mid-infrared spectral range is challenging because of the limitations of existing high intensity light sources. The use of tunable, monochromatic lasers allows for high signal but is limited by the available wavelengths and obtaining a high-resolution broadband spectrum requires significant time [37]. Quantum cascade lasers (QCLs) have been implemented with S-SNIM and have the ability to quickly scan through wavelengths but have a narrow spectral range [38,39]. Difference frequency generation provides a stable high intensity beam in the mid-infrared but needs to be tuned to different wavelength ranges to get the full spectrum and currently has a low frequency cutoff of $\sim 550 \text{ cm}^{-1}$ (18 μm wavelength) [12,13]. Thermal blackbody light sources like the globar provide a large spectral bandwidth but low intensities. Hence, significant integration time is required to obtain data with a globar and there is no usable intensity below $\sim 750 \text{ cm}^{-1}$ for broadband S-SNIM [40,41]. Previously, a globar was implemented as a broadband infrared source in our own near-field experimental setup. We were able to resolve phonon resonances in SiO_2 and SiC in the mid-infrared but the signal-to-noise level was very low and integration times of a few hours were required. Synchrotron light sources provide spatially coherent intense broadband light that is currently the highest intensity and widest bandwidth infrared source for nano-spectroscopy [14,42,43]. However, experiments require beam time at the

synchrotron that is highly competitive to obtain and is generally of limited duration. Moreover, travel and accommodation costs are generally borne by the users. These issues make it challenging to do in-depth, long-term studies on samples at synchrotron beamlines, and also make it difficult to implement modifications and improvements to equipment that are better suited for table top set-ups.

A wall stabilized plasma light source has shown potential as a high intensity broadband light source in both the far-field and the near-field. However, there is only one published work using this light source for near-field infrared spectroscopy. Moreover, the startup procedure for this light source requires a manual shorting of the arc, there are reports of “violent sputtering episodes” at the anode, and the required input power to sustain the arc is on the order of kilowatts [44–46]. The most common type of commercial plasma light sources are the xenon high pressure plasma lamps which are useful as a broadband source for the near-infrared, visible and ultraviolet i.e. frequencies higher than $2,500\text{ cm}^{-1}$. However, these lamps do not provide intensity in the mid- and far-infrared due to the plasma being encased in a quartz bulb which is opaque to these wavelengths. There is a need for a practical and affordable table-top light source that is ultra-broadband and covers the spectral range of $\sim 100\text{ cm}^{-1} - 2,500\text{ cm}^{-1}$ to allow the exploration of materials at the nanoscale by probing infrared-active phonon resonances and electronic properties.

Infrared spectroscopy has been commonly used to probe infrared-active phonons and charge dynamics in materials. However, many materials have been shown to exhibit phase coexistence at length scales much smaller than the

diffraction limit of infrared light. Infrared nano-spectroscopy techniques are necessary to properly understand the charge and lattice dynamics of these nano-domains that exist in a number of materials, for example, the oxides of vanadium and manganese as well as in the ternary alloy $\text{In}_{1-x}\text{Ga}_x\text{N}$. [6,47–50]. Recently, an S-SNIM setup has demonstrated that there is nanoscale phase coexistence of two crystallographic phases known as the thin film phase and bulk phase of pentacene [51]. It is shown through nano-imaging and point spectroscopy in the mid-infrared that there is bulk phase nucleation of pentacene during the growth of the expected thin film phase as well as during sample storage. In the mid-infrared it has been shown that the local absorption spectrum of silicon nitride nanoislands can be observed using S-SNIM [52]. To have the ability to probe nanoscale domains with broadband infrared spectroscopy in the far-infrared and mid-infrared spectral range would allow these types of experiments to be performed on a number of materials to discover and explore nanoscale phenomena that may also have significant potential for applications. Researchers will be able to probe the crystallinity of thin films over a broad spectral range, allowing the testing of the effectiveness of different growth methods. Moreover, the technique can be employed for nanoscale identification of materials, and quality control and characterization of nano-devices.

In this work, we introduce a new table-top light source that has significant potential as a broadband high intensity source of mid-infrared and far-infrared frequencies for microscopy applications. Our electrode stabilized argon plasma light source (APLS) is described, and its emission spectrum is characterized using

an FTIR spectrometer and compared to the well-known globar source. Then we employ the APLS for broadband nano-spectroscopy in the mid-infrared spectral range by resolving the phonon-polariton resonance in SiO₂ using a calibration grating of 100 nm of SiO₂ on Si (µmasch TGXYZ02). We demonstrate this argon plasma lamp's potential as a far-infrared light source by resolving a phonon-polariton resonance in bulk, crystalline strontium titanate (SrTiO₃). The spectra measured at room temperature are compared to the point dipole model and the finite dipole model using known literature values for the dielectric functions of SiO₂ and SrTiO₃ [53–55]. The broadband infrared nano-spectroscopy setup is then modified to extend the lower frequency cutoff to 400 cm⁻¹ (25 µm) and a spectrum on STO is taken again resolving a new sharper SPhP at 425 cm⁻¹. This spectrum is modeled both with analytical and numerical simulations. Finally, A significant improvement to the APLS is described wherein the Argon noble gas is replaced with Xenon and a high power near-IR laser is used to drive the plasma instead of an electrical current. The improvement is demonstrated by spectra on SiO₂ and STO showing significantly improved signal to noise.

3.2 Experiment

3.2.1 Argon Plasma Light Source (APLS)

A noble gas plasma radiates bremsstrahlung (or free-free radiation) that is primarily from deceleration of free electrons due to interactions with ions, atoms and other electrons [56]. From the near-infrared to the ultra-violet, there is a

continuum of bremsstrahlung radiation as well as intense, discrete atomic emission lines whose frequencies depend on the noble gas. In the far-infrared and much of the mid-infrared there is also significant continuum bremsstrahlung radiation but fewer atomic emission lines. Our home-built, electrode stabilized APLS has been constructed similar to a conventional short-arc lamp. One important difference from the conventional short-arc lamp is that the APLS is housed inside a sealed aluminum vessel with an infrared transparent window to allow access to the mid-infrared and far-infrared frequencies. A schematic representation of the APLS can be seen in Fig. 3.1. A high voltage pulse is applied to two tungsten electrodes 2 mm apart in high purity argon gas at a gauge pressure of one atmosphere. This causes an arc discharge to occur between the electrodes which is then sustained by a current of about 7 amperes. The input power to this lamp is about 90 W. The electrodes are in thermal contact with the water-cooled aluminum vessel but electrically isolated from it. A potassium bromide (KBr) or zinc selenide (ZnSe) window is clamped to the vessel to allow for infrared optical access to the plasma emission. Viton o-ring seals are used for isolating the high purity argon gas inside the vessel from atmospheric contamination. The light emission from the plasma is steered into a port of our Bruker Vertex 80v FTIR spectrometer using two off-axis parabolic mirrors. The first parabolic mirror collimates the beam which is then filtered through a germanium disk to eliminate the unwanted near-infrared and visible portion of the spectrum. The spectrum is measured using a KBr beam splitter and a liquid nitrogen cooled Mercury-Cadmium-Telluride (MCT)

photoconductor (Infrared Associates) with a KRS-5 window, and a 1 mm x 1 mm element.

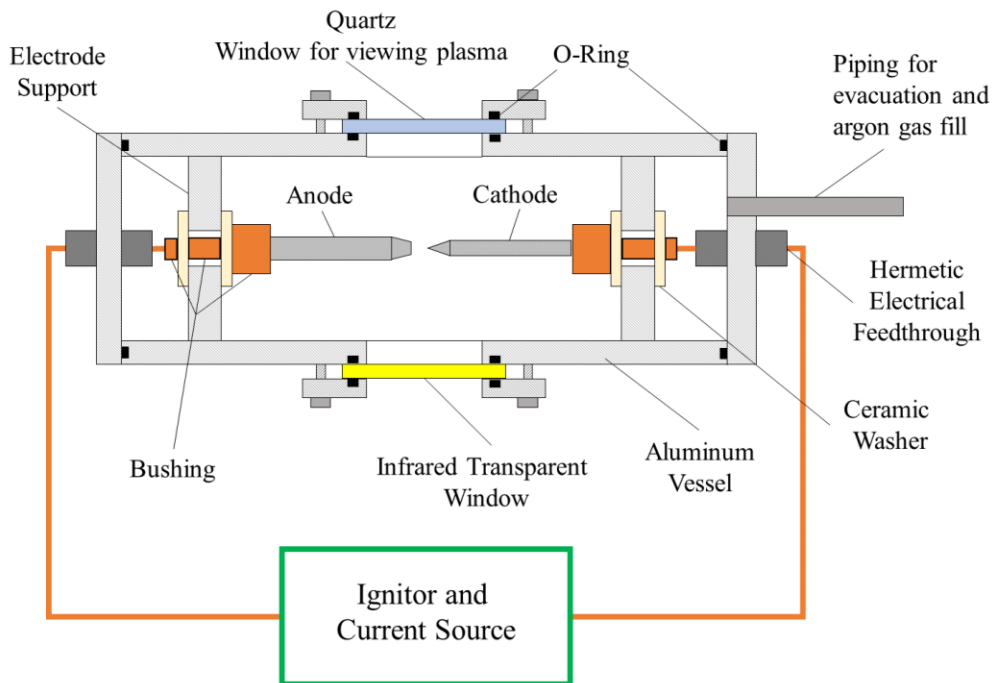


Fig. 3.1 A schematic representation of the APLS. A top view cross-section of the APLS is shown.

In Fig. 3.2(a), we plot the measured spectrum of the APLS. In the same figure, we also plot the spectrum of the globar source which radiates as a 1320 K blackbody. The globar spectrum was measured without the germanium filter. The absolute transmission of the germanium filter was also measured in the FTIR spectrometer. The lower cutoff of the APLS spectrum at $\sim 500 \text{ cm}^{-1}$ is due to the KBr beam splitter, the MCT detector, and ZnSe window of the APLS, and the upper cutoff at $\sim 5,800 \text{ cm}^{-1}$ is due to the germanium disk. The APLS spectrum displayed

in Fig. 3.2(a) has been corrected for the reduced transmission through the ZnSe window and the germanium disk to demonstrate the radiance of the plasma relative to that of the globar. This was done so that the radiance of the plasma can be seen independent of the choice of window and filter. The radiance of the APLS plasma in the region below 1000 cm^{-1} ranges from about 7 to 10 times that of the globar. Based on this relative radiance, we say that our effective plasma temperature is about 9000 K or higher. By taking the ratio of two successive measurements of the spectrum, 100% lines were obtained (Fig. 3.2(b)) to demonstrate the stability of the APLS compared to that of the globar. The APLS demonstrates highly stable intensity suitable for spectroscopy and microscopy rivaling the stability of the globar. The APLS is a highly stable light source because of the effective suppression of convection currents. The data from the APLS shown in Fig. 3.2 establishes this source's potential as an intense and stable mid-infrared and far-infrared light source. It is expected that there is significant intensity in the far-infrared below our lower measurement cutoff frequency [56]. Finally, due to the "short arc" electrode stabilized geometry of our lamp, the "hot spot" of the plasma, a volume that has the highest infrared emission, is estimated to be about 300 to 500 μm in diameter. This means that the APLS is closer to a point source than a globar making it more suitable for microscopy applications [57].

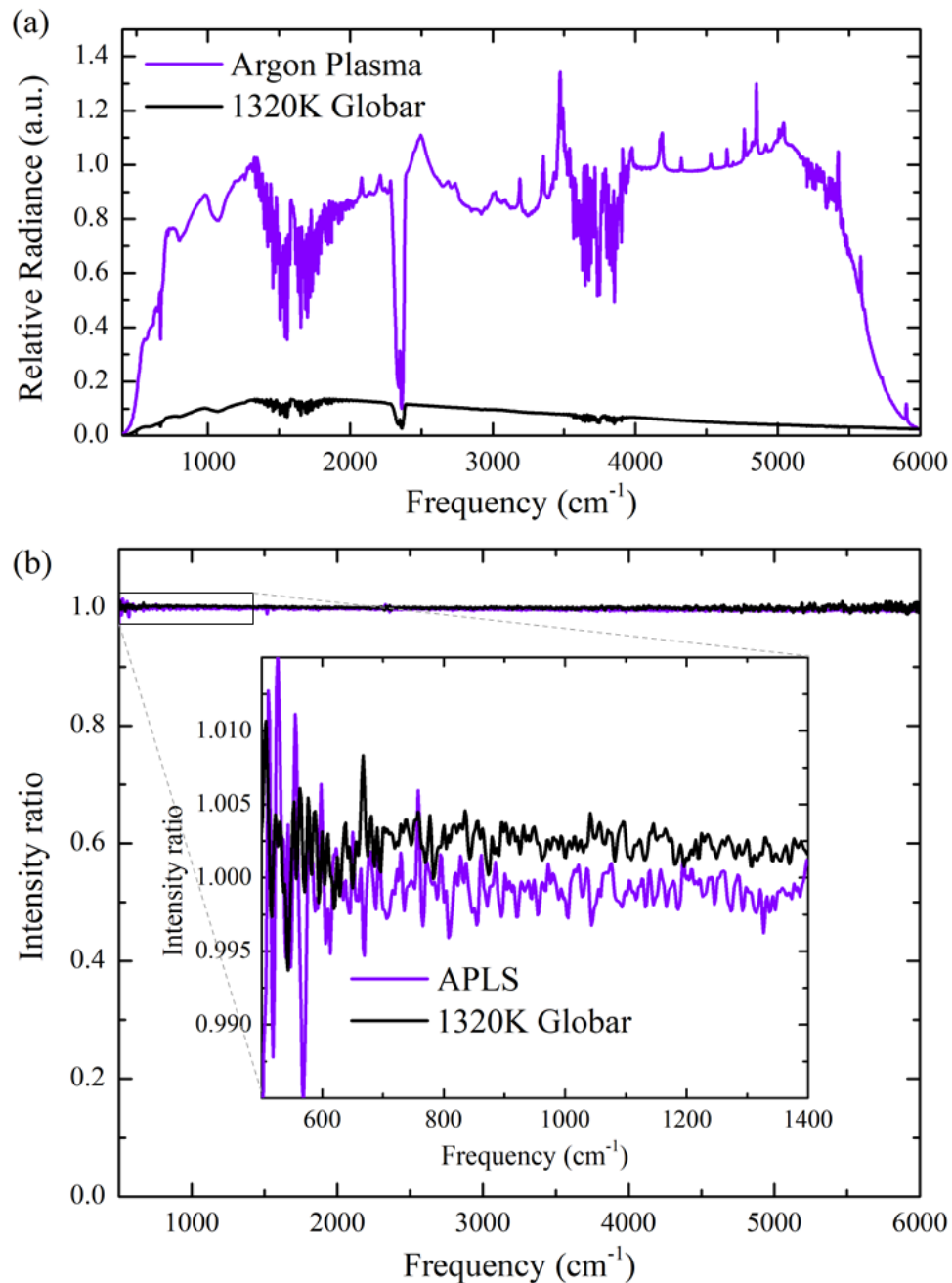


Fig. 3.2 **(a)** Relative radiance of the argon plasma (violet) compared to a 1320 K globar (black). The spectra were obtained with the Bruker Vertex 80v FTIR spectrometer in air. Sharp peaks in the APLS spectrum are mainly due to argon emission lines and the valleys are mainly due to atmospheric absorption. The atmospheric absorption features also appear in the globar spectrum. **(b)** Comparison of 100% lines taken with the Globar and APLS. (Inset) Zoomed in view of 100% lines demonstrating the relative noise levels of both sources in our spectral range of interest.

3.2.2 Broadband near-field infrared spectroscopy

The nano-spectroscopy setup primarily consists of a commercial S-SNIM from Neaspec GmbH and our APLS. Fig. 3.3(a) shows a schematic representation of our beam path. The light from the hot spot of our argon plasma is collected and collimated with an off axis parabolic mirror with a 2 inch focal length. It is then incident on an indium tin oxide (ITO) coated glass planar mirror with a 45 degree angle of incidence. The ITO mirror significantly reduces the unwanted near-infrared and visible portion of the spectrum in the reflected light. Thereafter, the beam is focused through a 300 μm pinhole by a second 4 inch focal length off-axis parabolic mirror. There are multiple advantages of using a pinhole in our system. In S-SNIM, a high numerical aperture mirror both focuses the incident radiation as well as collects the scattered radiation from the tip. Since the tip has a radius on the order of 10s of nanometers, its usable near-field scattered radiation after being collimated by the parabolic mirror is highly spatial coherent due to the small source area. The broadband radiation collected from the plasma is less spatially coherent due to its dimensions being much larger than the tip apex. By focusing the broadband radiation on a pinhole, we improve the overlap of the tip scattered and reference arm radiation that gets focused on the detector element thus maximizing the interference at the detector. After the pinhole, the light beam is collimated using a one inch focal length off axis parabolic mirror, setting the beam diameter to $\sim 10\text{mm}$, and sent into our broadband s-SNIM system.

The s-SNIM set-up consists of an atomic force microscope employing a metallic coated AFM tip and an asymmetric FTIR interferometer. The incoming

collimated infrared beam is incident on a ZnSe beam splitter sending part of the beam to the movable reference mirror and the other part of the beam to a parabolic mirror which is used to bring the beam to a focus on the tip and to collect and collimate the backscattered light. The backscattered and the reference beams are recombined at the beam splitter and brought to a focus on a liquid nitrogen cooled MCT detector. For the SiO₂ sample we use an AFM tip with a radius of about 15 nm (Arrow-NCPt) and a liquid nitrogen cooled photovoltaic MCT (Kolmar KLD-0.1-J1/208) with a ZnSe window and a spectral bandwidth of 750cm⁻¹ – 3000 cm⁻¹. For the SrTiO₃ (STO) sample we use a liquid nitrogen cooled broadband photoconductive MCT (Infrared Associates FTIR-22-0.100) with a spectral bandwidth of 400 cm⁻¹ – 5,000cm⁻¹. This is a similar detector to the one used with the Bruker in the far-field but has a 0.1 mm x 0.1 mm element size, a KBr window with moisture-resistant coating, and a preamp with 1 MHz bandwidth. Due to the lower detectivity of the broadband photoconductive MCT compared to the narrowband photovoltaic MCT, we used a larger 50 nm radius tip (PPP-NCSTAu) to enhance the near-field signal when measuring the STO sample.

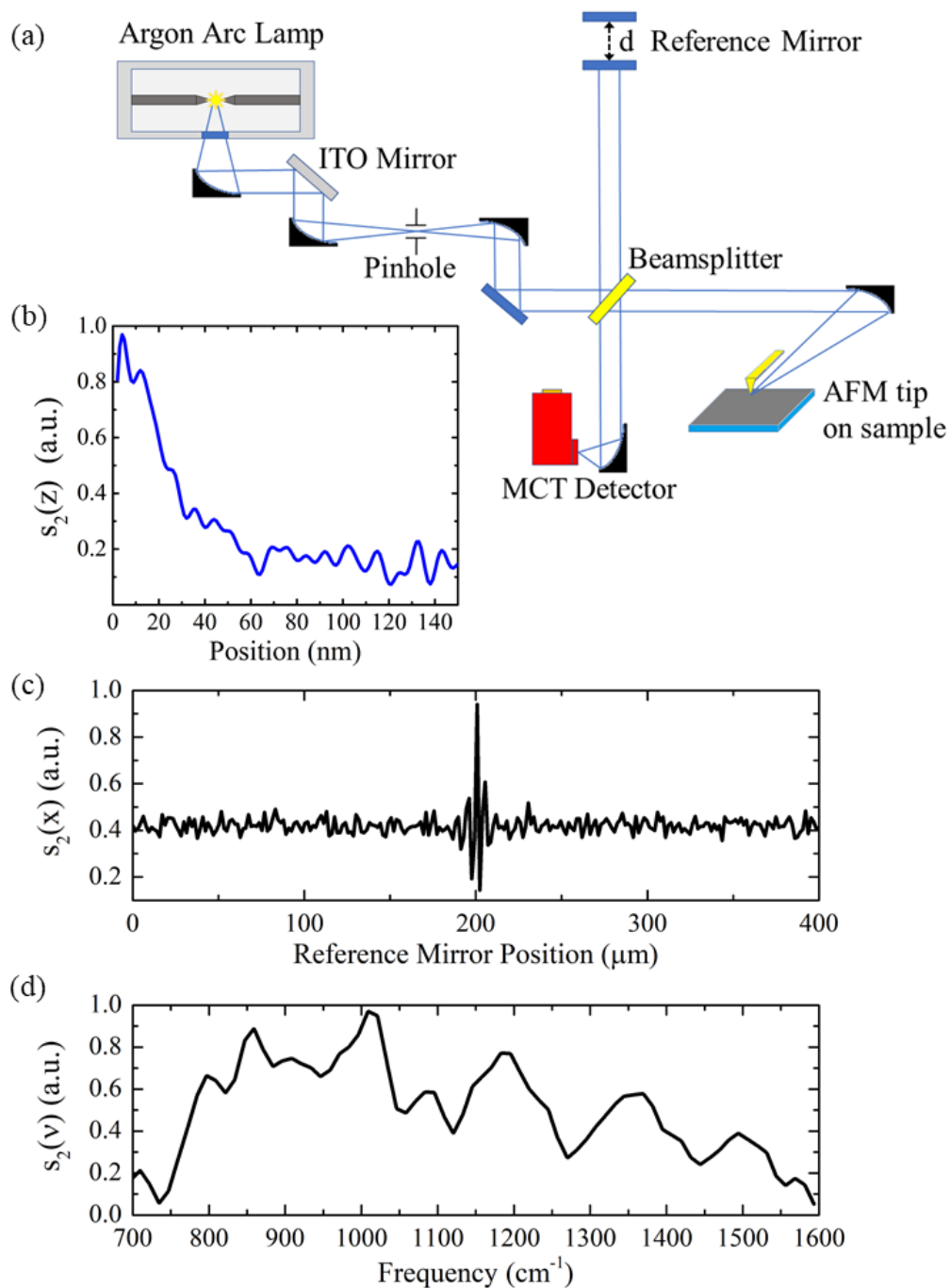


Fig. 3.3 **(a)** Schematic of the beam path used. **(b)** Approach curve obtained at the second harmonic with the reference arm set to the white light position (position of the peak in **(c)**). **(c)** Near-field interferogram on gold demodulated at the second harmonic obtained with the argon plasma light source and optical setup shown above and **(d)** the resultant spectrum generated by fast Fourier transformation of the interferogram.

The AFM is operated in tapping mode which modulates the infrared signal at the tapping frequency and higher harmonics of our tip. The tapping frequency ($\tilde{\nu}$) of the Arrow-NCPT is ~ 250 kHz while the tapping frequency of the PPP-NCSTAu is ~ 120 kHz. Since the near-field signal scales non-linearly with tip-sample distance, it is also present in the higher harmonics ($n\tilde{\nu}$) of the cantilever oscillation frequency. The far-field background scattering from the tip-cantilever-sample system is suppressed by demodulating our signal at higher harmonics of the cantilever oscillation frequency [8]. We demonstrate that we exclusively measure the near-field signal by taking an approach curve on gold which is shown in Fig. 3.3(b). This approach curve is obtained by setting the reference arm to the white light position (the position of maximum constructive interference) and recording the signal as we retract the sample away from the tip. This demonstrates the expected non-linear decay in the near-field infrared signal (s_2) demodulated at the second harmonic of the AFM tip oscillation frequency. To record our spectra on gold, Si, SiO₂ and STO, we move the reference mirror a total distance of $400 \mu\text{m}$ i.e. $200 \mu\text{m}$ on both sides of the white light position. This leads to an optical path difference of $400 \mu\text{m}$ yielding a spectrum with a resolution of 25 cm^{-1} . Fig. 3.3(c) shows an interferogram recorded over gold with the Arrow-NCPT tip and Kolmar photovoltaic MCT. Fourteen scans were averaged with a 200 ms reference mirror step time taking 256 total data points per scan resulting in a total acquisition time of ~ 12 minutes. Fig. 3.3(d) is the resultant spectrum generated by fast Fourier transformation of the interferogram.

3.3 Results with the APLS:

Firstly, we demonstrate that the spatial resolution of our setup is on the order of the AFM tip diameter and not limited by the diffraction limit of the tip illumination wavelength. We set the reference arm to the “white light position” i.e. the position of maximum constructive interference. We then take an AFM topography scan (Fig. 3.4(a)) across the edge of 100 nm of SiO₂ on silicon. The second harmonic of our near-field signal is simultaneously recorded (Fig. 3.4(b)). Although SiO₂ has a phonon-polariton resonance, the total integrated signal of silicon is higher than the total integrated signal of SiO₂. This contrast can be explained by the higher average refractive index of silicon (in the wavelength range of the incident infrared radiation) when compared to SiO₂ [41]. By taking a line trace across this border we see that while the topography line trace (Fig. 3.4(c)) shows a decrease in height when going from SiO₂ to Si, the near-field signal (Fig. 3.4(d)) has a sharp increase within about 50 nm, well below the diffraction limit of the range of mid-infrared wavelengths that are illuminating the tip.

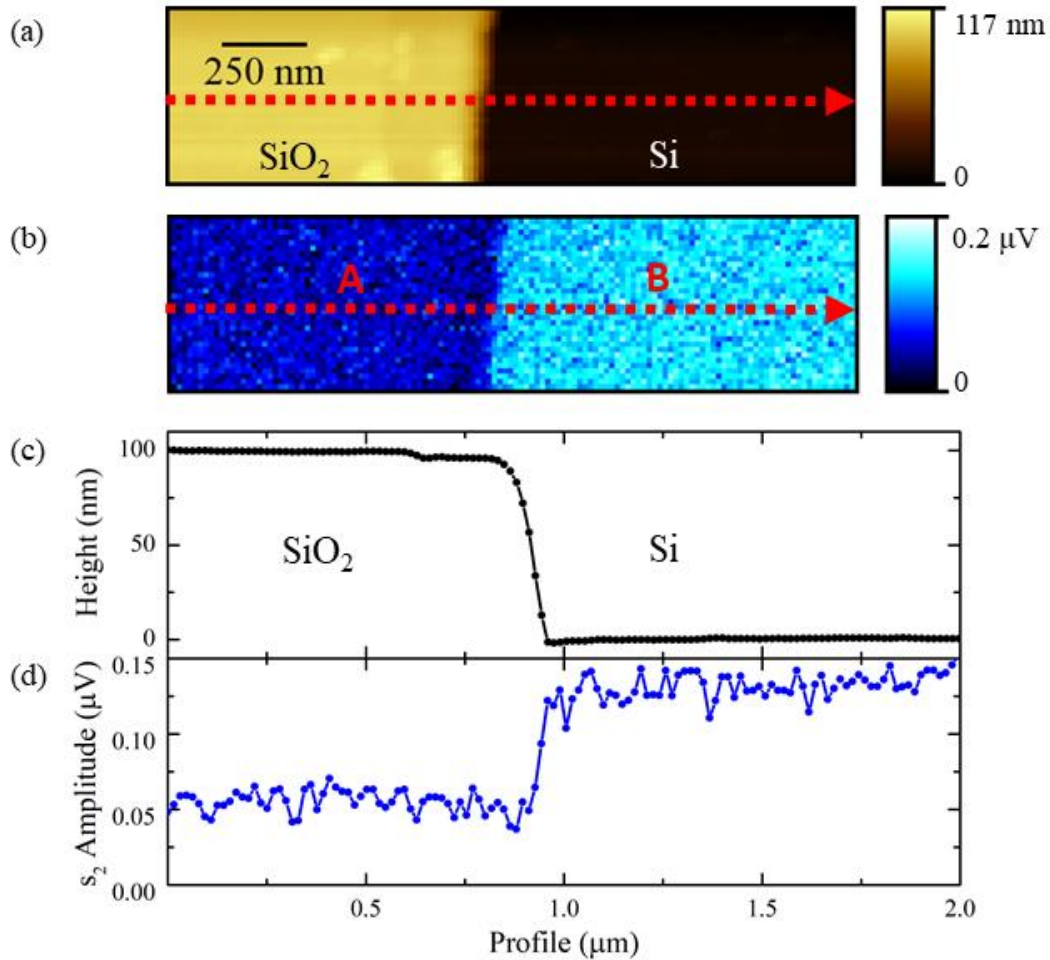


Fig. 3.4 **(a)** Topography and **(b)** the second harmonic near-field amplitude at the white light position obtained simultaneously on 100 nm thick SiO₂ on silicon. Each pixel represents an area of 15 square nanometers. The total integrated signal over all wavelengths is higher for silicon so it will have a higher amplitude in the near-field scan. **(c)** represents a line trace (red dashed line) averaged over 4 consecutive horizontal lines on the topography scan while **(d)** represents the same location for the near-field scan. In **(d)** we can see that moving off the SiO₂ step and onto the Si substrate there is a sharp increase in signal over about 50 nm which is about two orders of magnitude below the diffraction limit of the tip illumination wavelength range. The change in the near-field signal is solely due to the difference in the dielectric function of Si and SiO₂ and not due to a change in the height between the two materials.

To demonstrate the APLS capability as a broadband light source for nano-spectroscopy, the tip was centered at the positions indicated by the red letters in Fig 3.4(b). Figure 5 represents the spectrum of SiO₂ normalized to a Si reference spectrum. Data was obtained at the second harmonic demodulation using a 15 nm radius tip with a tapping amplitude of 65 nm, and spectral resolution of 25 cm⁻¹. The near-field infrared amplitude (Fig. 3.5(a)) shows the well-known phonon polariton that peaks at 1130 cm⁻¹ agreeing well with other measured results [37,41,43]. We are also able to resolve phase data (Fig. 3.5(b)) with our nano-spectroscopy setup and both our amplitude and phase data have the expected semi-quantitative agreement with the point dipole model and finite dipole model (see appendix A) [8,55].

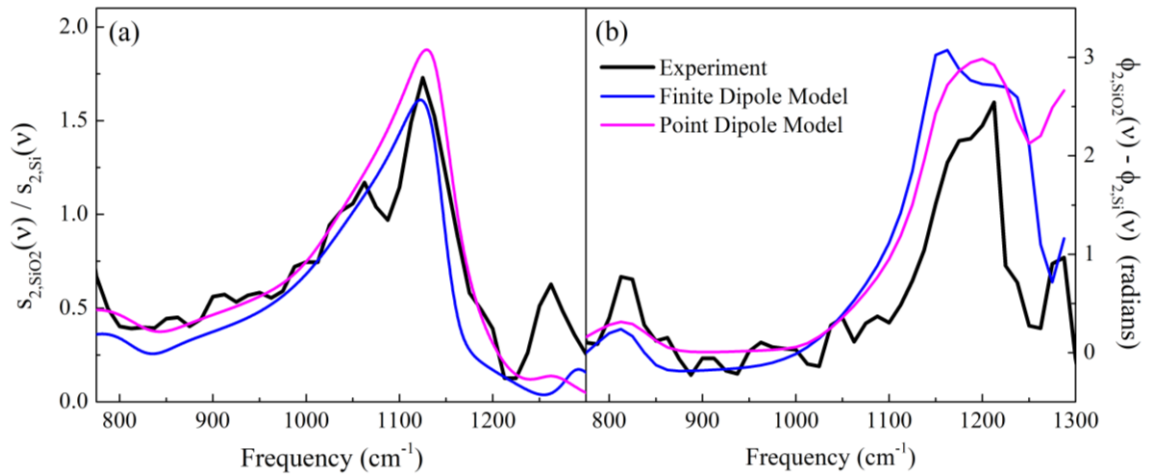


Fig. 3.5 Near-field amplitude **(a)** and phase shift ϕ **(b)** of 100 nm of SiO₂ normalized to Si. The location of these point spectra are represented approximately by the red letters in figure 3.3(b). The SiO₂ spectra were collected at point A and normalized to a spectrally flat silicon spectrum taken at point B. Comparing the experimental data (black) to the point dipole model (magenta) and finite dipole model (blue) we can see a semi-quantitative agreement.

To study the near-field spectrum of STO with reference to gold, 70 nm of gold was deposited on to a portion of a bulk STO substrate. The STO amplitude and phase shift were acquired and then normalized to data from the gold film. Here we used a 50 nm radius tip, 75 nm tapping amplitude, and spectral resolution of 25 cm^{-1} . The STO near-field amplitude and phase shift data is plotted in Fig. 3.6 with the inset in Fig. 3.6(a) demonstrating that we can see the resonance in the second, third, and fourth harmonics. Due to the significant suppression of the background at these higher harmonics, we can conclude that the peak is a near-field resonance. A peak in the normalized near-field infrared amplitude is seen around 640 cm^{-1} in Fig. 3.6(a). The finite dipole model matches the experimental amplitude better than the point dipole model. However, the experimental phase shift plotted in Fig. 3.6(b) is in better agreement with the point dipole model. The quantitative differences between the experiment and the models can be attributed to one or more of the following reasons: the more prominent noise level in this spectrum due to the lower signal-to-noise from the wider band photoconductive MCT; atmospheric absorption due to water vapor and CO_2 below 700 cm^{-1} ; the 25 cm^{-1} spectral resolution; the models being simplified versions of tip-sample near-field interaction, and hence only giving a semi-quantitative estimate of the magnitude and position of the near-field resonances (see appendix A); and the uncertainty in the measurements of the dielectric function of STO in published sources. Note that our experimental data shows a clear resonance peak, and to our knowledge, this is the first experimental demonstration with S-SNIM of a near-field phonon polariton resonance in STO.

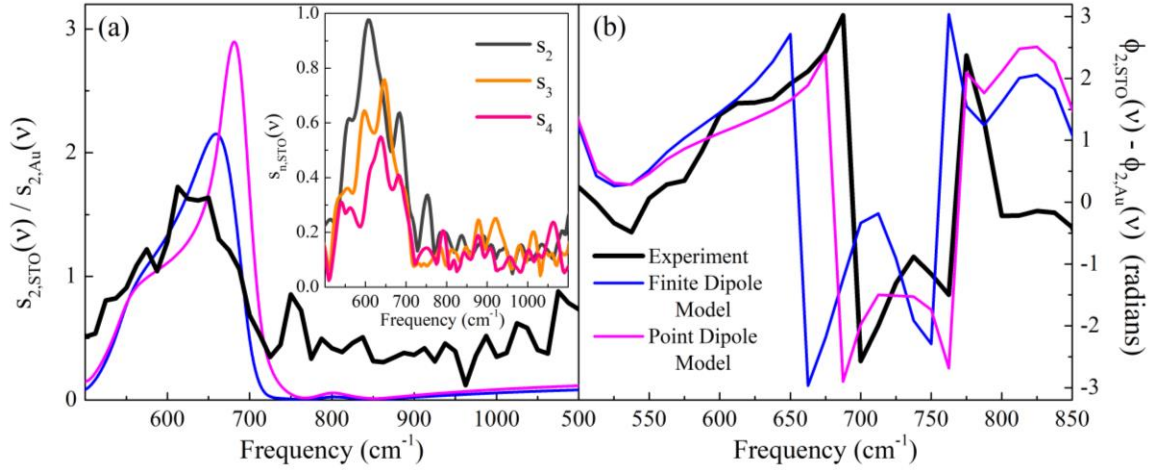


Figure 3.6 **(a)** Phonon polariton resonance of STO normalized to a gold reference (black) compared to the point dipole model (magenta) and finite dipole model (blue). In the inset we show the non-normalized second, third, and fourth harmonic near-field spectra on STO demonstrating that this resonance persists in the higher harmonics. **(b)** Phase shift of the near-field infrared signal on STO normalized to the gold reference and compared to the point dipole model (magenta) and finite dipole model (blue). The phase shift is constrained to values between π and $-\pi$.

3.4 APLS Summary and outlook

With the introduction of our APLS, we have demonstrated that it is a highly broadband infrared light source capable of being used for nano-spectroscopy from the far-infrared to the mid-infrared spectral range. Sub-diffraction limit point spectra and near-field images were obtained at the second harmonic optical demodulation demonstrating the phonon-polariton resonance in SiO_2 with very good agreement consistent with previously published literature. The expected phonon-polariton that occurs in bulk STO was experimentally observed to occur around 640 cm^{-1} . We

have demonstrated that our nano-spectroscopy set up can take spectra down to 500 cm^{-1} , the cutoff imposed by the ZnSe beamsplitter. Currently the upper limit seems to be the atmospheric absorption bands which occur above 1400 cm^{-1} . Future improvements that will be implemented include enclosing the entire near-field set up in dry, CO_2 -free air. This will reduce atmospheric absorption and will extend our spectral range past the atmosphere lines above 1400 cm^{-1} . Moreover, there is potential for implementing other combinations of detectors, beam-splitters, and infrared transparent windows in the future to explore the spectrum of the APLS in the sub- 500 cm^{-1} spectral range. This will enable acquisition of near-field spectra of lower frequency phonons in many materials.

3.5 Extending the APLS to the far-Infrared

The nano-spectroscopy setup consists of our home-built argon plasma light source and a commercial s-SNIM instrument from Neaspec GmbH [58]. The argon plasma light source is an electrode stabilized plasma that is housed inside a sealed water-cooled aluminum vessel with an infrared transparent window to allow access to the mid- and far-infrared wavelengths emitted from the plasma via bremsstrahlung radiation. We now use a potassium bromide (KBr) window for acquiring the Au and STO data and a ZnSe window for the SiO_2 and Si data [58]. The vessel is pressurized with 3-15 psi (gauge) of high purity argon gas. A high voltage pulse between the two electrodes ignites an arc discharge that is sustained with a current of about 7 Amps.

The light from the hot spot of the argon plasma is collected and collimated by an off-axis parabolic (OAP) mirror with a 2-inch focal length. It is then reflected at a 45° angle of incidence off an indium tin oxide (ITO) coated glass mirror. This transmits much of the unwanted near-infrared and visible radiation and reflects the mid- and far-infrared radiation from the plasma. The reflected beam is then focused through a 500 μm pinhole by an OAP mirror with a 4-inch focal length. This helps to improve the spatial coherence of our beam and ensures we are collecting light from the hot spot of the plasma. The beam is then recollimated using an OAP mirror with a 1-inch focal length setting the beam diameter to about 10 mm. We measure a beam power of 1.3 mW after the pinhole in the spectral range between 400 cm^{-1} and 5,800 cm^{-1} . The s-SNIM setup is based on an atomic force microscope (AFM) employing a metallic coated AFM tip and an asymmetric Fourier Transform Infrared (FTIR) interferometer. The incoming collimated beam is incident on a KRS-5 beam splitter for a 400 cm^{-1} cutoff. The beam splitter reflects part of the beam to a moveable reference mirror and transmits the other part to a parabolic mirror that focuses the beam onto a platinum-iridium coated AFM tip with a radius of curvature of ~ 60 nm for the STO/Au spectra. The scattered signal is then collected with the same parabolic mirror and is recombined with the reference beam at the beam splitter and brought to a focus at the detector. For the Au and STO data we use an Infrared Associates (FTIR-22-0.100) MCT photoconductive detector with an active area of 1×10^{-4} cm^2 , a noise equivalent power of 0.84 $\text{pW Hz}^{-1/2}$, a spectral bandwidth of 400 cm^{-1} – 5,000 cm^{-1} and a preamp with a 1 MHz bandwidth. This liquid nitrogen cooled MCT photoconductor element is housed in

a dewar with a KBr window with moisture-resistant coating. The AFM is operated in tapping mode with a tip oscillation frequency $\tilde{\nu} \approx 250$ kHz and a typical tapping amplitude is 80-90 nm. The tip oscillation modulates the scattered infrared signal and allows suppression of the background when demodulated at harmonics $n\tilde{\nu}$ of the tip oscillation frequency $\tilde{\nu}$, where the demodulation order $n = 2, 3, 4$ [8,29]. After demodulation, we obtain a scattering amplitude s_n and scattering phase ϕ_n . To eliminate unwanted signal fluctuations caused by atmospheric absorption lines we encased the entire beam path and microscope in a dry and CO₂-free air purge. Figure 3.7 shows a spectrum on STO that was taken with this new low frequency cutoff. We observe a sharper peak in STO at 425 cm⁻¹ below our previous cutoff of 500 cm⁻¹ as well as the peak at ~675 cm⁻¹ seen previously. This data was modeled with the point dipole model which did not give a reasonable match. This is due to the strongly resonant behavior STO has in the near-field which can be seen with the low frequency mode exceeding the response of gold by ~4 times at the second harmonic. In order to properly model this data full wave numerical simulations were performed using an accurate model of the tip used in experiment with an electromagnetic solver software called FEKO. The full details of our numerical modeling developed for s-SNIM are covered in Ref. [59] and summarized briefly in appendix A. Using these models, we see that the two peaks correspond with the two reststrahlen bands that occur in this spectral range for STO. The high frequency band occurs between 542 cm⁻¹ (TO) and 792 cm⁻¹ (LO) oxygen related modes while the lower frequency band is between the 179 cm⁻¹ (TO) and 472 cm⁻¹ (LO) titanium and strontium related modes [60].

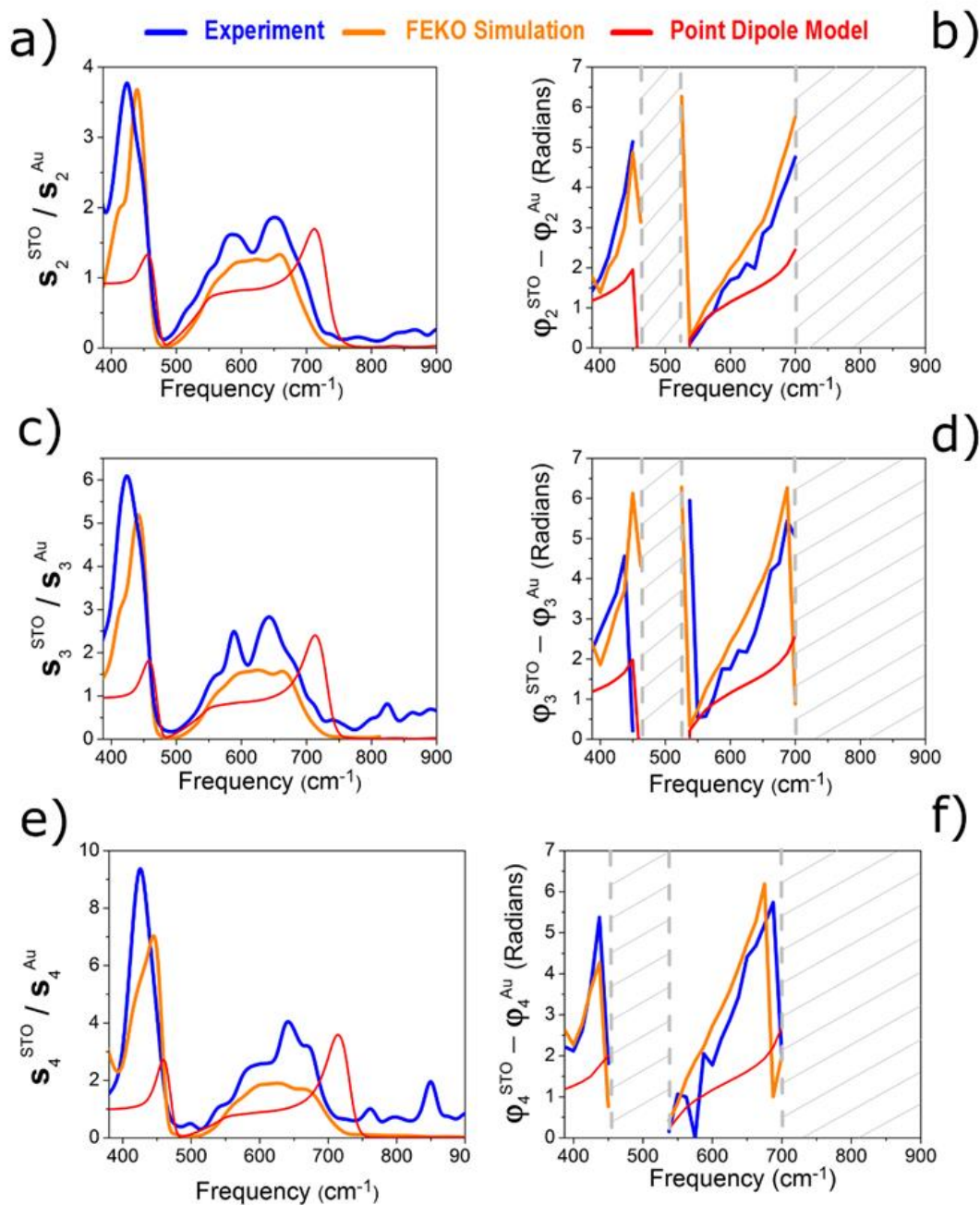


Figure 3.7 (a-f) Plots show the experimental results, numerical simulations, and point dipole model calculations of the $n = 2, 3, 4$ near-field infrared amplitude and phase of STO normalized to the spectra on gold. The phase is indeterminate in the spectral regions depicted by the gray hatched areas because the scattering amplitude from STO is negligibly small in these spectral regions.

3.6 The Laser Sustained Xenon Plasma Light Source

We developed a table-top laser-sustained plasma light source to provide the necessary high intensity broadband radiation for hyper-spectral broadband nano-spectroscopy and nano-imaging. This is a direct upgrade to our previously described argon plasma light source. [58,59,61] A schematic of the experimental setup can be seen in Fig. 3.8(a). Similar to the previous version of the light source, the upgraded light source is comprised of an aluminum vessel with windows for optical access and tungsten electrodes for igniting the plasma. This vessel is pressurized between 15 – 20 atmospheres gauge of high purity Xenon gas. A high voltage pulse generates an arc across two electrodes which is then sustained by a constant current. The upgrade consists of a near-infrared diode laser with a ~ 1 μm wavelength in the vicinity of a strong xenon line and incident power of ~ 85 W. The laser light is brought to a focus in the gap between these electrodes where the plasma is being sustained by the electric current. The current is then terminated, and the plasma is sustained by the laser at its focus yielding a highly stable and brilliant broadband infrared source. The aluminum vessel has two anti-reflective coated quartz windows: one window allows us to couple the laser to sustain the plasma and the other window allows the unabsorbed laser light to be terminated at an external beam dump after passing through a beam splitter that sends a small portion of the intensity to a power meter to measure the laser power transmitted through the plasma. A CVD diamond window is clamped to the pressure vessel via a viton O-ring. This material allows access to the broadband infrared radiation of the plasma into the mid- and far-infrared spectral range while providing the

necessary thermal and mechanical properties necessary to seal the pressure vessel.

There are major advantages of incorporating the laser to sustain the plasma. In the current- sustained plasma, a significant portion of the power is dissipated by the heat conducted by the electrodes. The advantage of sustaining with a laser is that the power is more efficiently transferred to useable broadband radiation while increasing the lifetime of the light source by significantly lowering the overall usage time of the electrodes. Secondly, the plasma becomes more localized to the focus of the laser, allowing a smaller emission volume which is advantageous for microscopy. For this experimental set-up, a 200 μm pinhole is used with a total transmitted power of ~ 1.2 mW measured in the beam after the pinhole in the spectral range between 400 cm^{-1} and $5,800\text{ cm}^{-1}$. This is a >5 times increase in power emitted per unit area compared to our current driven APLS.

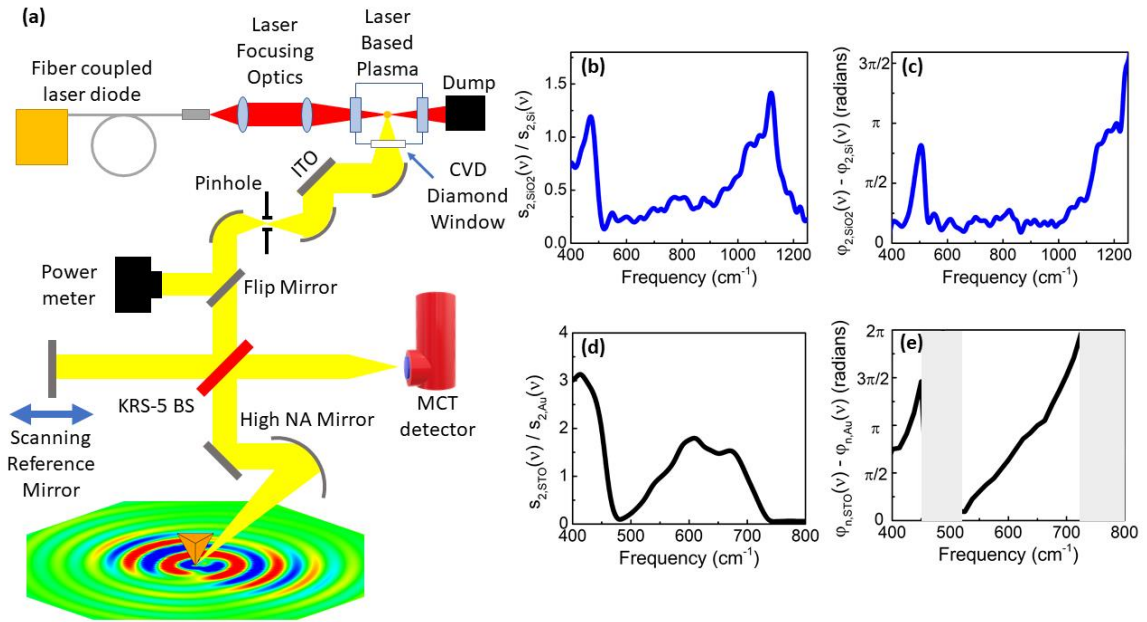


Figure 3.8 **(a)** Schematic of the beam path used in our LSLS system with the red representing the near-IR laser used to sustain the plasma and the yellow representing the broadband radiation from the plasma. Broadband nano-spectra obtained with the LSLS setup on 100 nm SiO₂ on Si showing amplitude **(d)** and phase **(e)**. The commonly observed resonance at 1130 cm⁻¹ is observed as well as an additional low frequency resonance at 460 cm⁻¹. Amplitude **(d)** and Phase **(e)** of bulk STO far (>500) from the Au reference showing a peak at ~420 cm⁻¹ and a broader peak at ~675 cm⁻¹.

Figure 3.8 (a) shows a schematic of the beam path for the laser sustained light source (LSLS) as well as the beam path for the nano-spectroscopy experiment. First, a calibration sample was studied to observe a known phonon polariton resonance in SiO₂. The area of the sample studied consisted of a ~100 nm layer of SiO₂ over Silicon. We obtain the ultrabroadband near-field spectrum over the 400 cm⁻¹ – 1250 cm⁻¹ range which resolves two separate SPhP resonances that occur in SiO₂ seen in the amplitude and phase [Fig. 3.8 (b) and

(c) respectively]. The higher lying resonance is the 1130 cm^{-1} that has been characterized in many other near-field works [40,41,58,59] while the lower lying resonance at 460 cm^{-1} has only been observed by s-SNIM utilizing an infrared Synchrotron beamline in conjunction with a liquid helium cooled Ge:Cu photoconductor [15]. Our observation of this lower lying mode with our tabletop LSLS demonstrates the powerful utility of this source for far-infrared near-field spectroscopy. We then move to bulk STO that has a 225 nm thick Au layer on part of the sample. We obtain amplitude and phase spectra [Fig. 3.8 (d-e)] on STO very far ($>500\text{ }\mu\text{m}$) from the Au edge to characterize the near-field spectrum of STO. We see the two SPhP resonances that have been observed previously on bulk STO with the sharper low frequency resonance occurring at $\sim 425\text{ cm}^{-1}$ and the broader high frequency resonance occurring at $\sim 675\text{ cm}^{-1}$ [59].

3.7 The signal-to-noise comparison of the plasma sources

Due to the small scattering cross section of the tip, it is necessary to have high intensity light sources but it is also necessary for them to have low noise. Since the signal to noise ratio can be dependent on things like the detector detectivity, light source, tip, and various other parameters of the system we will use a normalized SNR (NSNR) to compare the APLS and LSLS with each other. The NSNR can be defined as [62]

$$NSNR = \frac{\frac{\text{Signal Power}}{\text{rms noise}}}{(\delta\tilde{\nu})\sqrt{t}} \quad (3.1)$$

where $\delta\tilde{\nu}$ is the spectral resolution and t is the integration time to acquire the spectrum. To do a proper comparison, we use data where all other components are the same such as the detector, tip, and material the tip scanned over. We use the gold reference spectra taken with the APLS and the LSLS used to normalize the STO spectra in Fig. 3.7 and Fig. 3.8(d) respectively. Figure 3.9 shows 100% lines of the second and third harmonic compared for each plasma light source over our spectral range of interest.

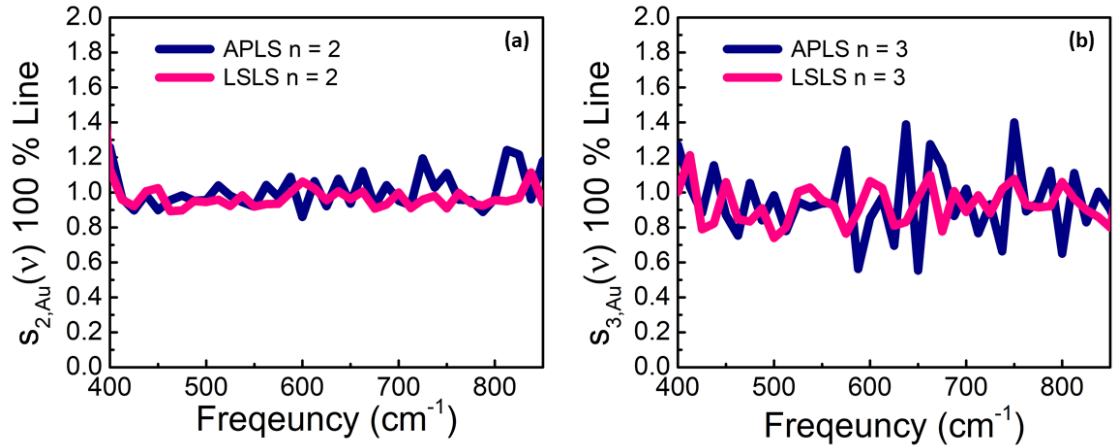


Figure 3.9 100% lines taken on over Gold with s-SNIM demodulated at the (a) second and (b) third harmonics comparing the noise in the APLS and LSLS.

Both spectra were taken at $\delta\tilde{\nu} = 12.5 \text{ cm}^{-1}$ and the APLS gold spectra were integrated for 120 minutes while the LSLS spectra were integrated for 55 minutes. In the range of 400 cm^{-1} to 850 cm^{-1} , using Eq. (3.1) we obtain a NSNR for the APLS of 0.009 for $n = 2$ and 0.0045 for $n = 3$. For the LSLS we obtain 0.026 for

$n = 2$ and 0.013 for $n = 3$. For both harmonics we observe an ~3-fold increase in the NSNR of the LSLS spectra over the APLS spectra. This is a great improvement but less than the expected 5-fold increase predicted by the intensity emitted per unit area of the LSLS over the APLS. We attribute this discrepancy to convective noise in the LSLS. Since the APLS operates at an argon gas pressure of 1 atmosphere gauge and the LSLS operates at a xenon gas pressure of 15 – 20 atmospheres gauge there is more convection present in the LSLS since convection has a strong pressure dependence. The hot plasma heats up the gas and causes the more buoyant hot gas to rise. This movement of gas around the pressure chamber causes ripples in the profile of the plasma which result in a slight but persistent random modulation in intensity of the collected light. Improvements that could reduce this convection are to properly model and fabricate a sufficiently small inner volume of the pressure cell to decrease the motion of the gas due to heat and its resultant convection.

Chapter 4:

Far-infrared surface phonon polariton propagation in STO

4.1 Introduction

Polaritons are quasiparticles formed from the strong coupling of photons with excitations of materials such as surface plasmons, phonons, and excitons [10,63–65]. Polaritons have already made significant impact to many areas of research including efforts towards room temperature Bose-Einstein condensation [65,66], superfluidity and quantized vortices [67,68], room temperature polariton lasers [69,70], all optical transistors [71], and efficient energy conversion [72]. Plasmon and exciton polaritons have demonstrated utility from the mid-infrared through visible. However, as the wavelengths get further into the less explored far-infrared and terahertz spectral range limitations are caused by the lack of available detectors and sources. It is in the far-infrared and terahertz spectral range that the surface phonon polariton (SPhP) shows great potential to carry over the technological advantages of plasmon-polaritons. Surface Phonon Polaritons result from bound charges in polar dielectrics coupling with incident photons. Thus SPhPs are different from surface plasmon polaritons (SPPs), which are a coupling

of free electrons in metals to photons. SPhPs occur at set wavelengths dictated by the optical phonons of the polar dielectric, which predominately take place below 1000 cm^{-1} . SPhPs already have proven applications such as coherent thermal emission [73], enhanced light-matter interactions [34], high-density IR data storage [74], metamaterials [75–77], and terahertz wave generation [78]. Recently, a first of its kind electrically pumped SPhP based laser, emitting at $\lambda = 26.3\text{ }\mu\text{m}$ ($\sim 380\text{ cm}^{-1}$), has been demonstrated [16].

SPhP spectra have recently been experimentally resolved in STO, a polar dielectric that exhibits a diverse range of electronic and optical properties that make it an exciting technological material [58,59,79,80]. STO is transparent to visible light with a band gap of $\sim 3.2\text{ eV}$ while having excellent ferroelectric, dielectric, and optoelectronic properties [60,81,82]. Upon doping with electrons, either through niobium or iron doping or via oxygen vacancies, STO can transition to a stable metallic state [83–90]. Furthermore, STO can support exotic states such as superconductivity and a two-dimensional electron gas [91–94]. As a cubic perovskite, STO is common substrate for lattice matching or to provide strain to a number of functional oxide films such as the ferroelectric BaTiO_3 as well as the high temperature superconductor $\text{YBa}_2\text{Cu}_3\text{O}_{7-\delta}$ [95]. Due to STO being such a common substrate for functional oxide systems, many advancements have been made in obtaining low impurity and high crystalline quality bulk samples as well as treatments to produce high quality surfaces. Despite all the research already proving STO as a powerful functional material, very little work has been done towards realizing the potential of STO as an infrared nanophotonic platform. Only

recently has STO been put in perspective as a unique polar dielectric in the infrared due to its ability to support both a mid-infrared SPhP and a far-infrared SPhP [59,96]. Most work discussing STO has been constrained to the mid-infrared, only covering the higher frequency SPhP without probing wavelengths longer than a free space wavelength of $\sim 20 \mu\text{m}$ [79,80,97]. Interestingly, it is STO's optical properties at longer infrared wavelengths that demonstrate its promise as a far-infrared nanophotonic material.

In both cases of SPPs and SPhPs, the condition for a propagating surface wave is that the real part of the dielectric function is negative while the imaginary part is small. In polar dielectrics, this is located between the transverse optical (TO) and longitudinal optical (LO) phonons, called the reststrahlen band. The reststrahlen band is a spectral range where the reflectance becomes like that of metal while keeping a reduced damping rate and electrical properties of a dielectric due to the absence of free carriers [17]. It is in this range that the real part of the dielectric function becomes negative. The incident electromagnetic field causes the positive and negatively charged lattice sites to coherently oscillate in a direction that leads to an induced electric field that opposes the incident electromagnetic radiation. As a result, electromagnetic radiation in the medium is screened and the propagation into the medium evanescently decays. In addition, the electromagnetic fields propagate along the surface with the wavevector ($k_{SPhP} = 2\pi/\lambda_{SPhP}$) where λ_{SPhP} represents the compressed wavelength of the surface phonon polariton. Fig. 4.1(a) shows the reflectance of STO showing two reststrahlen bands, with the mid-infrared band manifesting between the TO and

LO oxygen phonon modes and the far-infrared band resulting from a combined contribution of the TO and LO phonon modes from the strontium and titanium atoms. Fig. 4.1(b) shows the real and imaginary parts of the complex dielectric function showing the reststrahlen bands when ϵ_1 is negative and ϵ_2 is small. It is interesting to note that the low frequency very strong TO strontium mode located at $\sim 87 \text{ cm}^{-1}$ causes ϵ_1 to be negative for a significant portion of the far-infrared spectrum. It is STO's ability to support SPhP modes across this large spectral range that make it a good candidate for far-infrared nanophotonic applications. While many polar dielectric materials support SPhP modes in more narrow regions of the mid- and far-infrared, few support them over such a wide far-infrared and terahertz spectral range. It is this broadband window for SPhPs in the far-infrared combined with STO supporting two separate SPhP branches across the mid- and far-infrared that make the case for STO as a far-infrared nanophotonic solution. Through the application of established techniques such as nanopatterning of geometric structures on the surface, SPhPs in STO should be tunable over a very large window of the far-infrared. For example, it has been shown that localized SPhPs can be tuned across the reststrahlen band by nanopatterning pillars of varying radius on SiC [75]. Applied to STO these methods should allow selective and tunable optical response over the large bandwidth of the far-infrared inside of STO's lower reststrahlen band. STO as a nanophotonics platform paves the way for frequency tailorable far-infrared and terahertz sensors, metamaterials, and coherent far-infrared and terahertz sources.

There exists a mismatch in the momentum needed to excite a SPhP with freely propagating photons. Scattering-type scanning infrared microscopy (s-SNIM) has been proven to be a particularly useful method to directly probe and excite SPhPs [18]. In this method infrared radiation is focused to a metal coated AFM tip which induces strong near-fields at the tip apex. These strong near-fields interact with the sample underneath and this interaction is encoded in the scattered far-field radiation. The AFM tip is operated in tapping mode to extract the near-field interaction from the background contributions [8]. This technique allows nanometer-scale optical properties to be studied at a spatial resolution limited only by the radius of the AFM tip apex [6,98–101]. Due to this high-field confinement, the tip can provide the necessary momentum to excite SPhPs in dielectric materials [102]. This overcomes the momentum mismatch between the incident light, $k = (\omega/c)$, and SPhP momentum:

$$k_{SPhP} = \left(\frac{\omega}{c}\right) \sqrt{\frac{\varepsilon_{SPhP}\varepsilon_a}{\varepsilon_{SPhP} + \varepsilon_a}} \quad (4.1)$$

Where ω is the frequency of incident photons, c is the speed of light, ε_{SPhP} is the complex dielectric function of the medium supporting SPhPs, and ε_a is the complex dielectric function of the ambient medium. Work been done using s-SNIM to characterize polar dielectric materials such as SiC or low dimensional van der Waals materials, e.g. hexagonal boron nitride. s-SNIM has been utilized to excite, launch and observe interference of these SPhPs by either single line laser or broadband techniques. [11,13,27,43,103–108] Most work to characterize and realize applications for these SPhPs has been in the mid infrared ($> 15 \mu\text{m}$) where

there are plenty of detectors and sources compatible with s-SNIM. However, as the SPhP frequency approaches the longer wavelengths ($< 700 \text{ cm}^{-1}$) there is little experimental work [17].

We explore the propagation and interference of the SPhPs on STO by coupling a newly designed laser sustained plasma light source (LSLS) to our s-SNIM set up. This newly integrated light source allows ultrabroadband infrared nano-spectroscopy to be accessed on a table-top experiment down to frequencies as low as 400 cm^{-1} , limited by the detector cutoff. This allows direct access to probe and excite SPhPs with s-SNIM in the broad far-infrared reststrahlen band in STO. We use it to resolve and map propagating SPhP resonances on STO. Additionally, these results are validated using state-of-the-art full wave numerical simulations using a highly accurate full tip geometry demonstrating good agreement between simulation and experiment.

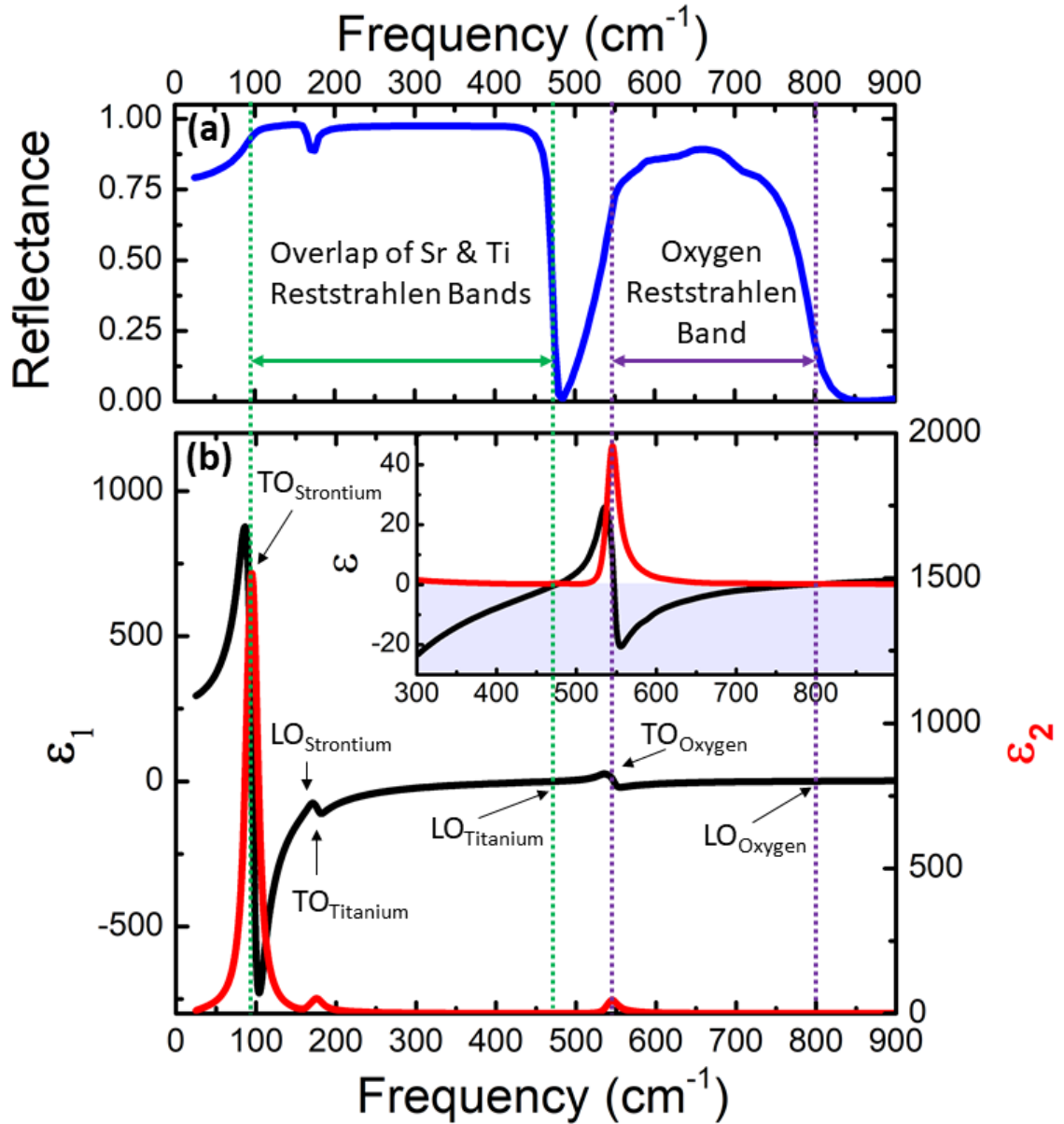


Fig. 4.1 (a) Reflectance of STO demonstrating the two reststrahlen bands. (b) Real and imaginary parts of the dielectric function with the optical phonon modes indicated. The inset shows the zoomed in real and imaginary parts of the dielectric function showing the negative ϵ_1 and low ϵ_2 . The optical constants for STO were taken from Ref. [109]

4.2 Experimental Method

Scattering-type scanning near-field infrared microscopy (s-SNIM) and spectroscopy was performed on STO and SiO₂ samples using a commercial s-SNIM microscope from Neaspec GmbH. By focusing infrared light to the apex of a metal-coated atomic force microscope (AFM) tip, s-SNIM obtains sample information encoded in the scattered light from the tip sample system that is localized to a lateral resolution limited only by the radius of the AFM tip used. [8] Broadband near-field nano-spectra can be acquired with the s-SNIM instrument and the spectra reveal the broadband, frequency-dependent infrared behavior of the sample at nanometer scale spatial resolution determined by the radius of curvature of the AFM tip apex. This method allows us to obtain infrared properties by circumventing the Abbe diffraction limit. It also enables enhanced surface sensitivity when compared to the larger penetration depths of conventional far-field FTIR methods. [13,41,110] As can be seen in Fig. 3.8(a), we take broadband nano-spectroscopy data by coupling the LSLS to the S-SNIM system. Similar to our previous table-top setup [58], the broadband infrared radiation from the plasma is collected and collimated by an off-axis parabolic (OAP) mirror with a 2-inch focal length. It is reflected at a 45° angle of incidence off an indium tin oxide (ITO) coated glass mirror to transmit the unwanted near infrared and visible radiation and reflect the mid- and far- infrared radiation from the plasma. The reflected beam is then focused through a 200 μm pinhole by an OAP with a 4-inch focal length to improve the spatial coherence of the beam. There are multiple advantages of using a pinhole in our system. In S-SNIM, a high numerical aperture mirror both focuses

the incident radiation as well as collects the scattered radiation from the tip. Since the tip has a radius on the order of tens of nanometers, its usable near-field scattered radiation after being collimated by the parabolic mirror is highly spatially coherent due to the small source area. The broadband radiation collected from the plasma is less spatially coherent due to its dimensions being much larger than the tip apex. By focusing the broadband radiation on a pinhole, we improve the overlap of the tip scattered and reference arm radiation that gets focused on the detector element thus maximizing the interference at the detector. After the pinhole the beam is collimated using an OAP mirror with a 1-inch focal length yielding a beam diameter of 10 mm. A power of ~ 1.2 mW is measured in the beam after the pinhole in the spectral range between 400 cm^{-1} and $5,800\text{ cm}^{-1}$ which is obtained after following an alignment procedure to ensure the hottest part of the plasma is being collected. This beam is then incident on a KRS-5 beam splitter with 70% of the beam power transmitting through to a parabolic mirror focusing to the tip sample system of the S-SNIM and 30% of the power reflecting to a movable reference mirror. The tip used is platinum-iridium coated AFM tip with a radius of curvature of ~ 60 nm. The scattered signal from the tip sample system is then recollimated with the same parabolic mirror and recombined with the beam reflected off the movable reference mirror and brought to a focus at a liquid nitrogen cooled Infrared Associates (FTIR-22-0.100) MCT photoconductive detector with an active area of $1 \times 10^{-4}\text{ cm}^2$, a noise equivalent power of $0.84\text{ pW Hz}^{-1/2}$, a spectral bandwidth of $400\text{ cm}^{-1} - 5,000\text{ cm}^{-1}$ and a preamp with a 1 MHz bandwidth. The AFM is operated in tapping mode with a tip oscillation frequency of $\tilde{\nu} \approx 250\text{ kHz}$ and a tapping

amplitude of ~ 80 nm. To suppress the background, the signal recorded by the detector is demodulated at harmonics $n\tilde{\nu}$ of the tip oscillation frequency $\tilde{\nu}$, where the higher harmonics $n = 2, 3, 4$ contain little to no background contamination. After demodulation, we obtain a scattered amplitude s_n and a scattered phase ϕ_n .

To take a spectrum, initially the tip is rastered across the sample surface to map the area to be studied, then the tip is brought into contact at the desired location of the image and the reference arm is scanned a set distance which generates an interferogram. A Fourier transform is applied to this interferogram to generate the near-field spectrum. To eliminate the instrumental features from the spectrum such as the detector responsivity, beam splitter and LSXP emission features, a normalization spectrum is obtained over a spectrally featureless material such as Si or Au. For point spectroscopy, the tip is kept in the same position on the sample and multiple interferograms are averaged to obtain a high signal to noise ratio spectrum. For a spatio-spectral line scan, the tip moves along a set path and at each point, one interferogram is collected. This generates an image where the x-axis is the real space location of the tip and the other axis is the frequency dependence of the near-field at that location. All the spectra in this paper, including the spatio-spectral line scan, are taken with a total optical path difference of $800 \mu\text{m}$ to yield a spectral resolution of 12.5 cm^{-1} . The beam path and S-SNIM system is enclosed in a dry and CO_2 -free air purge to eliminate unwanted spectral features from water and CO_2 .

4.3 Results & discussion

We resolve the propagation and interference of SPhP resonances in STO by obtaining an amplitude and phase resolved spatio-spectral line scan in the vicinity of an Au edge of a height of 225 nm. The spatio-spectral line scan image maps the interference of the tip launched and Au edge launched SPhPs as well as the tip launched, and edge reflected SPhPs. We orient the sample such that the Au edge is perpendicular to the in-plane projection of the tip illumination wavevector. Fig. 4.2(a) shows a basic schematic of how the tip is scanned a distance L away from the Au edge while the broadband illumination, having a focused spot size diameter of $\sim 120 \mu\text{m}$ set by the pinhole, allows simultaneous tip illumination while launching SPhPs from the Au edge. Fig. 4.2 (b) and (c) show the amplitude and phase resolved near-field spatio-spectra line scan showing the two SPhP resonances that occur in STO. As the tip is scanned away from the Au edge frequency dependent interference fringes can be seen in both the resonances. Taking single frequency cuts [Fig. 4.2(d-g)] of the spatio-spectral line scan demonstrate clear fringes in both the amplitude and phase whose fringe spacing decrease with increasing illumination frequency.

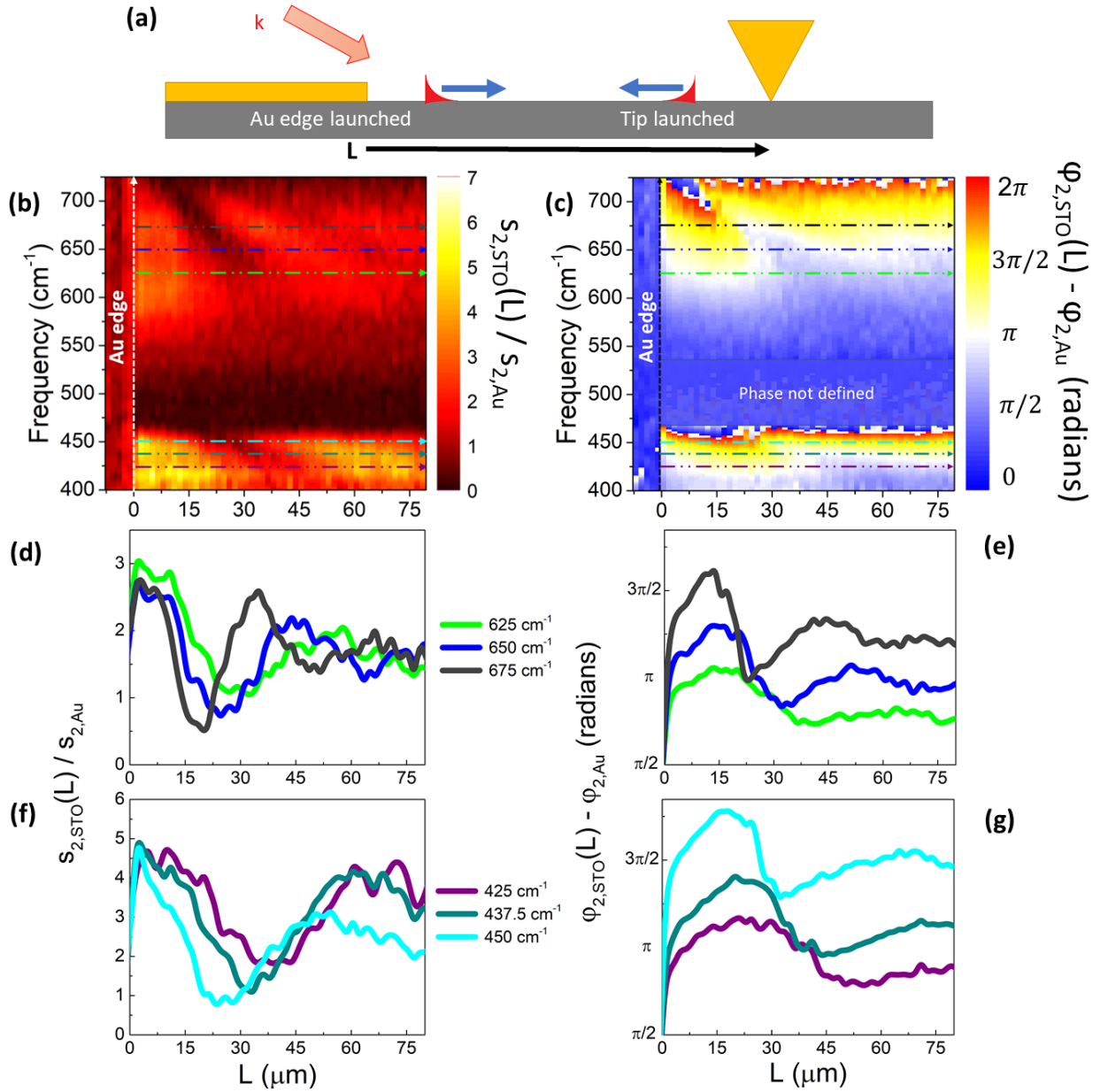


Fig. 4.2 **(a)** Schematic of the experiment measuring the propagation and interference of the SPhPs on STO. The broadband tip illumination launches SPhPs off the gold edge which interfere with the tip launched and Au edge reflected SPhPs. This tip, starting over Au, is scanned away from the Au edge a distance L while the broadband amplitude **(b)** and phase **(c)** spectra are measured and normalized to an Au reference spectrum. Amplitude **(d)** and Phase **(e)** line cuts around 650 cm^{-1} exhibit frequency dependent interference fringe spacings. Looking at amplitude **(f)** and phase **(g)** at line cuts around 437.5 cm^{-1} , longer interference fringe spacings can be observed.

Another way to view this Au edge distance dependent SPhP interference is to look at the spectra as a function of distance. To increase the SNR from the spatio-spectra line scan, point spectra were obtained at select distances from the Au edge in the same location and experimental geometry as the spatio-spectral line scan. Fig 4.3 (a) shows the topography of the STO and Au edge with each dot's color matching the spectrum color in Fig. 4.3(b-g). A clear modulation of the spectrum can be seen in the amplitude and phase. The low frequency peak decreases in amplitude shifts to higher frequency then increases in amplitude while the high frequency peak decreases in amplitude and splits into two peaks with the higher peak decreasing in frequency as distance is increased. This behavior is completely consistent with the spatio-spectral line scan.

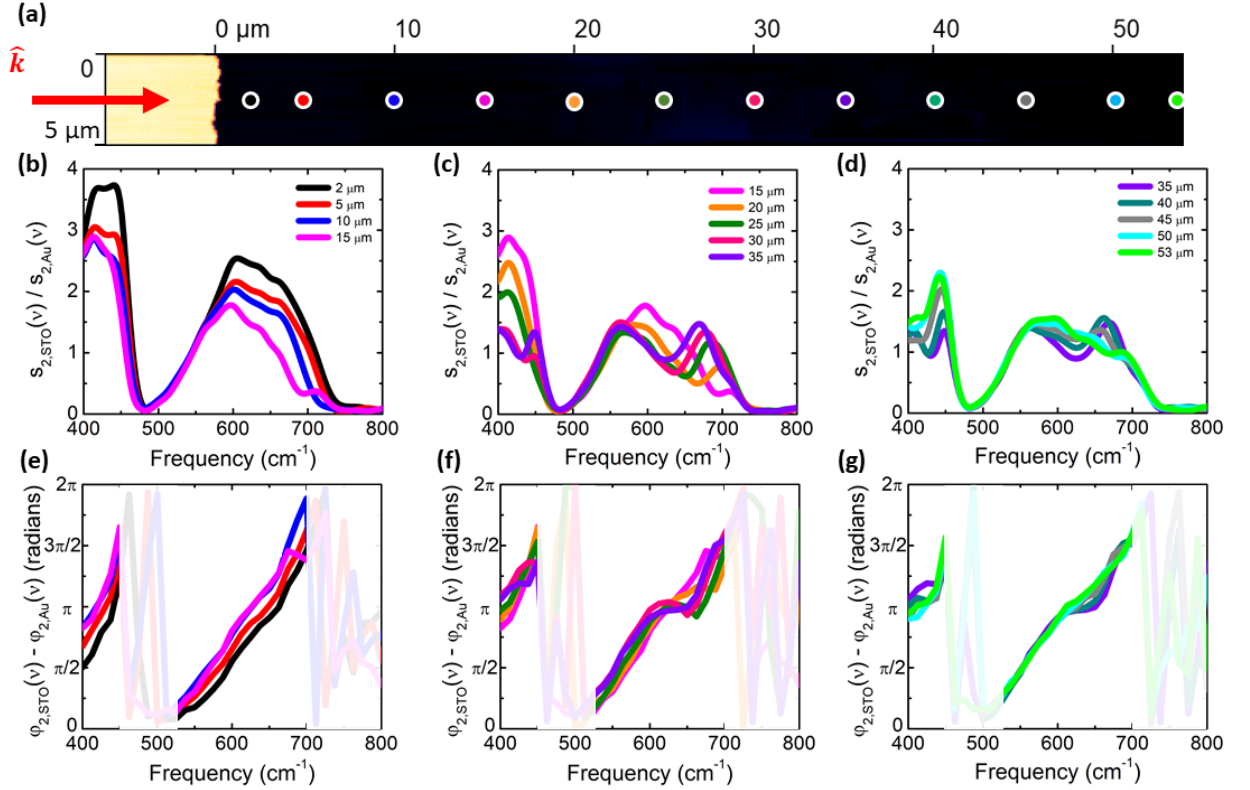


Fig. 4.3 **(a)** Topography scan of gold edge (yellow) and STO (black) with locations of point spectra taken at set distances of from the gold edge. The incident broadband tip illumination reradiation is represented by the red arrow. The amplitude spectra **(b-d)** and phase spectra **(e-g)** exhibit tip-edge distance dependent SPhP interference. The phase spectra become less resolvable where there is insufficient scattered amplitude for STO so this area is greyed out of the phase spectrum. The amplitude exhibits a shifting of the 650 cm^{-1} resonance into two peaks, with the higher frequency peak moving towards 700 cm^{-1} as the tip gold edge distance is increased. The 420 cm^{-1} resonance decreases in amplitude and then shifts higher frequencies, then grows in amplitude while shifting back to lower frequencies. This behavior is seen at higher harmonics as well.

Full wave numerical simulations using FEKO were carried out to model our experiment. The details of this simulation method are described elsewhere [59] but to briefly summarize, the model consists of a realistic geometric model of our tip

tetrahedron with an accurate shaft length of 15 μm and apex radius of 60 nm that is over an infinite half planar Green's function with bulk STO optical constants. The tip is simulated at a sufficient number of heights above the STO surface to simulate the accurate non-linear near-field approach curve and tapping amplitude. The tip is tapped at a frequency of 250 kHz and demodulated at higher harmonics of the tapping frequency as is done in the experiment. This tip was placed near a gold surface of finite dimensions of 400 x 100 μm with a thickness set to the thickness of the Au edge (225 nm) in our experiment with the 400 μm edge perpendicular to the in-plane projection of the incident illumination wavevector taken from experiment. This was done since the physically real situation of an effectively infinitely long gold edge cannot be realized in this simulation due to memory constraints. We chose dimensions of the Au surface such that it was large enough not to cause unwanted effects due to its finite geometry. A plane wave is incident on the system with its wavevector matching the experimental direction of incident radiation. Fig. 4.4(a) shows the simulated tip with the Au edge on STO matching the experimental geometry. Also shown are the tip and Au edge launched SPhPs as electric field oscillations for incident plane wave illumination of 437.5 cm^{-1} . Fig 4.4(b) and (c) show the amplitude and phase of the spatio-spectral line scan data, point spectroscopy data and simulated data showing good agreement in fringe spacing. Fig. 4.4(d) and (e) show the same situation for the 675 cm^{-1} incident frequency. This simulation was carried out for other frequencies with the fringe spacing from experiment and simulation compared in Fig. 4.4(f). Finally, looking at the wavelength of the SPhPs launched from the Au surface in the simulations and

comparing them to the theoretical dispersion relation for isotropic STO, seen in Fig. 4.4(g) calculated from Eq. (4.1), we get excellent agreement.

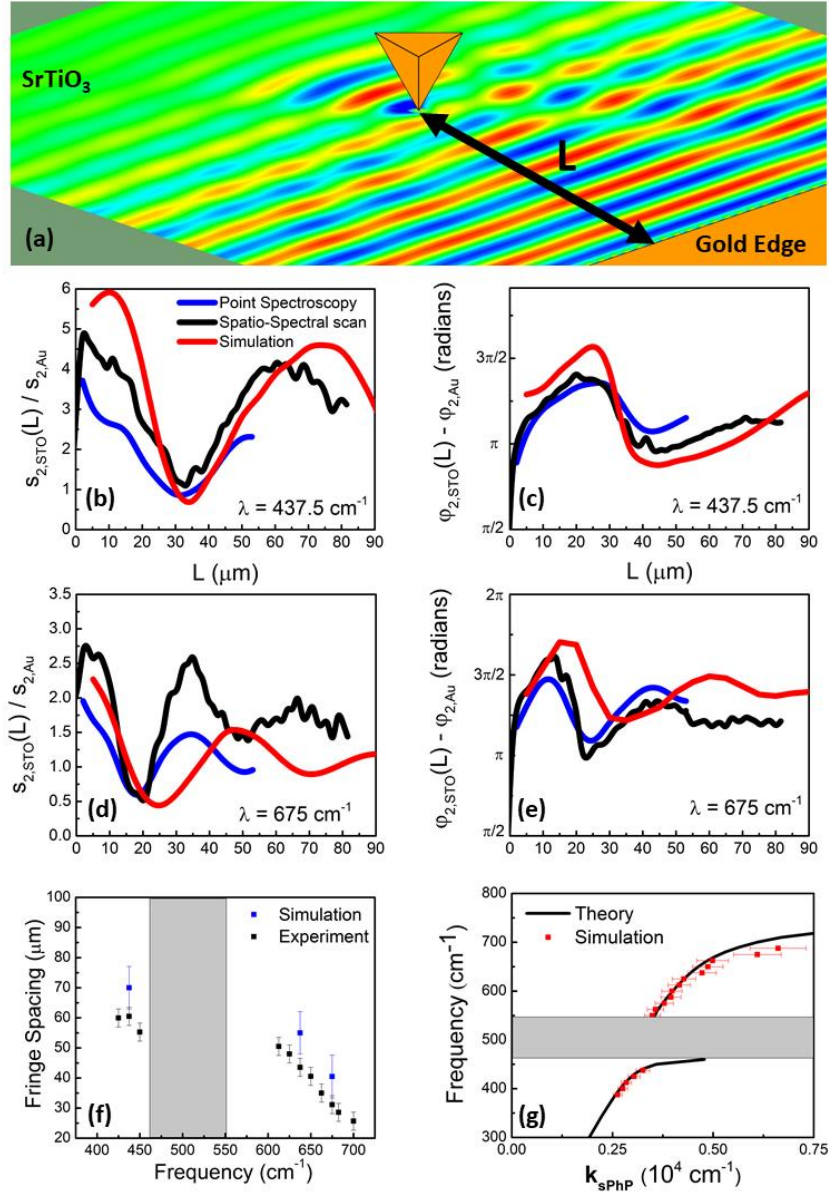


Fig. 4.4 **(a)** Simulated tip with Au edge showing tip and Au edge launched SPhPs as electric field oscillations for incident plane wave illumination with $\lambda = 437.5 \text{ cm}^{-1}$. Measured and simulated amplitude **(b)** and phase **(c)**, at 437.5 cm^{-1} plane wave illumination, for the tip-Au edge distance dependent interference fringes. Amplitude **(d)** and phase **(e)** for the same scenario but with 675 cm^{-1} plane wave illumination. **(f)** Simulated and experimental fringe spacing compared as a function of frequency. **(g)** Theoretical dispersion relation for STO SPhPs compared to the dispersion obtained from numerical simulations of the SPhPs launched from the tip and Au edge.

4.4 Conclusion

In summary, we have characterized propagating SPhPs in STO by introducing a new thermal broadband source based on a laser-sustained plasma that provides sufficient intensity in the far- and mid-infrared for ultrabroadband s-SNIM. We showed that this table-top source, combined with a CVD diamond window, allows the acquisition of nano-spectra into the far-IR. We demonstrate the capabilities of this source by first resolving two SPhP resonances in SiO₂. We then used it to characterize amplitude and phase resolved broadband SPhP propagation and interference in bulk STO. This was then validated by state-of-the-art parameter-free full-wave numerical simulations which considered the complete tip and shaft geometry. This work opens the possibility of STO as a platform for far-IR nanophotonics. Interesting paths forward include spatially confining these SPhPs to thin films or ultrathin membranes [111] of STO as well incorporating subwavelength nanophotonic structures on STO that guide and direct these SPhPs. The laser sustained plasma light source enables a low cost table-top method for far-IR ultrabroadband nano-spectroscopy with future improvements involving alternative detectors with lower frequency cutoffs to delve deeper into the far-IR since the CVD diamond window is transparent to all of the far-IR and terahertz.

Chapter 5:

Mott transition in the rutile insulator VO_2 without Peierls ordering

5.1 Introduction

An insulator-to-metal transition (IMT) is an emergent characteristic of quantum materials. When the IMT occurs in materials with interacting electronic and lattice degrees of freedom, it is often difficult to determine if the energy gap in the insulating state is formed by Mott electron-electron correlations or by Peierls charge-density wave (CDW) ordering. To solve this problem, we investigate a representative material, vanadium dioxide (VO_2), which exhibits strong electron-electron interactions as well as CDW (Peierls) ordering. We have fabricated ultrathin VO_2 films on rutile (001) TiO_2 substrates. These VO_2 films undergo the IMT without the CDW (Peierls) ordering. Infrared and optical measurements discover the Mott-Hubbard semiconductor gap of 0.6 eV in the rutile phase below $T_c \approx 306$ K. Above T_c , we observe a Drude feature along with an increase in the optical conductivity due to a Mott IMT. Our results establish the route to a purely

electronic IMT with profound implications for fundamental and applied studies of this phenomenon.

An insulator-to-metal transition (IMT) leads to dramatic changes in physical properties, and it is induced by variation of control parameters such as temperature, chemical doping, and strain [112]. The underlying mechanism of the IMT is ambiguous in materials in which the IMT is accompanied by a structural phase transition, such as in bulk vanadium dioxide (VO_2) [6,113–117]. Bulk VO_2 undergoes a thermally induced IMT at the intrinsic critical temperature $T_c \approx 340$ K accompanied by a structural phase transition (SPT) between a monoclinic structure and rutile (tetragonal) structure. The high-temperature metallic phase has rutile structure which is viewed as chains of equidistant vanadium atoms along the rutile c_R -axis. The low-temperature insulating phase has monoclinic (M_1) structure that consists of twisted V-V dimers with alternating spacing of $c_R \pm 2\delta$ (distortion) i.e. the CDW (Peierls) ordering. Given the presence of CDW ordering in the M_1 structure, in early works the IMT was considered a Peierls transition [115,116]. However, subsequent experimental and theoretical works demonstrated the significance of electron-electron correlations to the IMT [6,113,114,118]. Some even posited a new kind of Mott insulator whose ground state is the Peierls ordered phase rather than the antiferromagnetic phase expected in classical Mott insulators [119]. Nevertheless, modern theoretical schemes that explain the IMT and the insulating phase have one aspect in common. Specifically, the calculations in the insulating phase of VO_2 are based on the Peierls ordered structure and the V-V dimers are considered a necessity for a quantitative description. Indeed, even

state-of-the art Dynamical Mean-Field Theory (DMFT) calculations, while emphasizing the significance of electronic correlations, use a cluster-DMFT method based on the primacy of the vanadium pairs [119,120]. This is attributed to the complexity of the electron-electron interactions and the CDW instability in the M_1 structure.

On the other hand, VO_2 films grown on rutile (001) TiO_2 substrates in previous experimental works [121–136] provide an opportunity to consider the IMT in a simpler structure. For thicker VO_2 films grown on rutile (001) TiO_2 substrates, the T_c is close to the intrinsic value of ≈ 340 K and decreases as the film thickness is reduced. Much of the previous literature has focused on films thicker than 10 nm and in these films the IMT is accompanied by the SPT [122,131,135]. A few recent papers have provided evidence in films of reduced thicknesses that the IMT is not accompanied by the SPT [123,125,133]. However, these papers did not directly measure the broadband optical characteristics such as the energy gap which is a defining characteristic of the insulating phase below T_c . Nor did they measure the Drude behavior describing the metallic phase above T_c . Hence, the electronic structure of the ultrathin films was unknown.

To address the question about the origin of the energy gap in insulating VO_2 , we have grown films of thicknesses less than 7.5 nm. These films are in the rutile structure and the monoclinic distortion induced by Peierls ordering is absent [126]. This simplifies the problem because what remains to be confirmed is the energy gap of the insulating phase and the Drude behavior in the metallic phase following the IMT. In this paper, we demonstrate a rutile Mott insulator below

$T_c \approx 306$ K (Fig. 5.1a) by observing both the energy gap of 0.6 eV and the absence of the CDW bonding-antibonding optical transition. Furthermore, we observe the Mott IMT via the emergence of the Drude feature above T_c . These observations were enabled by broadband infrared and optical spectroscopy on a 7.2 nm thick VO₂ film grown on rutile (001) TiO₂ substrate by pulsed laser deposition (see Methods for details). Moreover, we compare the optical conductivity spectra of the ultrathin VO₂ film with that of a thick, bulk-like VO₂ film [137].

5.2 Materials & Methods

The ultrathin VO₂ films were grown on rutile (001) TiO₂ substrates at 500°C via pulsed laser deposition. A KrF excimer laser was used to ablate a metallic vanadium target with a pulse energy of 300 mJ and a repetition rate of 10 Hz. The oxygen pressure was maintained at 20 mTorr while growing and cooling of the sample.

To highlight the growth quality of VO₂, as well as evolution of its properties across the phase transition, both electrical and structural measurements were performed as a function of temperature. The electrical resistance of the films was acquired using a conventional four-probe system (JANIS CCS-450) equipped with a resistive heater to provide the sample heating up to 350 K. The temperature values were measured by two silicon diode thermometers integrated with an automatic temperature controller. The crystalline structure of the insulating and metallic VO₂ was evaluated by variable temperature X-ray diffractometer

(RIGAKU, D/MAX-2500) using Cu K α radiation with an operating voltage of 40 kV and current of 300 mA. The sample was heated up with a rate 1°C/min and stabilized for 3 mins at a particular temperature prior to performing the continuous theta-2theta scans with a 0.01° step. Temperature dependent X-ray diffraction (XRD) measurements on the 7.2 nm thick VO₂ film on rutile (001) TiO₂ substrate are shown in figure A2a in appendix B. An obvious feature from the rutile (001) TiO₂ substrate is seen in the data. There is also a broad VO₂ feature centered at $2\theta \approx 66^\circ$ that is independent of temperature indicating that the ultrathin VO₂ film maintains the rutile structure across the IMT.

The ultrathin VO₂ film used for optical measurements is 7.2 nm thick as determined by grazing-angle X-ray reflectivity (XRR) measurement (See appendix B, Fig. A2b). Grazing-angle XRR measurements were obtained with a Panalytical Empyrean X-ray diffractometer. Atomic Force Microscopy (AFM) scans reveal the film's surface to be very smooth with an rms roughness of 0.2 nm. Epitaxial growth was confirmed by transmission electron microscopy (TEM) (see Fig. 5.1). For TEM experiments, thin samples that are transparent to electrons were prepared by a focused-ion beam technique using Ga ions as a polisher. The microstructural characterizations were done via cross-sectional observations of VO₂/TiO₂ with High-Resolution TEM operated at 300 kV. The obtained images were analyzed with DigitalMicrograph software (Gatan Inc.).

Spectroscopic ellipsometry at 70° and 75° angles of incidence was performed on the 7.2 nm thick VO₂ film on rutile (001) TiO₂ substrate and on the pristine rutile (001) TiO₂ substrate for photon energies 0.6 – 6.5 eV (4,800 cm⁻¹ to

52,000 cm^{-1}) using the Variable-Angle Spectroscopic Ellipsometer (VASE) from J. A. Woollam Co., Inc. The ellipsometry data was complemented by mid- and far-infrared spectroscopy measurements performed in normal incidence transmission and near-normal incidence reflectance geometries from photon energies 50 meV to 740 meV (400 cm^{-1} to $6,000 \text{ cm}^{-1}$) in a Bruker Vertex 80v Fourier Transform Infrared (FTIR) spectrometer. For all spectroscopy measurements, the sample temperature was varied and monitored using a Lakeshore temperature controller, resistive heaters, silicon diode thermometer, and home-built heating stages to take data above and below T_c .

Kramers-Kronig consistent oscillators were employed in the substrate model to fit the ellipsometry, transmission and reflectance data on the pristine TiO_2 substrate using W-VASE software from J. A. Woollam Co., Inc. Next, the ellipsometry, transmission and reflectance data from the ultrathin VO_2 film on the substrate was modeled by adding a 7.2 nm thick VO_2 layer to the TiO_2 substrate model. The data was fit using Kramers-Kronig consistent oscillators in the VO_2 layer. Thus, we obtain the broadband dielectric function of the VO_2 film above and below the IMT temperature (see figure A3 in Appendix C). The real and imaginary parts of the dielectric function are used respectively to obtain the imaginary and real parts of the optical conductivity. Due to the ultrathin nature of the film, we do not observe VO_2 phonon features in the mid- and far-infrared reflectance spectrum which is dominated by the phonons of the TiO_2 substrate.

Scattering-type Scanning Near-Field Infrared Microscopy was performed in the nano-imaging mode utilizing Pseudo-heterodyne interferometric detection [29]

to map the near-field of the VO₂ as a function of temperature. S-SNIM was also performed in the nano-spectroscopy mode in conjunction with a homebuilt laser sustained xenon plasma as the broadband infrared source allowing spectra to be obtained down to 400 cm⁻¹ at 12.5 cm⁻¹ spectral resolution. For nano-imaging, the tip, (Nanoworld, Arrow NCPT) has a radius of curvature of ~20 nm, and for nano-spectra the tip (Neaspec, nanoFTIR) has a radius of curvature of ~60 nm for enhanced signal-to-noise. The data of set temperatures was obtained by implementing a homebuilt heating stage in the same fashion as the far-field spectroscopy.

5.3 Results & discussion

An ultrathin VO₂ film on rutile (001) TiO₂ substrate was imaged by Transmission Electron Microscopy (TEM). Fig. 5.1b shows that the crystalline pattern of the film in real space is the same as that of the substrate demonstrating epitaxial film growth. The reciprocal space selected area electron diffraction (SAED) patterns from a region in the TiO₂ substrate and a region in the VO₂ film are compared in Figs. 5.1c and 5.1d. The SAED patterns from the substrate and the film are the same. These data are consistent with a previous observation that the first ≈ 7.5 nm of a thick VO₂ film grown on rutile (001) TiO₂ is in the rutile structure [126]. Moreover, ultrathin VO₂ films grown on rutile (001) TiO₂ are locked in the rutile structure [123,125,133,138]. Thus, our VO₂ film in the insulating phase at room

temperature has the rutile structure and the complexity in the electronic structure due to CDW is reduced.

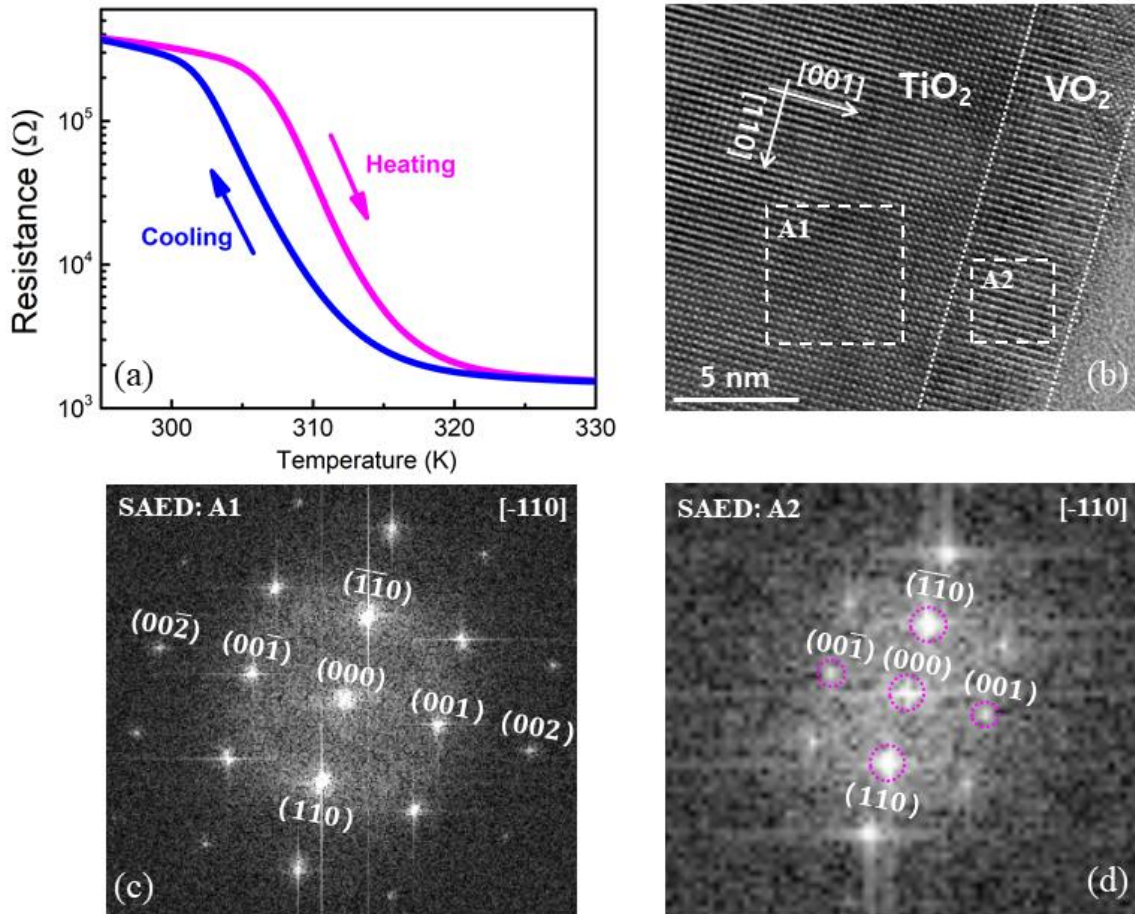


Fig. 5.1: **(a)** Temperature dependent resistance of ultrathin VO₂ on rutile (001) TiO₂. The magenta and blue curves are obtained while heating and cooling the sample respectively. **(b)** TEM image of the VO₂/TiO₂ interface demonstrating clear epitaxial growth. Selected area electron diffraction (SAED) images of white dashed rectangle (A1) in TiO₂ **(c)** and (A2) in VO₂ **(d)** from the TEM image in **(b)**.

Broadband infrared and optical spectroscopy was employed to determine the real and imaginary parts of the frequency-dependent dielectric function in the metallic and insulating phases of the 7.2 nm rutile VO₂ film grown on rutile (001) TiO₂ (see appendix C, Fig. A3). From the dielectric function, we obtain the optical conductivity. The real part of the optical conductivity (σ_1) is related to the imaginary part of the dielectric function by the equation: $\sigma_1 = \omega \varepsilon_2 / (4\pi)$ in CGS units [139]. We plot σ_1 in SI units ($\Omega^{-1} \text{cm}^{-1}$) in the insulating and metallic phases in figure 5.2a. Peaks in optical conductivity can be attributed to direct optical transitions from a filled band to an empty band. The spectrum below T_c in the insulating phase of the ultrathin VO₂ film shows the feature β centered at 1.3 eV and defines an energy gap (E_g) of 0.6 eV below which the optical conductivity is suppressed. The feature β is due to optical interband transitions between the filled, lower a_{1g} band to the empty e_g^π band (see figure 5.3). We also observe a feature ξ with band center 3.2 eV and a feature κ with a band center of 4.4 eV in the optical conductivity of the insulating phase. When this is compared to the optical conductivity spectrum measured in a thick, bulk-like VO₂ film in the insulating, M_1 structure (Fig. 5.2c), the similarities include the existence of features X and Z which are similar to features β and ξ respectively. It is remarkable that the energy gap in rutile, insulating VO₂ is the same as in monoclinic (M_1) insulating VO₂. This already demonstrates that Peierls ordering is not responsible for the energy gap leading to the conclusion that the energy gap is due to electron-electron interactions. The differences are the absence of feature Y with band center 2.5 eV and the presence of feature κ in the insulating, rutile VO₂ conductivity spectrum. The feature Y in

the spectrum of the insulating, M_1 phase shown in Fig. 5.2c is known to be due to optical interband transition between the bonding and anti-bonding bands due to the CDW (Peierls) ordering of V-V dimers [120,121,137]. This indicates that the ultrathin VO₂ film has rutile structure without CDW ordering as also proven by the analysis of the TEM image in Fig. 5.1b, d. The feature κ in the spectrum of rutile, insulating VO₂ is due to optical interband transitions between lower Hubbard band (LHB) and upper Hubbard band (UHB). The feature κ is not evident in the spectrum of insulating, M_1 VO₂ (Fig. 5.2c) because the Hubbard bands are weaker, and their spectral weight is transferred to CDW feature Y. The feature ξ (and Z) at ~3.2 eV is attributed to optical transitions from the filled O_{2p} band to the empty e_g^π band and from the filled a_{1g} band to the empty e_g^σ band [121,137,140–142].

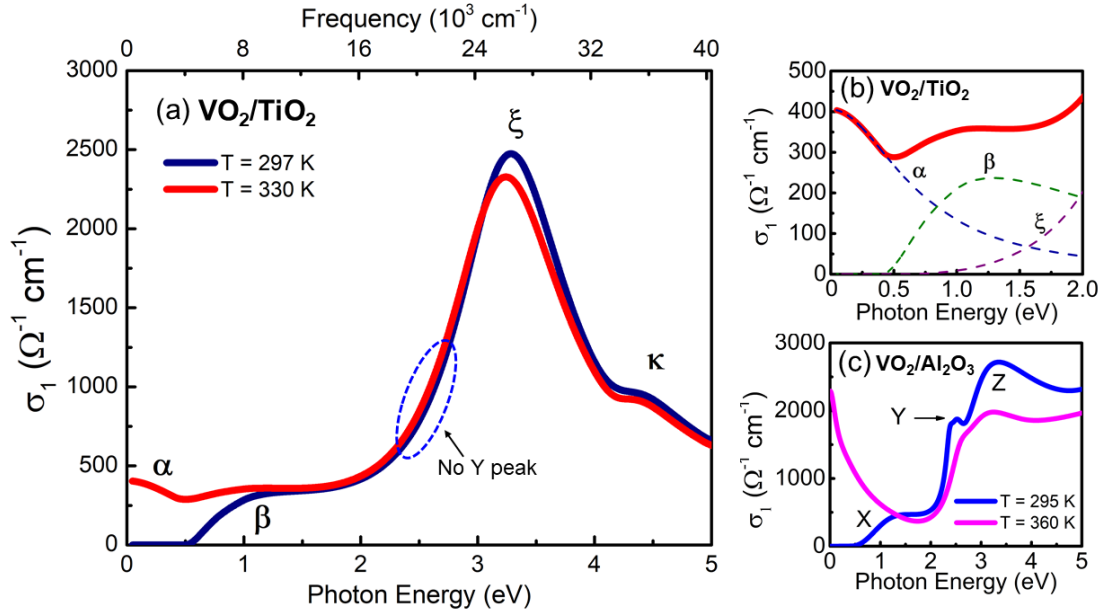


Fig. 5.2: **(a)** Real part of the optical conductivity (σ_1) for the insulating (dark blue) and metallic (red) phases of the 7.2 nm thick VO₂ film on rutile (001) TiO₂ as a function of photon energy. **(b)** Zoomed in low energy region of σ_1 in the metallic phase. The dashed lines representing individual contributions of the free carrier Drude feature, α (blue), and the optical transitions, β (green) and ξ (purple). **(c)** Plot of σ_1 in the insulating (blue) and metallic (magenta) phases of a thick 100 nm VO₂ film grown on ($\bar{1}012$) oriented sapphire (Al₂O₃) taken from Ref. [137].

The optical conductivity spectrum of the metallic state shows that the conductivity in the dc limit ($\omega \rightarrow 0$) is about a factor of 5 lower than in bulk-like VO₂ (see figures 5.2a, 5.2b, and 5.2c). This is primarily because the spectral weight of the free-carrier Drude mode (feature α) in the metallic state is lower compared to bulk-like metallic VO₂ [6,137]. Importantly, we observe an optical interband transition in the near-infrared (feature β) in the metallic state which is similar to that seen in the optical conductivity of the insulating state (see figures 5.2a, 5.2b, and 5.2c). Based on the features α and β in the optical conductivity of the metallic state

of the ultrathin VO₂ film, we propose the following scenario. The weak Drude feature arises from delocalized carriers which appear at the Fermi level as a quasiparticle peak (QP) of mostly a_{1g} character (figure 5.3b). The e_g^π band stays above the Fermi level and is therefore empty. This leads to the interband transition β across the energy gap between filled a_{1g} band and the empty e_g^π band (figure 5.3b). This energy gap occurs in parts of momentum space and can be considered to be a pseudogap. In contrast, bulk VO₂ is metallic in the rutile structure because the Fermi level crosses partly filled a_{1g} and e_g^π bands (see Figure 5.3d). We have considered the possibility that part of the ultrathin film undergoes the IMT to a bulk-like rutile metal leading to an inhomogeneous metallic phase at $T = 330$ K. We performed near-field infrared microscopy experiments (figure 5.4) that are sensitive to in-plane and out-of-plane inhomogeneity [6,143]. However, the near-field infrared data rules out an inhomogeneous metallic phase at $T = 330$ K (see appendix D). The Drude feature and electronic structure of ultrathin rutile metallic VO₂ is different from bulk-like metallic VO₂ due to substrate-induced strain in the ultrathin film.

Further support for the empty e_g^π bands in ultrathin rutile metallic VO₂ comes from the relatively small change in feature ξ between the insulating and metallic states (see figure 5.2a). Feature ξ consists of optical interband transitions from the filled O_{2p} band to the e_g^π band and between the filled a_{1g} band and the empty e_g^σ band. However, it is dominated by spectral weight of the interband transitions from the filled O_{2p} band to the e_g^π band as the optical selection rule favors optical transitions when there is a change of unity in the orbital angular momentum of the

electrons like that between p -orbitals and d -orbitals. In bulk-like VO_2 , there is a drastic reduction in the spectral weight of feature ξ because the empty e_g^π band in the insulating phase becomes partly occupied in the metallic phase (figure 5.2c). Clearly, the relatively small change in feature ξ between the insulating and metallic states in the ultrathin VO_2 film suggests that the e_g^π band is empty in the metallic state and downshifts by about 0.1 eV. Moreover, the spectral weight of feature ξ is shifted to the QP in the metallic phase due to depletion in the density of states of the filled a_{1g} band.

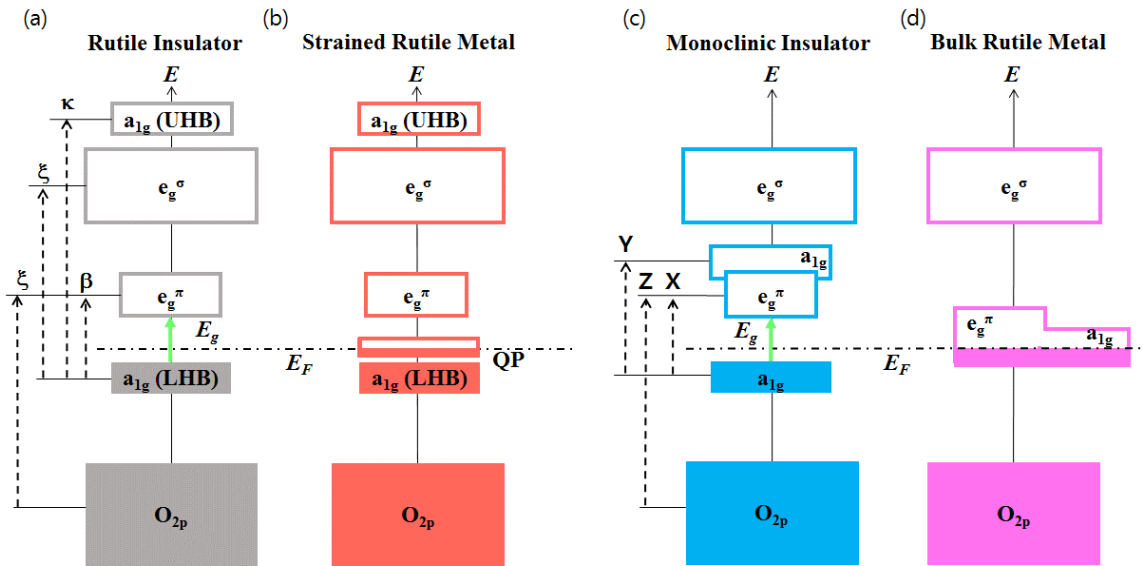


Fig. 5.3: Schematic depiction of the effective band arrangement of the insulating (a) and metallic (b) phases of the ultrathin, rutile VO_2 film based on the features in the optical conductivity labeled in figure 5.2a. Band arrangement of the insulating (c) and metallic (d) phases of bulk-like VO_2 .

The effective number of delocalized carriers per vanadium atom, N_{eff}^{Drude} , in the metallic state can be calculated from the conductivity $\sigma_1^{Drude}(\omega)$ of the Drude oscillator used in the fits to the infrared and optical spectroscopy data (figure 5.2b).

$$N_{eff}^{Drude} = \frac{m_0 V_0 \omega_p^2}{4\pi e^2} = \frac{2m_0 V_0}{\pi e^2} \int_0^\infty \sigma_1^{Drude}(\omega) d\omega \quad (5.1)$$

Here, V_0 is the cell volume of one VO_2 formula unit in the rutile structure and ω_p is the Drude plasma frequency [139]. The delocalized carriers are assumed to have free-electron mass (m_0). We find that the plasma frequency $\omega_p = 1.32$ eV, and ω_p^2 is about four times lower than the value for bulk-like, rutile VO_2 metal. We find that N_{eff}^{Drude} is ~ 0.037 and our calculation of N_{eff}^{Drude} in the ultrathin VO_2 film is a lower bound because it is likely the mass of the delocalized carriers is larger than the free electron mass assumed in the N_{eff}^{Drude} calculation. Using the relaxation time (τ) of the Drude oscillator, we obtain a scattering rate $1/(2\pi c\tau) = 5.6 \times 10^3 \text{ cm}^{-1}$, where c is the speed of light. The scattering rate is notably higher than that seen in bulk-like VO_2 film and this suggests stronger electronic correlations [144].

5.4 Conclusion

Our data indicates that the IMT takes place solely due to change in the strength of electronic correlations in the rutile lattice without the SPT. Hence, the IMT is a pure Mott transition. In general, the Mott transition occurs due to competition between correlation-driven localization and itinerancy. Clearly, temperature is an important

factor in the thermally-driven IMT. Moreover, it is possible that impurities play a role as well [119,145]. Our results will motivate first-principles electronic structure calculations that should be able to elucidate the underlying factors that lead to a thermally-driven Mott IMT in strained, rutile VO₂.

5.5 Continuing near-field study of ultrathin VO₂

Near-field infrared imaging and spectroscopy was performed on the VO₂ sample due to the significantly enhanced surface sensitivity. When compared to the penetration depth of far-field radiation in the mid and far-infrared, the evanescently decaying near-field interaction of the tip and sample has a much smaller (<100 nm) depth dependence [110,143,146]. Initially, single-line nano-imaging was performed on the 7.2 nm VO₂ film through the T_c using s-SNIM with the pseudo-heterodyne interferometric scheme to resolve the nanoscale images [29]. Fig. 5.4 shows clear percolative phase coexistence in the vicinity of T_c but shows uniform insulating and metallic states in the low and high temperatures. This helps to rule out the possibility of the film only being partially transitioned into the metallic state at high temperatures.

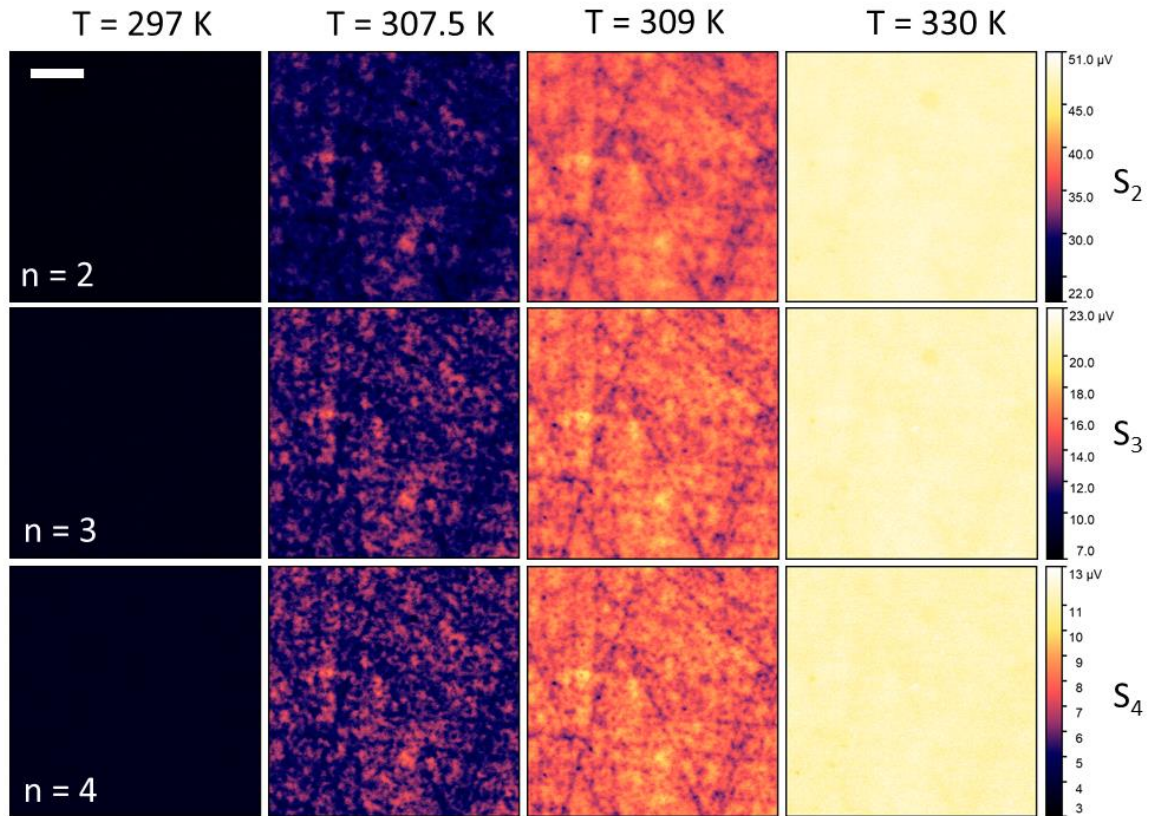


Fig. 5.4 Nano-imaging with s-SNIM of the same area of the film showing phase coexistence in the vicinity of T_c but uniform metallic and insulating phases in the low (297 K) and high temperature (330 K) regions. The white scale bar to the top left represents 1 μm . Data shown is at $n = 2, 3, 4$ with increasing surface sensitivity as the harmonics are increased [146].

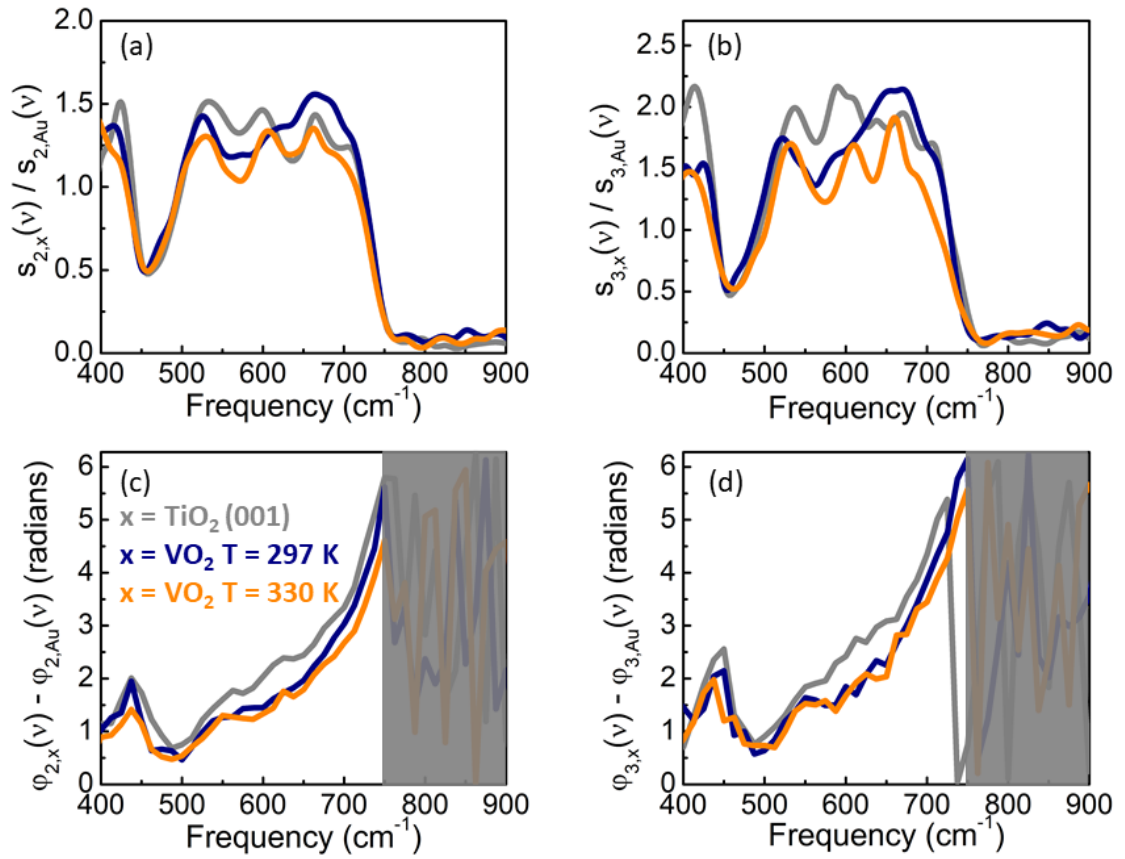


Fig. 5.5 Amplitude **(a, b)** and phase **(c, d)** resolved broadband spectra of the TiO₂ substrate and VO₂ ultrathin film in the fully insulating and metallic states. Data shows a decrease in amplitude from the insulating VO₂ for both $n = 2$ **(a, c)** and $n = 3$ **(b, d)**. Above 750 cm⁻¹ the amplitude goes to zero and the phase becomes undefined.

Broadband s-SNIM was taken on both the TiO₂ substrate and VO₂ film in the fully metallic and fully insulating state (Fig. 5.5). Due to the ultrathin nature of this film, the spectra must be interpreted as a convolution of the substrate and the thin film together. TiO₂ (001) and VO₂ are predicted to have a surface phonon polariton resonances (SPhPs) below 750 cm⁻¹ due to the phonon resonances of these materials in this spectral range. We see in Fig. 5.5 that the amplitude and phase

both show SPhPs as well as a small decrease in the amplitude of the SPhP in metallic VO_2 when compared to the insulating state. This is likely due to the screening of the SPhP by the free electrons in the metallic film. Ideally, the main goal of this experiment would be to use this data to extract the local optical constants to interpret the structure from the locations of the phonon resonances as is done in far-field FTIR. Unfortunately, to accurately resolve the optical constants from this data, numerical modeling is needed as is done in Ref. [59] which can be seen for the isotropic STO in Chapter 3. Numerically modeling our system is made more complicated by the anisotropy in the optical constants of the substrate. Current efforts by other members of our research group are focused toward modeling this experiment on TiO_2 (001) using full wave numerical simulations in conjunction with the High-Performance Computing Cluster at William & Mary. In the near future the modeling of this data should yield the local optical constants of the film.

Chapter 6:

Conclusions & Outlook

This dissertation focused on the interactions of light and matter in quasi-two-dimensional geometries including surfaces and thin films. Hence, s-SNIM and ellipsometry were the major experimental methods used. The development and implementation of a broadband plasma source was a central solution to realizing broadband s-SNIM in the far- and mid- infrared, where the relevant excitations for strongly correlated systems and surface phonon polaritons are located. Initially, this source was realized as a current driven argon plasma. This was then subsequently upgraded to a laser driven xenon plasma resulting in a ~3 times improvement in the SNR while significantly improving the overall lifetime of the light source due to the decrease in usage time of the electrodes. This source was successfully implemented with the s-SNIM system and broadband spectra of surface phonon polaritons were obtained on SiO₂ and STO. By using a KBr window for the argon plasma light source (APLS) and a CVD diamond window for the laser sustained (xenon) plasma light source (LSLS) the low frequency cutoff was extended down to 400 cm⁻¹, a cutoff much lower than all other reported tabletop s-SNIM experiments. This 400 cm⁻¹ cutoff combined with the improved SNR of the

LSLS allowed the real space mapping of Au edge launched SPhPs in STO. Most interestingly, due to the broadband nature of the LSLS, two different modes were measured simultaneously. This interference of SPhPs was reproduced with full wave numerical simulations of the experiment. Further research can realize STO as a far-IR nanophotonics material for applications in metamaterials and coherent thermal radiation at terahertz frequencies.

The strongly correlated electron system, VO_2 , was investigated in a strained state by growing a 7.2 nm film on (001) TiO_2 by PLD. It was determined that epitaxial strain from the substrate removed the monoclinic distortion in the insulating state while a thermally driven insulator to metal transition (IMT) was still observed at a reduced temperature of ~ 306 K. This first-time measurement of the bandgap of rutile insulating VO_2 demonstrated that it maintained its 0.6 eV bandgap despite the absence of the CDW Peierls distortion of vanadium atoms into dimers. This demonstrates that this ultrathin VO_2 film's IMT is a Mott transition. Far-field optical and infrared spectroscopy uncovered a modified band structure that did not change significantly from insulator to metal, save for the band gap collapsing to a weaker Drude feature compared to bulk metallic VO_2 . It is already clear that there is interesting physics occurring in this film at the nanoscale considering the phase coexistence near the transition temperature. Broadband s-SNIM has been obtained but the means to properly model it and extract the optical constants are still being developed. Soon, that data will be modeled to extract the complex optical constants of the ultrathin film. This data will likely provide key insights into the electronic and vibrational properties of rutile VO_2 .

The LSLS has significant potential as a broadband source for optical and infrared spectroscopy in both the near- and far-field. Further improvements that can be applied are remodeling the inner geometry to reduce convective noise. Additionally, the low frequency cutoff is imposed entirely by the choice of detector given that the CVD diamond window is transparent well below 400 cm^{-1} all the way into the radiofrequency spectral range. Faster detectors sensitive to sub 400 cm^{-1} frequencies could open the tabletop broadband S-SNIM experiment's capability to probe a multitude of low energy excitations and collective modes at the nanoscale. Eventually, this source could be implemented wherever there is need for ultrabroadband high intensity photon sources. Infrared micro spectroscopy and infrared ellipsometry could benefit from this source in much the same way as our s-SNIM setup.

Appendices

Appendix A: Near-field simulation methods

For far-field optics based on reflectance, transmission, and ellipsometry it is possible to directly solve for the complex frequency dependent optical constants by way of the Fresnel coefficients. Due to the coupling of the incident light to the tip, simulations must be used to model the s-SNIM amplitude and phase to extract the material properties. Initially, this has been done by using simplifying approximations to the tip geometry to make the problem more tractable. The tip can be simplified to either a sphere at the apex (centered at point A of figure A1a) or an ellipsoid (extended between point A and B of figure A1a) [13]. The simplest model is to approximate the tip as sphere inscribed in the apex of the tip and is referred to as the point dipole model [8,13]. In the electrostatic approximation $a \ll \lambda_{\text{inc}}$, where a is the radius of a sphere on the order of tens of nanometers, the effective polarizability over an infinite substrate as a function of the gap distance has an analytic form. The scattered field, E_{scat} , from equation 2.2 in chapter 2 is proportional to the effective polarizability α_{eff} ,

$$E_{\text{scat}} \propto \alpha_{\text{eff}} = \frac{\alpha(1+r_p)^2}{1 - \frac{\alpha\beta}{16\pi(a+z)^3}} \quad (\text{A1})$$

where $\alpha = 4\pi a^3 \frac{\epsilon_t - 1}{\epsilon_t + 1}$, $\beta = \frac{\epsilon - 1}{\epsilon + 1}$, r_p is the Fresnel reflection coefficient of the sample for p-polarized light, and z is the gap distance between the probe apex and the sample surface. Here, α is the polarizability of an isolated sphere with the complex dielectric function ϵ_t , and β is the response function of the material with complex dielectric function ϵ .

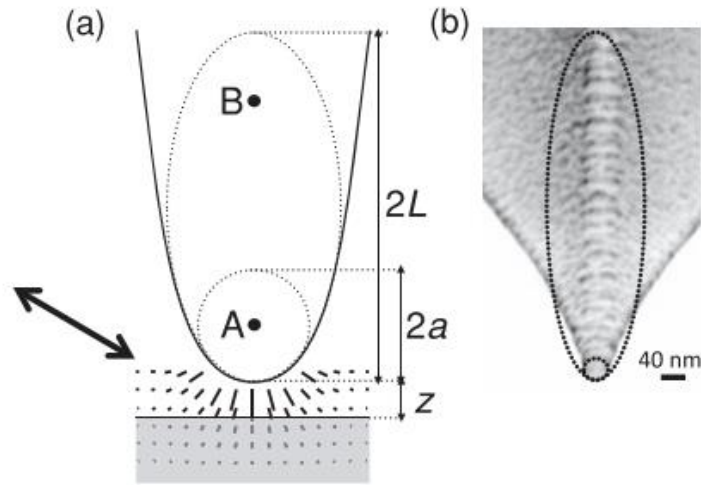


Fig. A1. Taken from Ref. [13]. **(a)** schematic of the point dipole and simple dipole regions over the sample (grey) showing a vector field demonstrating the tip enhanced optical field under the tip. **(b)** SEM image of a s-SNIM tip and shaft with the point dipole region and finite dipole ellipsoid overlaid. This tip has an apex diameter of 40 nm.

The other way the tip geometry is simplified is to use an ellipsoid and this is called the finite dipole model [13,32,55]. It assumes the tip charges are distributed through an ellipsoid of length $2L$ with the distribution of charge being dependent on the tip sample distance. It also requires experimental data to be obtained where the scattered intensity at the higher harmonics as a function of z , called an approach curve. This approach curve is fit by varying the shaft length $2L$ and a complex valued parameter, $g = g_1 + ig_2$, related to the approximate fraction of charge contributing to the near-field, to get a good match. These parameters are then used with the finite dipole's analytic prediction for its effective polarizability

$$\alpha_{\text{eff}} = (1 + r_p)^2 \frac{a^2 L (\epsilon_t - 1) \left(2L \sqrt{1 - a/L} + a \ln \frac{(1 - \sqrt{1 - a/L})^2}{a/L} \right)}{2\sqrt{1 - a/L} \left((L - a\epsilon_t) - aL(\epsilon_t - 1) \ln \frac{(1 - \sqrt{1 - a/L})^2}{a/L} \right)} \quad (\text{A2})$$

$$\times \left(2 + \frac{(gL - a - z)\beta \ln \frac{L}{z + 3a/4}}{(z - gL + 3a/4)\beta \ln \frac{L}{z + a/2}} + L \ln \frac{L}{a/4} \right).$$

The point dipole model is useful for qualitative modeling of near-field spectra and the finite dipole model can be more quantitatively accurate but requires experimental data to extract values for L , g_1 , and g_2 . To quantitatively model near-field data, especially in the vicinity of strong resonances such as SPhPs, one must perform full wave numerical simulations. Numerical simulations for modeling near-field spectra have been developed by our lab and are described in detail in Ref. [59]. To summarize, scanning electron microscope images of the tip used in

our s-SNIM system were obtained and accurately modeled using computer-aided design (CAD). This tip model was then imported to a proprietary computational electromagnetic solver for arbitrary bodies called FEKO that has a CAD interface. The material for the tip model was chosen to be a perfect electrical conductor and it was placed over half-planar/multilayer Green's function that contained the optical constants of the material studied with s-SNIM. This tip sample system was simulated using the method of moments and surface equivalence principle with plane wave illumination incident on the tip along the same direction as the experimental incident radiation. This was simulated at a number of different tip-sample distances to simulate the tapping amplitude and frequency. The scattered signal, E_{scat} , is simulated by taking the simulated scattered field as a function of tip position and frequency and parametrizing them to be periodic. The higher harmonics are then extracted by expanding our the simulated E_{scat} into a Fourier series. Simulating both a reference material and the material of interest, we apply the normalization in the same way as experiment to compare our simulations and experiment.

Appendix B: Ultrathin VO₂ film X-ray characterization

Temperature dependent X-ray diffraction (XRD) measurements on the 7.2 nm thick VO₂ film on rutile (001) TiO₂ substrate are shown in figure A2a. Apart from the obvious feature from the rutile (001) TiO₂ substrate, there is a broad VO₂ feature centered at $2\theta \approx 66^\circ$ that is independent of temperature. Grazing incidence X-ray reflectivity (XRR) measurements were obtained with a Panalytical Empyrean X-ray diffractometer on the VO₂ thin film at room temperature. The XRR measurements established that the film is 7.2 nm thick (Figure A2b). We used the following equation [138,147] to calculate the film thickness from the XRR data:

$$\lambda = 2t \left[(\cos^2\theta_c - \cos^2\theta_2)^{\frac{1}{2}} - (\cos^2\theta_c - \cos^2\theta_1)^{\frac{1}{2}} \right] \quad (\text{A3})$$

Here $\lambda = 1.54056 \text{ \AA}$ is the x-ray wavelength, $t = 7.2 \text{ nm}$ is the film thickness, $\theta_c = 0.258$ degrees is the critical angle and $\theta_1 = 0.60$ degrees and $\theta_2 = 1.18$ degrees are the angles of the first and second fringe respectively. Nearly identical film thickness is obtained by using the fast Fourier transform (FFT) method [148].

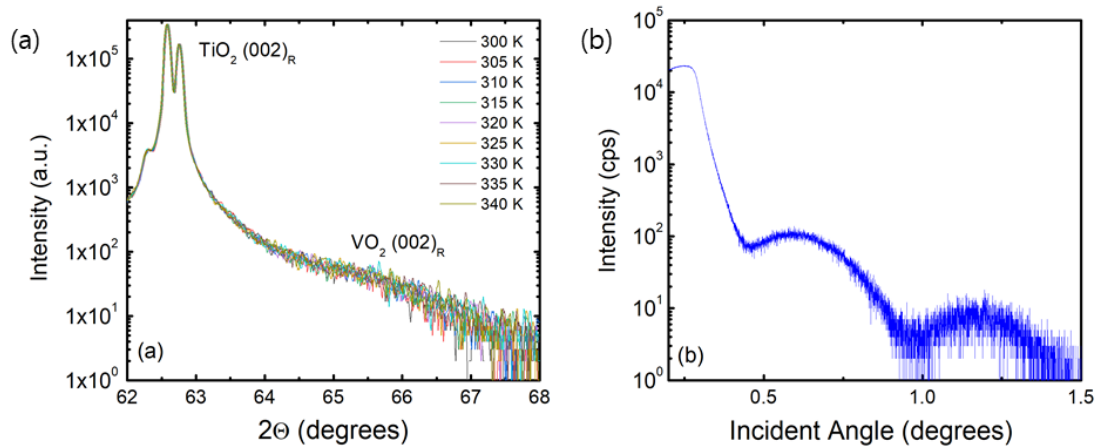


Fig. A2: **(a)** Temperature dependent XRD of the 7.2 nm thick VO_2 film on (001) TiO_2 showing the rutile (R) features. **(b)** Grazing incidence X-ray reflectance at room temperature used to determine VO_2 film thickness of 7.2 nm.

Appendix C: Ultrathin VO₂ film dielectric function

The frequency dependent real and imaginary parts of the dielectric function of the 7.2 nm rutile VO₂ film above and below the insulator-to-metal transition temperature are plotted in figure A3.

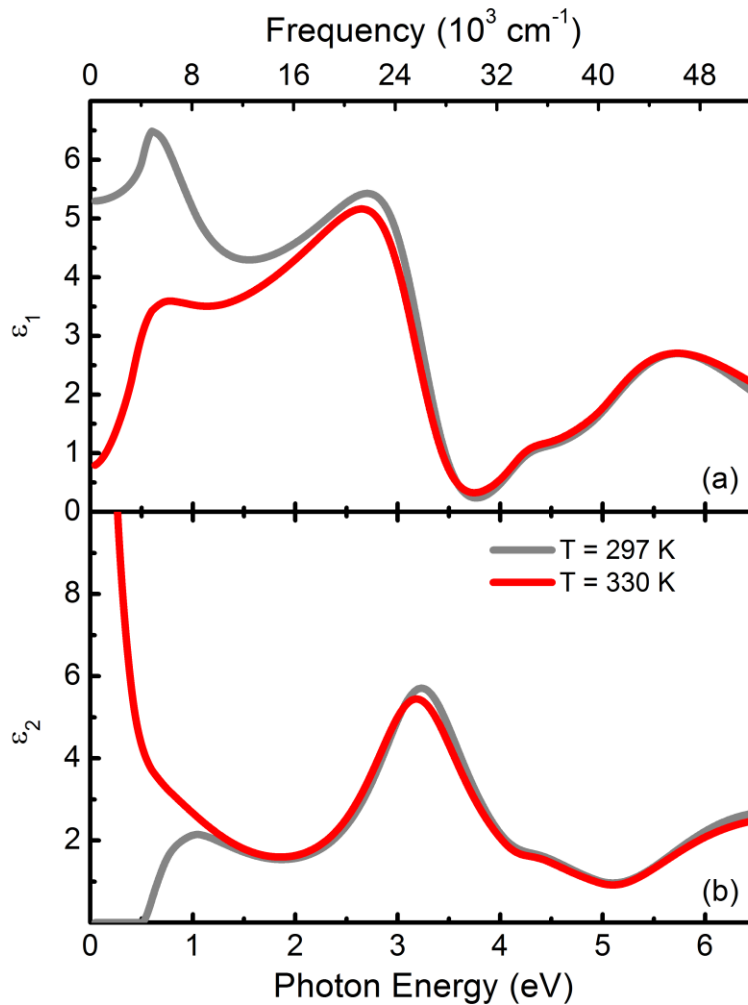


Figure A3: The real **(a)** and imaginary **(b)** parts of the dielectric function for the insulating (grey) and metallic (red) phases of the VO₂ film as a function of photon energy.

Appendix D: Ultrathin VO₂ film metallic layer analysis

This analysis was carried out to better understand the optical properties of the VO₂ film in the metallic state. The question to be answered is if the film transitions fully over the 7.2 nm thickness with metallic optical constants obtained from far-field spectroscopies or if there is inhomogeneity in the direction normal to the film surface whereby there is a certain percentage of the film that transitions to bulk like metallic VO₂ and the rest remains as insulating VO₂. The experimental data available to us is the far-field spectroscopy measurements including ellipsometry, and FTIR reflectance and transmission as well as scattering type near-field microscopy at $\lambda = 10.3 \mu\text{m}$. S-SNIM images obtained below, in the vicinity of, and above the T_c tell us that close to the T_c there is phase coexistence. However, above T_c in the metallic state there is no observable phase coexistence in the plane of the film based on S-SNIM images.

This tells us that if only a certain percentage of the film is transitioning then it must be along the z-axis i.e. normal to the film surface which would likely be due to interface strain. Modeling our film as a layer consisting of the bulk-like metallic VO₂ optical constants [137] and a layer consisting of our film's insulating optical constants, we varied the relative thicknesses of both with the constraint that the total composite thickness must equal 7.2 nm. For both the instance of the bulk metallic layer being at the interface (Figure A4(d) inset) and on the top (Figure A5(d) inset) we observed that the closest fit for all the far-field data was for a thickness of 1.5 nm with bulk-like metallic optical constants. For both cases we get

a close fit with the reflectance and the transmission being virtually identical for the interface metallic layer case and the case of a top metallic layer. Looking at figure A5 where the metallic layer is on the surface, we see a slightly closer fit. However, for both orientations, the model of a fully metallic 7.2 nm film gives the best fit.

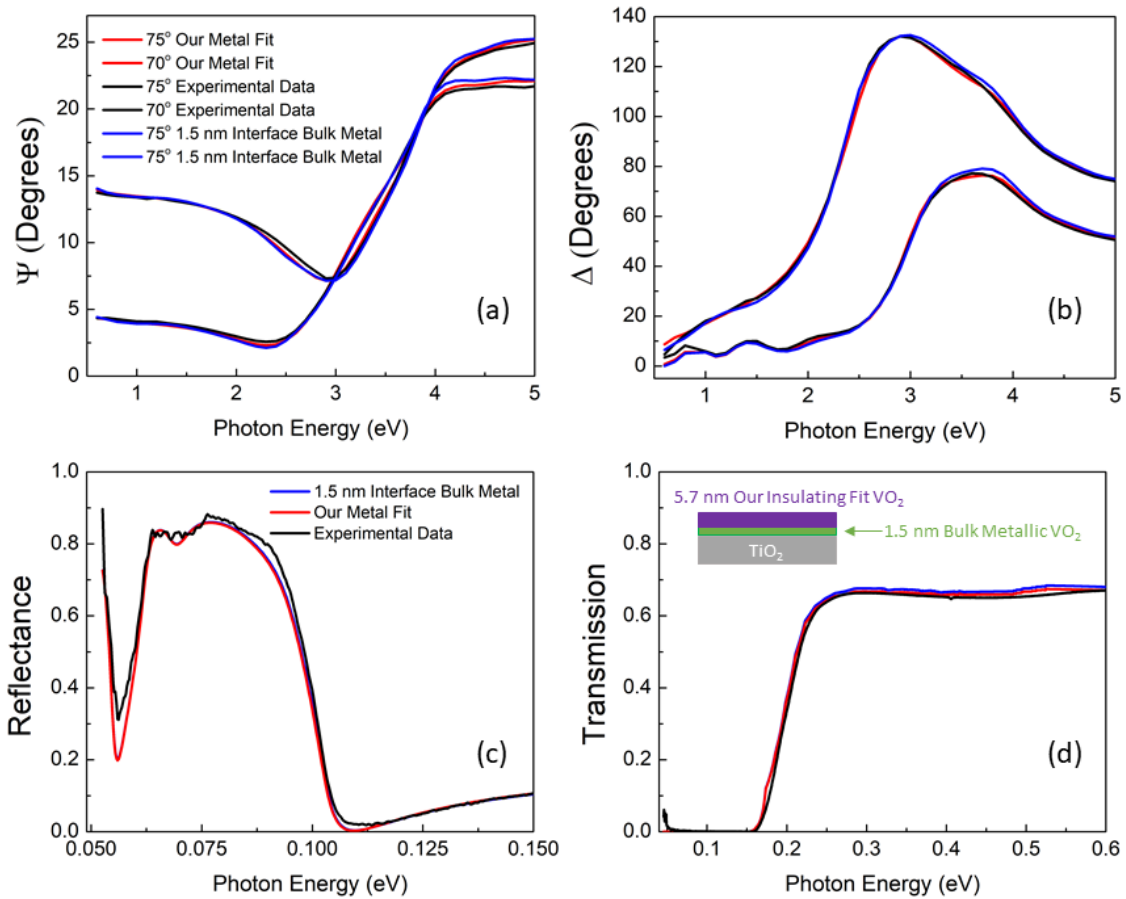


Fig. A4: Ellipsometry measurements of Ψ (a) and Δ (b) along with absolute reflectance (c) and absolute transmission (d) for our metallic fit of the full film compared to a top layer of VO_2 with our insulating optical constants over a interface layer of bulk VO_2 metallic optical constants. The inset shows a schematic of the film for clarity.

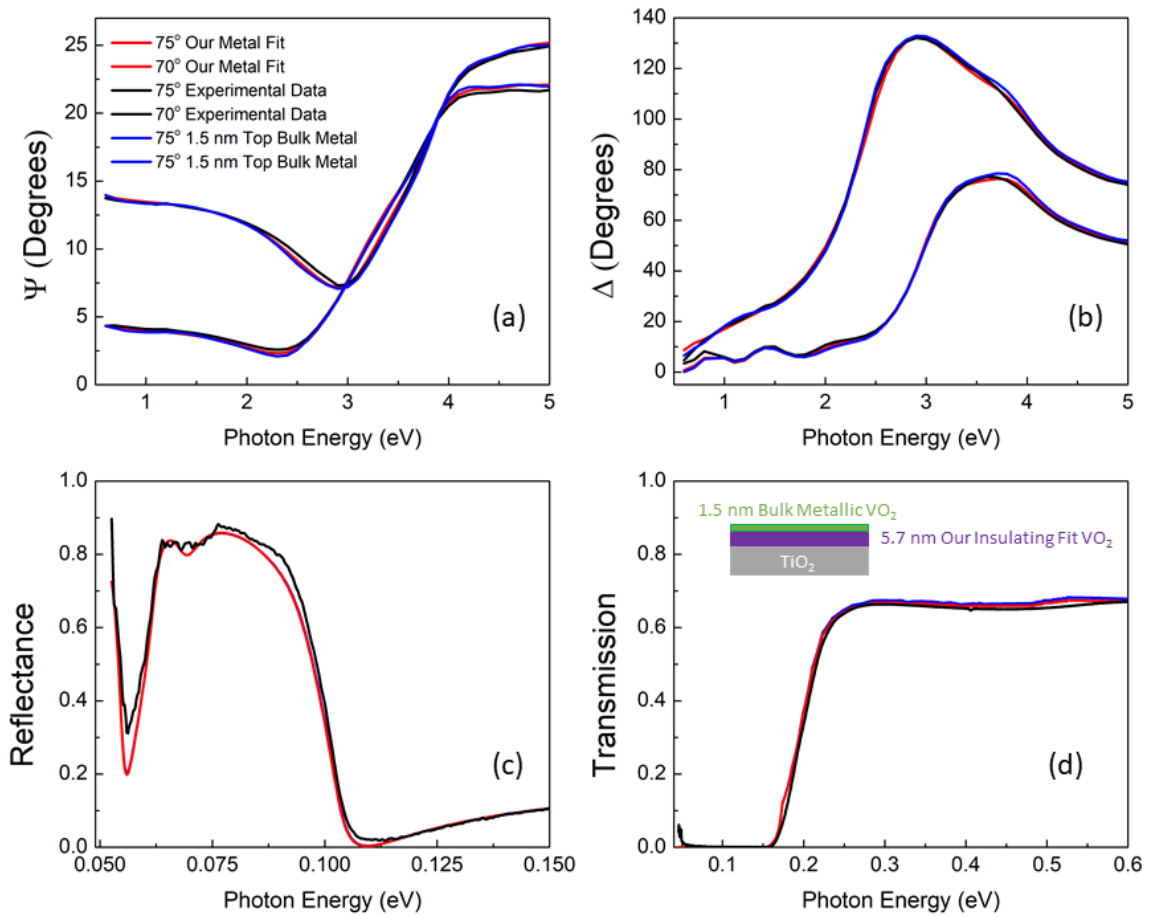


Fig. A5: Ellipsometry measurements of Ψ (a) and Δ (b) along with absolute reflectance (c) and absolute transmission (d) for our metallic fit of the full film compared to a top layer of VO₂ with bulk VO₂ metallic optical constants over a layer of VO₂ with our insulating optical constants. The inset shows a schematic of the film for clarity.

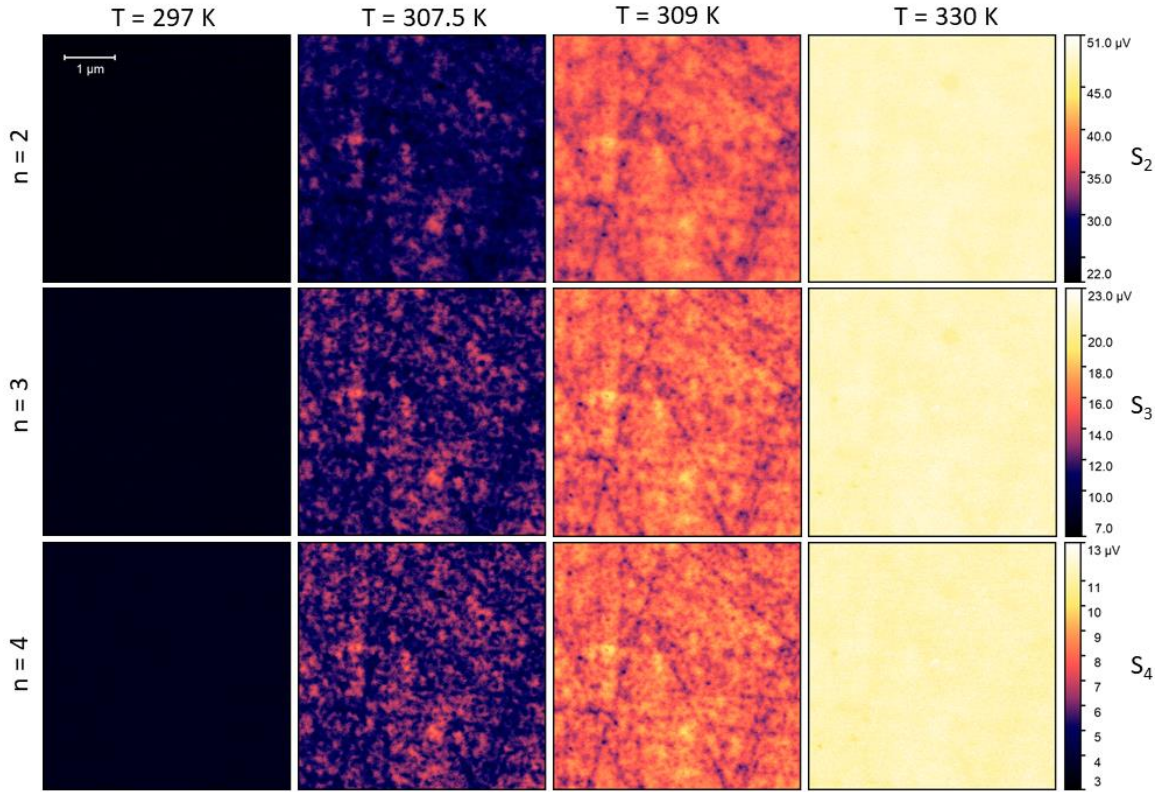


Fig. A6: (Experiment 1) Single line s-SNIM images at $\lambda = 10.3 \mu\text{m}$ above, through and below the T_c of the film at all higher harmonics ($n = 2, 3, 4$). Each image represents the same area of the film with a lateral resolution of 15 nm. The white scale bar to the top left represents 1 μm . The scale bars to the right of the images represent the scattered amplitude measured at the detector with a higher amplitude (light yellow) representing the metallic state and a lower amplitude (navy blue) representing the insulating state. While there is some percolative contrast in the vicinity of the T_c , there is no observable lateral phase coexistence in the metallic state ($T = 330 \text{ K}$) or insulating state ($T = 297 \text{ K}$) where the far-field spectra were taken.

S-SNIM provides a more surface sensitive technique at the longer wavelengths where the metallic Drude feature is located [143,146]. Two experiments were carried out with the first consisting of taking images of the same

area while incrementally increasing the temperature from insulating to fully metallic. Some of this data is shown in figure A6 with the insulating ($T = 297$ K) and metallic ($T = 330$ K) showing clear and homogenous insulating and metallic states. There is some inhomogeneity in the intermediate temperatures but at all harmonics at 330 K where the far-field spectra were taken the film is fully metallic with no phase coexistence along the surface of the film. The second experiment was to take images of the film at insulating and metallic temperatures as well as images of a gold layer in order to remove any experimental temperature induced effects on the AFM and provide a way to compare the data to simulations. This data is shown in figure A7 with the insulating and metallic images showing no lateral (in-plane) phase coexistence. Figure A8 shows how the values of gold and insulating and metallic VO_2 were extracted by fitting the intensity distribution of each image with a gaussian function, $f(x) = y_0 + ae^{-(x-x_0)^2/b^2}$, to give a systematic method to extract the peak value across multiple scans.

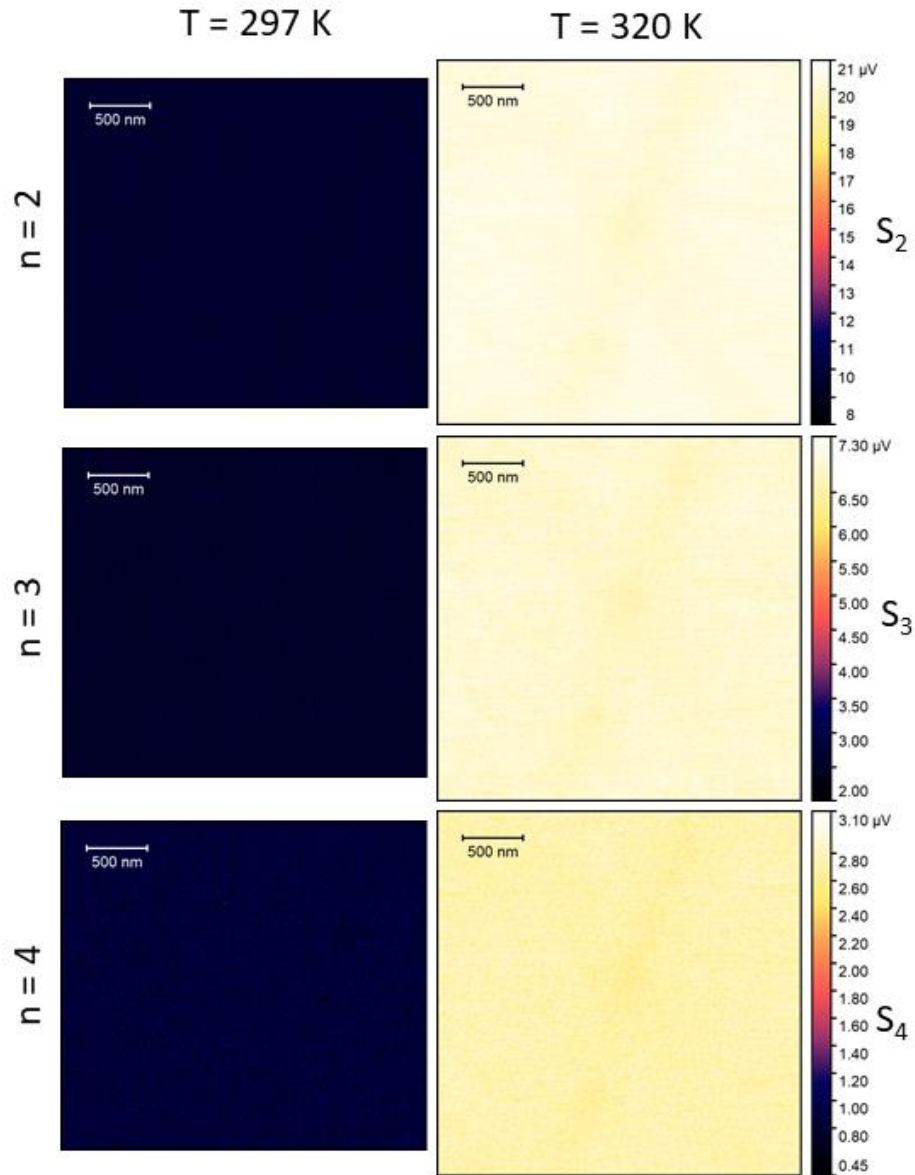


Fig. A7: (Experiment 2) Single line s-SNIM images at $\lambda = 10.3 \mu\text{m}$ above and below the T_c of the film at all higher harmonics ($n = 2, 3, 4$). The scale bars to the right of the images represent the scattered amplitude measured at the detector with a higher amplitude (light yellow) representing the metallic state and a lower amplitude (navy blue) representing the insulating state. There is no observable lateral phase coexistence in the metallic state ($T = 320 \text{ K}$) or insulating state ($T = 297 \text{ K}$).

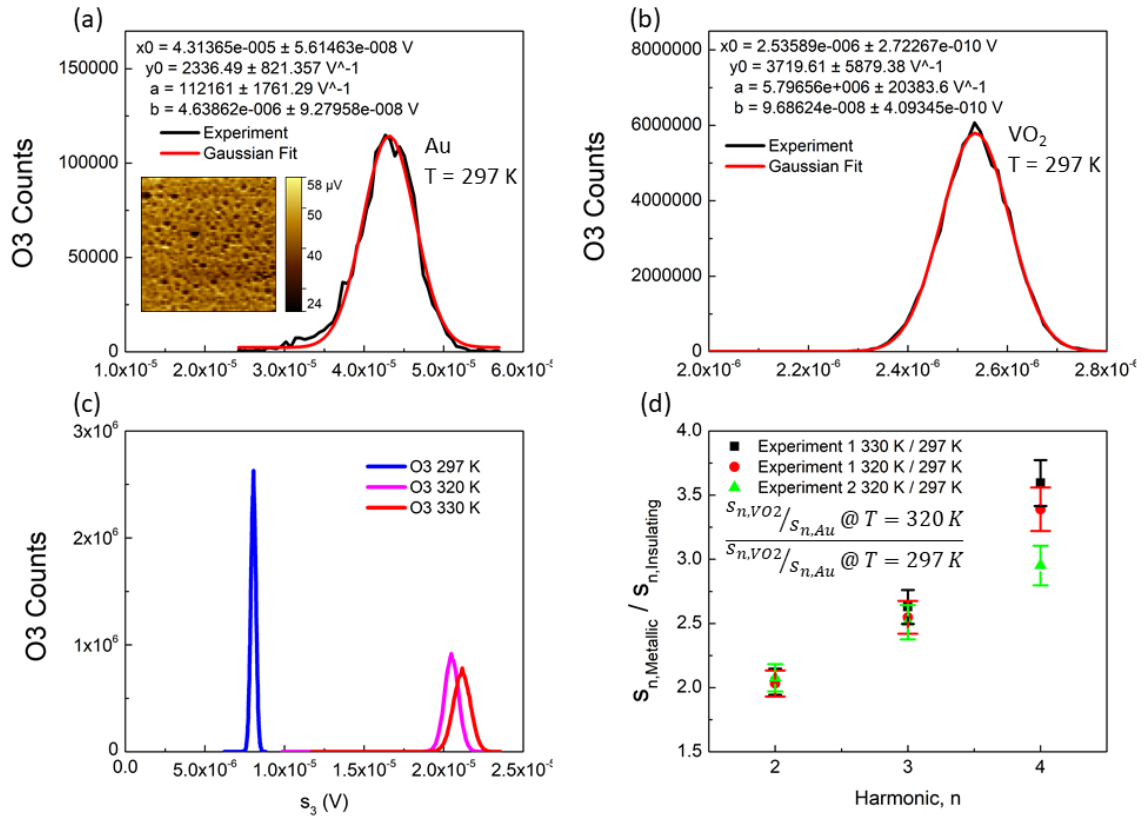


Fig. A8 **(a)** Distribution of near-field scattered amplitude at the third harmonic for a 1 x 1 μ m image taken on gold (inset) with the gaussian fit to determine the peak value. Data is from experiment 2. **(b)** Same analysis but for an image over insulating VO_2 at $T = 297$ K also taken from experiment 2. **(c)** Near-field scattered amplitude for VO_2 from Experiment 1 showing the relative increase for 297 K, 320 K and 330 K showing that there is a small increase from 320 K to 330 K. **(d)** Plot of the relative increase from insulating to metallic for experiment 1 and experiment 2 where the values for the amplitudes were determined using the method shown in **(a)** and **(b)**. For experiment 2 each measured value is normalized to gold at the same temperature which is seen in the equation under the legend. Experiment 1 has no gold normalization. Looking at experiment 1 compared to experiment 2 we see that the fourth harmonic is lower for the gold normalized data *even at the same temperature of 320 K*. This indicates that the gold normalization is necessary to get the most accurate comparison to the simulation.

The metallic scattered amplitude increases over the insulating amplitude with the increase getting larger as the harmonic is increased. We numerically

simulate the near-field experiment with the film for the three cases of either our full metallic film with our fitted optical constants or the composite 1.5 nm layer of bulk metallic optical constants and a 5.7 nm layer of our insulating optical constants. At 10.3 μm we are away from any resonant near-field effects from phonons or plasmons so a simple model where the tip can be modeled as a sphere can be employed [8,34]. We set the sphere radius to be 20 nm which matches the experimental tip radius of curvature. We simulate the sphere tapping at the experimental AFM tapping amplitude and oscillation frequency (Ω) and demodulate the scattered signal the same way the s-SNIM demodulates to get the higher harmonics of the near-field signal ($n\Omega$, where $n = 2, 3, 4$). First, we simulated a known s-SNIM experiment of 2 nm of SiO₂ on Si which gave us correct results at our wavelength. We then simulated the three possible cases for our film.

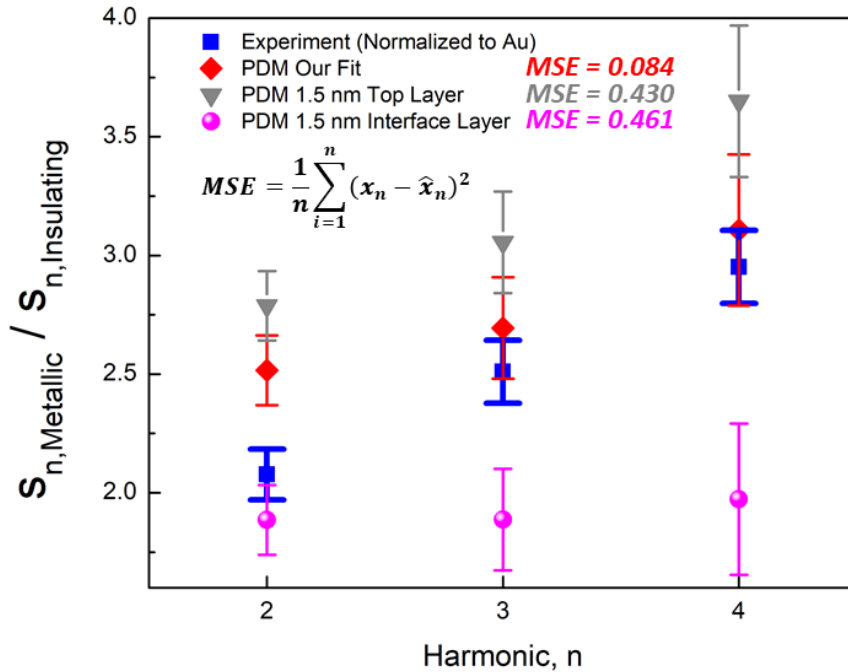


Fig. A9. Experiment 2 compared to the simulated point dipole model for a full metallic layer with our experimentally determined optical constants, 1.5 nm top layer of bulk-like metallic VO2 optical constants on 5.7 nm layer of our measured insulating optical constants and a 1.5 nm bulk-like metallic interface layer under 5.7 nm layer of our insulating optical constants. Looking at the Mean squared error with (x = experimental value, \hat{x} = predicted) we see that the closest match is our metallic optical constants over the full 7.2 nm film thickness.

Figure A9 shows the experimental and simulated relative amplitude increase (metal / insulating). This relative amplitude increase acts as a normalized value that can be compared across different experiments and simulations. We used experiment 2 due to its gold normalization allowing better accuracy. When all harmonics are looked at collectively, the best agreement with our data is our

metallic optical constants for the full 7.2 nm film. The MSE is lowest when it is calculated using our experimental data compared to our metallic fit of the full 7.2 nm film. The error is larger for the 1.5 nm bulk metallic surface layer and much larger for the 1.5 nm bulk metallic interface layer. From this analysis our experimental data indicates that the film is not partially transitioning to a certain percentage of bulk metallic VO₂. The near-field images indicate no phase segregation in the xy- plane while the far-field data, near-field data and near-field simulations indicate that there is no phase segregation in the out of plane direction.

Bibliography

1. J. H. De Boer and E. J. W. Verwey, "Semi-conductors with partially and with completely filled 3d-lattice bands," *Proc. Phys. Soc.* **49**, 59–71 (1937).
2. N. F. Mott and R. Peierls, "Discussion of the paper by de Boer and Verwey," *Proc. Phys. Soc.* **49**, 72–73 (1937).
3. S. V. Dordevic and D. N. Basov, "Electrodynamics of correlated electron matter," *Ann. der Phys.* **15**, 545–570 (2006).
4. M. Marezio, D. McWhan, J. Remeika, and P. Dernier, "Structural Aspects of the Metal-Insulator Transitions in Cr-Doped VO₂," *Phys. Rev. B* **5**, 2538–2541 (1972).
5. F. J. Morin, "Oxides which show a metal-to-insulator transition at the neel temperature," *Phys. Rev. Lett.* **3**, 34–36 (1959).
6. M. M. Qazilbash, M. Brehm, B.-G. B. G. Chae, P.-C. C. Ho, G. O. Andreev, B. J. B.-J. Kim, S. J. Yun, A. V. Balatsky, M. B. Maple, F. Keilmann, H.-T. H. T. Kim, and D. N. Basov, "Mott Transition in VO₂ Revealed by Infrared Spectroscopy and Nano-Imaging," *Science* (80-.). **318**, 1750–1753 (2007).
7. R. Hillenbrand and F. Keilmann, "Complex optical constants on a subwavelength scale," *Phys. Rev. Lett.* **85**, 3029–3032 (2000).
8. F. Keilmann and R. Hillenbrand, "Near-field microscopy by elastic light scattering from a tip.," *Philos. Trans. A. Math. Phys. Eng. Sci.* **362**, 787–805 (2004).
9. M. Liu, A. J. Sternbach, and D. N. Basov, "Nanoscale electrodynamics of strongly correlated quantum materials," *Reports Prog. Phys.* **80**, 014501 (2017).

10. D. L. Mills and E. Burstein, "Polaritons: The electromagnetic modes of media," *Reports Prog. Phys.* **37**, 817–926 (1974).
11. A. Huber, N. Ocelic, D. Kazantsev, and R. Hillenbrand, "Near-field imaging of mid-infrared surface phonon polariton propagation," *Appl. Phys. Lett.* **87**, 2003–2006 (2005).
12. S. Bensmann, F. Gaußmann, M. Lewin, J. Wüppen, S. Nyga, C. Janzen, B. Jungbluth, and T. Taubner, "Near-field imaging and spectroscopy of locally strained GaN using an IR broadband laser.," *Opt. Express* **22**, 22369–22381 (2014).
13. S. Amarie and F. Keilmann, "Broadband-infrared assessment of phonon resonance in scattering-type near-field microscopy," *Phys. Rev. B* **83**, 1–9 (2011).
14. H. A. Bechtel, E. A. Muller, R. L. Olmon, M. C. Martin, and M. B. Raschke, "Ultrabroadband infrared nanospectroscopic imaging.," *Proc. Natl. Acad. Sci. U. S. A.* **111**, 7191–6 (2014).
15. O. Khatib, H. A. Bechtel, M. C. Martin, M. B. Raschke, and G. L. Carr, "Far Infrared Synchrotron Near-Field Nanoimaging and Nanospectroscopy," *ACS Photonics* **5**, 2773–2779 (2018).
16. K. Ohtani, B. Meng, M. Franckié, L. Bosco, C. Ndebeka-Bandou, M. Beck, and J. Faist, "An electrically pumped phonon-polariton laser," *Sci. Adv.* **5**, (2019).
17. J. D. Caldwell, L. Lindsay, V. Giannini, I. Vurgaftman, T. L. Reinecke, S. A. Maier, and O. J. Glembocki, "Low-loss, infrared and terahertz nanophotonics using surface phonon polaritons," *Nanophotonics* **4**, 44–68 (2015).
18. T. G. Folland, L. Nordin, D. Wasserman, and J. D. Caldwell, "Probing polaritons in the mid- to far-infrared," *J. Appl. Phys.* **125**, (2019).

19. H. Fujiwara, *Spectroscopic Ellipsometry Principles and Applications*, 1st ed. (John Wiley & Sons, 2007).
20. "Ellipsometry Measurements," <https://www.jawoollam.com/resources/ellipsometry-Tutorial/ellipsometry-Measurements>.
21. F. L. Pedrotti, L. M. Pedrotti, and L. S. Pedrotti, *Introduction to Optics*, 3rd ed. (Cambridge University Press, n.d.).
22. E. Cartlidge, "Tapping into light's hidden information to push fundamental diffraction limit," <https://physicsworld.com/a/tapping-into-lights-hidden-information-to-push-fundamental-diffraction-limit/>.
23. E. Hecht, *Optics*, 4th ed. (Addison-Wesley, 2001).
24. M. Born and E. Wolf, *Principles of Optics*, 7th ed. (Cambridge University Press, 1999).
25. L. Novotny and B. Hecht, *Principles of Nano-Optics*, 2nd ed. (1012).
26. J. D. Jackson, *Classical Electrodynamics Third Edition*, 3rd ed. (Wiley, 1998).
27. S. Amarie, T. Ganz, and F. Keilmann, "Mid-infrared near-field spectroscopy.," *Opt. Express* **17**, 21794–801 (2009).
28. G. Dominguez, A. S. Mcleod, Z. Gainsforth, P. Kelly, H. A. Bechtel, F. Keilmann, A. Westphal, M. Thiemens, and D. N. Basov, "Nanoscale infrared spectroscopy as a non-destructive probe of extraterrestrial samples," *Nat. Commun.* **5**, 5445 (2014).
29. N. Ocelic, A. Huber, and R. Hillenbrand, "Pseudoheterodyne detection for background-free near-field spectroscopy," *Appl. Phys. Lett.* **89**, 3–6 (2006).
30. D. G. Mead and L. Genzel, "Interferometry in the Asymmetric Mode," *Infrared Phys.* **18**, 555–564 (1978).

31. F. Huth, "Nano-FTIR - Nanoscale Infrared Near-Field Spectroscopy," Universidad Del Pais Vasco (2015).
32. N. Ocelic, "Quantitative Near-field Phonon-polariton Spectroscopy," TU Munich (2007).
33. R. Hillenbrand, B. Knoll, and F. Keilmann, "Pure optical contrast in scattering-type scanning near-field microscopy," *J. Microsc.* **202**, 77–83 (2001).
34. R. Hillenbrand, T. Taubner, and F. Keilmann, "Phonon-enhanced light – matter interaction at the nanometre scale," *Nature* **748**, 1542–1544 (2002).
35. E. E. Bell, "Measurement of the far infrared optical properties of solids with a michelson interferometer used in the asymmetric mode: Part 1, mathematical formulation," *Infrared Phys.* **6**, 57–74 (1966).
36. M. Brehm, A. Schliesser, F. Cajko, I. Tsukerman, and F. Keilmann, "Antenna-mediated back-scattering efficiency in infrared near-field microscopy.," *Opt. Express* **16**, 11203–11215 (2008).
37. L. M. Zhang, G. O. Andreev, Z. Fei, A. S. McLeod, G. Dominguez, M. Thiemens, A. H. Castro-Neto, D. N. Basov, and M. M. Fogler, "Near-field spectroscopy of silicon dioxide thin films," *Phys. Rev. B* **85**, 1–8 (2012).
38. Z. Fei, G. O. Andreev, W. Bao, L. M. Zhang, A. S. McLeod, C. Wang, M. K. Stewart, Z. Zhao, G. Dominguez, M. Thiemens, M. M. Fogler, M. J. Tauber, A. H. Castro-Neto, C. N. Lau, F. Keilmann, and D. N. Basov, "Infrared nanoscopy of dirac plasmons at the graphene-SiO₂ interface," *Nano Lett.* **11**, 4701–4705 (2011).
39. I. M. Craig, M. S. Taubman, A. S. Lea, M. C. Phillips, E. E. Josberger, and M. B. Raschke, "Infrared near-field spectroscopy of trace explosives using an external cavity quantum cascade laser," *Opt. Express* (2013).
40. B. T. O’Callahan, W. E. Lewis, S. Möbius, J. C. Stanley, E. A. Muller, and

- M. B. Raschke, "Broadband infrared vibrational nano-spectroscopy using thermal blackbody radiation," *Opt. Express* **23**, 32063 (2015).
41. F. Huth, M. Schnell, J. Wittborn, N. Ocelic, and R. Hillenbrand, "Infrared-spectroscopic nanoimaging with a thermal source," *Nat. Mater.* **10**, 352–356 (2011).
 42. P. Hermann, A. Hoehl, P. Patoka, F. Huth, E. Ruehl, and G. Ulm, "Near-field imaging and nano-Fourier-transform infrared spectroscopy using broadband synchrotron radiation.," *Opt. Express* **21**, 2913–9 (2013).
 43. P. Hermann, A. Hoehl, G. Ulrich, C. Fleischmann, A. Hermelink, B. Kästner, P. Patoka, A. Hornemann, B. Beckhoff, E. Rühl, and G. Ulm, "Characterization of semiconductor materials using synchrotron radiation-based near-field infrared microscopy and nano-FTIR spectroscopy.," *Opt. Express* **22**, 17948–58 (2014).
 44. J. M. Bridges and a L. Migdall, "Characterization of argon arc source in the infrared," *Metrologia* **32**, 625–628 (1995).
 45. F. Huth, A. Chuvilin, M. Schnell, I. Amenabar, R. Krutokhvostov, S. Lopatin, and R. Hillenbrand, "Resonant antenna probes for tip-enhanced infrared near-field microscopy," *Nano Lett.* **13**, 1065–1072 (2013).
 46. A. L. McIntosh, B. A. Wofford, R. R. Lucchese, and J. W. Bevan, "High resolution Fourier transform infrared spectroscopy using a high temperature argon arc source," *Infrared Phys. Technol.* **42**, 509–514 (2001).
 47. M. Fath, S. Freismen, A. A. Menovsky, Y. Tomioka, J. Aarts, and J. A. Mydosh, "Spatially Inhomogeneous Metal-Insulator Transition in Doped Manganites," *Science* (80-.). **285**, 1540–1542 (1999).
 48. T. Becker, C. Streng, Y. Luo, V. Moshnyaga, B. Damaschke, N. Shannon, and K. Samwer, "Intrinsic inhomogeneities in manganite thin films

- investigated with scanning tunneling spectroscopy," *Phys. Rev. Lett.* **89**, 237203 (2002).
49. A. S. McLeod, E. van Heumen, J. G. Ramirez, S. Wang, T. Saerbeck, S. Guenon, M. Goldflam, L. Anderegg, P. Kelly, A. Mueller, M. K. Liu, I. K. Schuller, and D. N. Basov, "Nanotextured phase coexistence in the correlated insulator V₂O₃," *Nat. Phys.* **1**, 1–8 (2016).
 50. Y. Abate, D. Seidlitz, A. Fali, S. Gamage, V. Babicheva, V. S. Yakovlev, M. I. Stockman, R. Collazo, D. Alden, and N. Dietz, "Nanoscopy of phase separation in In_xGa_{1-x}N alloys," *ACS Appl. Mater. Interfaces* **8**, 23160–23166 (2016).
 51. C. Westermeier, A. Cernescu, S. Amarie, C. Liewald, F. Keilmann, and B. Nickel, "Sub-micron phase coexistence in small-molecule organic thin films revealed by infrared nano-imaging," *Nat. Commun.* **5**, 1–6 (2014).
 52. J. Stiegler, Y. Abate, A. Cvitkovic, Y. Romanyuk, A. Huber, S. Leone, and R. Hillenbrand, "Nanoscale IR Absorption Spectroscopy of Individual NPs Enabled by Scattering-Type Near-Field Microscopy," *ACS Nano* **5**, 6494–6499 (2011).
 53. W. G. Spitzer, R. C. Miller, D. A. Kleinman, and L. E. Howarth, "Far Infrared Dielectric Dispersion in BaTiO₃, SrTiO₃, and TiO₂," *Phys. Rev.* **126**, 1710–1721 (1962).
 54. M. K. Gunde, "Vibrational modes in amorphous silicon dioxide," *Phys. B Condens. Matter* **292**, 286–295 (2000).
 55. A. Cvitkovic, N. Ocelic, and R. Hillenbrand, "Analytical model for quantitative prediction of material contrasts in scattering-type near-field optical microscopy.," *Opt. Express* **15**, 8550–65 (2007).
 56. M. F. Kimmitt and G. B. F. Niblett, "Infra-red Emission from the Theta Pinch," *Proc. Phys. Soc. LONDON* **82**, 938–946 (1963).

57. W. Elenbaas, *Light Sources (Philips Technical Library)*, 1st ed. (Crane, Russak, 1973).
58. D. J. Lahneman, T. J. Huffman, P. Xu, S. L. Wang, T. Grogan, and M. M. Qazilbash, "Broadband near-field infrared spectroscopy with a high temperature plasma light source," *Opt. Express* **25**, 20421–20430 (2017).
59. P. Mcardle, D. J. Lahneman, A. Biswas, F. Keilmann, and M. M. Qazilbash, "Near-field infrared nanospectroscopy of surface phonon-polariton resonances," *Phys. Rev. Res.* **2**, 23272 (2020).
60. S. Zollner, A. A. Demkov, R. Liu, P. L. Fejes, R. B. Gregory, P. Alluri, J. A. Curless, Z. Yu, J. Ramdani, R. Droopad, T. E. Tiwald, J. N. Hilfiker, and J. A. Woollam, "Optical properties of bulk and thin-film SrTiO₃ on Si and Pt," *J. Vac. Sci. Technol. B Microelectron. Nanom. Struct.* **18**, 2242 (2000).
61. M. M. Qazilbash and D. J. Lahneman, "Infrared light generating system," U.S. patent US 9 , 934 , 927 B1 (2018).
62. P. R. Griffiths and J. A. de Haseth, *Fourier Transform Infrared Spectrometry*, 2nd ed. (Wiley Interscience, 2007).
63. C. H. Henry and J. J. Hopfield, "Raman scattering by Polaritons," *Phys. Rev. Lett.* **15**, 964–966 (1965).
64. A. V. Zayats, I. I. Smolyaninov, and A. A. Maradudin, "Nano-optics of surface plasmon polaritons," *Phys. Rep.* **408**, 131–314 (2005).
65. H. Deng, H. Haug, and Y. Yamamoto, "Exciton-polariton Bose-Einstein condensation," *Rev. Mod. Phys.* **82**, 1489–1537 (2010).
66. J. Kasprzak, M. Richard, S. Kundermann, A. Baas, P. Jeambrun, J. M. J. Keeling, F. M. Marchetti, M. H. Szymńska, R. André, J. L. Staehli, V. Savona, P. B. Littlewood, B. Deveaud, and L. S. Dang, "Bose-Einstein condensation of exciton polaritons," *Nature* **443**, 409–414 (2006).

67. A. Amo, J. Lefrère, S. Pigeon, C. Adrados, C. Ciuti, I. Carusotto, R. Houdré, E. Giacobino, and A. Bramati, "Superfluidity of polaritons in semiconductor microcavities," *Nat. Phys.* **5**, 805–810 (2009).
68. K. G. Lagoudakis, M. Wouters, M. Richard, A. Baas, I. Carusotto, R. André, L. S. Dang, and B. Deveaud-Plédran, "Quantized vortices in an exciton-polariton condensate," *Nat. Phys.* **4**, 706–710 (2008).
69. S. Kéna-Cohen and S. R. Forrest, "Room-temperature polariton lasing in an organic single-crystal microcavity," *Nat. Photonics* **4**, 371–375 (2010).
70. S. Christopoulos, G. B. H. Von Högersthal, A. J. D. Grundy, P. G. Lagoudakis, A. V. Kavokin, J. J. Baumberg, G. Christmann, R. Butté, E. Feltin, J. F. Carlin, and N. Grandjean, "Room-temperature polariton lasing in semiconductor microcavities," *Phys. Rev. Lett.* **98**, 1–4 (2007).
71. D. Ballarini, M. De Giorgi, E. Cancellieri, R. Houdré, E. Giacobino, R. Cingolani, A. Bramati, G. Gigli, and D. Sanvitto, "All-optical polariton transistor," *Nat. Commun.* **4**, (2013).
72. X. Zhong, T. Chervy, S. Wang, J. George, A. Thomas, J. A. Hutchison, E. Devaux, C. Genet, and T. W. Ebbesen, "Non-radiative energy transfer mediated by hybrid light-matter states," *Angew. Chemie - Int. Ed.* **55**, 6202–6206 (2016).
73. J. J. Greffet, R. Carminati, K. Joulain, J. P. Mulet, S. Mainguy, and Y. Chen, "Coherent emission of light by thermal sources," *Nature* **416**, 61–64 (2002).
74. N. Ocelic and R. Hillenbrand, "Subwavelength-scale tailoring of surface phonon polaritons by focused ion-beam implantation.," *Nat. Mater.* **3**, 606–609 (2004).
75. J. D. Caldwell, O. J. Glembocki, Y. Francescato, N. Sharac, V. Giannini, F. J. Bezares, J. P. Long, J. C. Owrutsky, I. Vurgaftman, J. G. Tischler, V. D.

- Wheeler, N. D. Bassim, L. M. Shirey, R. Kasica, and S. A. Maier, "Low-loss, extreme subdiffraction photon confinement via silicon carbide localized surface phonon polariton resonators," *Nano Lett.* **13**, 3690–3697 (2013).
76. G. Shvets, "Photonic approach to making a material with a negative index of refraction," *Phys. Rev. B - Condens. Matter Mater. Phys.* **67**, 035109 (2003).
77. H. S. Kim, N. Y. Ha, J. Y. Park, S. Lee, D. S. Kim, and Y. H. Ahn, "Phonon-Polaritons in Lead Halide Perovskite Film Hybridized with THz Metamaterials," *Nano Lett.* **20**, 6690–6696 (2020).
78. T. Tanabe, K. Suto, J. Nishizawa, K. Saito, and T. Kimura, "Frequency-tunable terahertz wave generation via excitation of phonon-polaritons in GaP and beam properties," *J. Phys. D Applied Phys.* **36**, 953–957 (2003).
79. M. Lewin, C. Baeumer, F. Gunkel, A. Schwedt, F. Gaussmann, J. Wueppen, P. Meuffels, B. Jungbluth, J. Mayer, R. Dittmann, R. Waser, and T. Taubner, "Nanospectroscopy of Infrared Phonon Resonance Enables Local Quantification of Electronic Properties in Doped SrTiO₃ Ceramics," *Adv. Funct. Mater.* **28**, 1802834 (2018).
80. L. Wehmeier, D. Lang, Y. Liu, X. Zhang, S. Winnerl, L. M. Eng, and S. C. Kehr, "Polarization-dependent near-field phonon nanoscopy of oxides: SrTiO₃, LiNbO₃, and PbZr_{0.2}Ti_{0.8}O₃," *Phys. Rev. B* **100**, 35444 (2019).
81. A. A. Sirenko, A. M. Clark, J. Hao, W. Si, and X. X. Xi, "Soft-mode hardening in SrTiO₃ thin films," *Nature* **404**, 373–376 (2000).
82. J. H. Haeni, P. Irvin, W. Chang, R. Uecker, P. Reiche, Y. L. Li, S. Choudhury, W. Tian, M. E. Hawley, B. Craigo, A. K. Tagantsev, X. Q. Pan, S. K. Streiffer, L. Q. Chen, S. W. Kirchoefer, J. Levy, and D. G. Schlom, "Room-temperature ferroelectricity in strained SrTiO₃," *Nature* **430**, 758–761 (2004).

83. A. Sendil Kumar, P. Suresh, M. Mahesh Kumar, H. Srikanth, M. L. Post, K. Sahner, R. Moos, and S. Srinath, "Magnetic and ferroelectric properties of Fe doped SrTiO_{3-δ} films," *J. Phys. Conf. Ser.* **200**, 2–6 (2010).
84. S. Taibl, G. Fafilek, and J. Fleig, "Impedance spectra of Fe-doped SrTiO₃ thin films upon bias voltage: Inductive loops as a trace of ion motion," *Nanoscale* **8**, 13954–13966 (2016).
85. O. N. Tufte and P. W. Chapman, "Electron mobility in semiconducting strontium titanate," *Phys. Rev.* **155**, 796–802 (1967).
86. J. L. M. Van Mechelen, D. Van Der Marel, C. Grimaldi, A. B. Kuzmenko, N. P. Armitage, N. Reyren, H. Hagemann, and I. I. Mazin, "Electron-phonon interaction and charge carrier mass enhancement in SrTiO₃," *Phys. Rev. Lett.* **100**, 7–10 (2008).
87. W. Baer, "Free-carrier Absorption in Reduced SrTiO₃," *Phys. Rev.* **144**, 2–6 (1966).
88. I. H. Kwak, S. S. Varnoosfaderani, C. S. Barquist, A. Paykar, A. Shakya, Y. Lee, A. F. Hebard, and A. Biswas, "Optimization of atomically smooth and metallic surface of SrTiO₃," *J. Appl. Phys.* **121**, (2017).
89. P. P. Balakrishnan, M. J. Veit, U. S. Alaan, M. T. Gray, and Y. Suzuki, "Metallicity in SrTiO₃ substrates induced by pulsed laser deposition," *APL Mater.* **7**, (2019).
90. X. Lin, C. W. Rischau, L. Buchauer, A. Jaoui, B. Fauqué, and K. Behnia, "Metallicity without quasi-particles in room-temperature strontium titanate," *npj Quantum Mater.* **2**, 1–8 (2017).
91. A. Ohtomo and H. Y. Hwang, "A high-mobility electron gas at the LaAlO₃ / SrTiO₃ heterointerface," *Nature* **427**, 423–427 (2004).
92. A. F. Santander-Syro, O. Copie, T. Kondo, F. Fortuna, S. Pailhès, R. Weht, X. G. Qiu, F. Bertran, A. Nicolaou, A. Taleb-Ibrahimi, P. Le Fèvre, G.

- Herranz, M. Bibes, N. Reyren, Y. Apertet, P. Lecoeur, A. Barthélémy, and M. J. Rozenberg, "Two-dimensional electron gas with universal subbands at the surface of SrTiO₃," *Nature* **469**, 189–194 (2011).
93. J. F. Schooley, W. R. Hosler, and M. L. Cohen, "Superconductivity in Semiconducting SrTiO₃," *Phys. Rev. Lett.* **12**, 474–475 (1964).
94. G. Binnig, A. Baratoff, H. E. Hoenig, and J. G. Bednorz, "Two-band superconductivity in Nb-Doped SrTiO₃," *Phys. Rev. Lett.* **45**, 1352–1355 (1980).
95. D. P. Norton, "Synthesis and properties of epitaxial electronic oxide thin-film materials," *Mater. Sci. Eng. R Reports* **43**, 139–247 (2004).
96. N. Kalfagiannis, J. L. Stoner, J. Hillier, I. Vangelidis, and E. Lidorikis, "Mid-to far-infrared sensing: SrTiO₃, a novel optical material," *J. Mater. Chem. C* **7**, 7851–7857 (2019).
97. Y. Zhong, S. D. Malagari, T. Hamilton, and D. Wasserman, "Review of mid-infrared plasmonic materials," *J. Nanophotonics* **9**, 093791 (2015).
98. F. Huth, A. Govyadinov, S. Amarie, W. Nuansing, F. Keilmann, and R. Hillenbrand, "Nano-FTIR absorption spectroscopy of molecular fingerprints at 20 nm spatial resolution," *Nano Lett.* **12**, 3973–3978 (2012).
99. X. Lu, O. Khatib, X. Du, J. Duan, W. Wei, X. Liu, H. A. Bechtel, F. D'Apuzzo, M. Yan, A. Buyanin, Q. Fu, J. Chen, M. Salmeron, J. Zeng, M. B. Raschke, P. Jiang, and X. Bao, "Nanoimaging of Electronic Heterogeneity in Bi₂Se₃ and Sb₂Te₃ Nanocrystals," *Adv. Electron. Mater.* **1700377**, 1700377 (2017).
100. M. B. Raschke and C. Lienau, "Apertureless near-field optical microscopy: Tip-sample coupling in elastic light scattering," *Appl. Phys. Lett.* **83**, 5089–5091 (2003).
101. J. M. Atkin, S. Berweger, A. C. Jones, and M. B. Raschke, "Nano-optical

imaging and spectroscopy of order, phases, and domains in complex solids," *Adv. Phys.* **61**, 745–842 (2012).

102. J. Renger, S. Grafström, L. M. Eng, and R. Hillenbrand, "Resonant light scattering by near-field-induced phonon polaritons," *Phys. Rev. B - Condens. Matter Mater. Phys.* **71**, 1–7 (2005).
103. A. Huber, N. Ocelic, T. Taubner, and R. Hillenbrand, "Nanoscale resolved infrared probing of crystal structure and of plasmon-phonon coupling," *Nano Lett.* **6**, 774–778 (2006).
104. V. E. Babicheva, S. Gamage, L. Zhen, S. B. Cronin, V. S. Yakovlev, and Y. Abate, "Near-Field Surface Waves in Few-Layer MoS₂," *ACS Photonics* **5**, 2106–2112 (2018).
105. S. Dai, Q. Ma, Y. Yang, J. Rosenfeld, M. D. Goldflam, A. McLeod, Z. Sun, T. I. Andersen, Z. Fei, M. Liu, Y. Shao, K. Watanabe, T. Taniguchi, M. Thiemens, F. Keilmann, P. Jarillo-Herrero, M. M. Fogler, and D. N. Basov, "Efficiency of Launching Highly Confined Polaritons by Infrared Light Incident on a Hyperbolic Material," *Nano Lett.* **17**, 5285–5290 (2017).
106. S. Dai, Q. Ma, M. K. Liu, T. Andersen, Z. Fei, M. D. Goldflam, M. Wagner, K. Watanabe, T. Taniguchi, M. Thiemens, F. Keilmann, G. C. A. M. Janssen, S.-E. Zhu, P. Jarillo-Herrero, M. M. Fogler, and D. N. Basov, "Graphene on hexagonal boron nitride as a tunable hyperbolic metamaterial.," *Nat. Nanotechnol.* **10**, 682–6 (2015).
107. Z. Shi, H. A. Bechtel, S. Berweger, Y. Sun, B. Zeng, C. Jin, H. Chang, M. C. Martin, M. B. Raschke, and F. Wang, "Amplitude- and Phase-Resolved Nanospectral Imaging of Phonon Polaritons in Hexagonal Boron Nitride," *ACS Photonics* **2**, 790–796 (2015).
108. S. Dai, Z. Fei, Q. Ma, A. S. Rodin, M. Wagner, A. S. McLeod, M. K. Liu, W. Gannett, W. Regan, K. Watanabe, T. Taniguchi, M. Thiemens, G. Dominguez, A. H. Castro Neto, A. Zettl, F. Keilmann, P. Jarillo-Herrero, M.

- M. Fogler, and D. N. Basov, "Tunable phonon polaritons in atomically thin van der Waals crystals of boron nitride," *Science* (80-.). **343**, 1125–1129 (2014).
109. P. Dore, G. De Marzi, and A. Paolone, "Refractive indices of SrTiO₃ in the infrared region," *Int. J. Infrared Millimeter Waves* **18**, 125–138 (1997).
 110. B. Hauer, A. P. Engelhardt, and T. Taubner, "Quasi-analytical model for scattering infrared near-field microscopy on layered systems," *Opt. Express* **20**, 13173 (2012).
 111. S. S. Hong, J. H. Yu, D. Lu, A. F. Marshall, Y. Hikita, Y. Cui, and H. Y. Hwang, "Two-dimensional limit of crystalline order in perovskite membrane films," *Sci. Adv.* **3**, eaao5173 (2017).
 112. V. Dobrosavljevic, N. Trivedi, and J. M. Valles, "Introduction to Metal-Insulator Transitions," in *Conductor-Insulator Quantum Phase Transitions* (2012), pp. 3–58.
 113. T. M. Rice, H. Launois, and J. Pouget, "Comment on "VO₂": Peierls or Mott-Hubbard? A View from Band Theory,"" *Phys. Rev. Lett.* **73**, 3042 (1994).
 114. H. T. Kim, Y. W. Lee, B. J. Kim, B. G. Chae, S. J. Yun, K. Y. Kang, K. J. Han, K. J. Yee, and Y. S. Lim, "Monoclinic and correlated metal phase in VO₂ as evidence of the mott transition: Coherent phonon analysis," *Phys. Rev. Lett.* **97**, 266401 (2006).
 115. J. B. Goodenough, "The two components of the crystallographic transition in VO₂," *J. Solid State Chem.* **3**, 490–500 (1971).
 116. R. M. Wentzcovitch, W. W. Schulz, and P. B. Allen, "VO₂: Peierls or Mott-Hubbard? A view from band theory," *Phys. Rev. Lett.* **72**, 3389–3392 (1994).
 117. Y. H. Matsuda, D. Nakamura, A. Ikeda, S. Takeyama, Y. Suga, H.

- Nakahara, and Y. Muraoka, "Magnetic-field-induced insulator–metal transition in W-doped VO₂ at 500 T," *Nat. Commun.* **11**, 3591 (2020).
118. O. Nájera, M. Civelli, V. Dobrosavljević, and M. J. Rozenberg, "Resolving the VO₂ controversy: Mott mechanism dominates the insulator-to-metal transition," *Phys. Rev. B* **95**, 035113 (2017).
119. C. Weber, D. D. O'Regan, N. D. M. Hine, M. C. Payne, G. Kotliar, and P. B. Littlewood, "Vanadium dioxide: A peierls-mott insulator stable against disorder," *Phys. Rev. Lett.* **108**, 256402 (2012).
120. W. H. Brito, M. C. O. Aguiar, K. Haule, and G. Kotliar, "Metal-Insulator Transition in VO₂: A DFT + DMFT Perspective," *Phys. Rev. Lett.* **117**, 056402 (2016).
121. K. Okazaki, S. Sugai, Y. Muraoka, and Z. Hiroi, "Role of electron-electron and electron-phonon interaction effects in the optical conductivity of VO₂," *Phys. Rev. B - Condens. Matter Mater. Phys.* **73**, 165116 (2006).
122. K. Kawatani, T. Kanki, and H. Tanaka, "Formation mechanism of a microscale domain and effect on transport properties in strained VO₂ thin films on TiO₂ (001)," *Phys. Rev. B - Condens. Matter Mater. Phys.* **90**, 054203 (2014).
123. M. Yang, Y. Yang, B. Hong, L. Wang, K. Hu, Y. Dong, H. Xu, H. Huang, J. Zhao, H. Chen, L. Song, H. Ju, J. Zhu, J. Bao, X. Li, Y. Gu, T. Yang, X. Gao, Z. Luo, and C. Gao, "Suppression of Structural Phase Transition in VO₂ by Epitaxial Strain in Vicinity of Metal-insulator Transition," *Sci. Rep.* **6**, 23119 (2016).
124. J. A. Creeden, S. E. Madaras, D. B. Beringer, M. R. Beebe, I. Novikova, and R. A. Lukaszew, "Structural and Photoelectric Properties of Epitaxially Grown Vanadium Dioxide Thin Films on c-Plane Sapphire and Titanium Dioxide," *Sci. Rep.* **9**, 9362 (2019).

125. R. J. Suess, N. S. Bingham, K. M. Charipar, H. Kim, S. A. Mathews, A. Piqué, and N. A. Charipar, "Ultrafast Phase Transition Dynamics in Strained Vanadium Dioxide Films," *Adv. Mater. Interfaces* **4**, 1700810 (2017).
126. Y. Cho, S. Aritomi, T. Kanki, K. Kinoshita, N. Endo, Y. Kondo, D. Shindo, H. Tanaka, and Y. Murakami, "Morphology of phase-separated VO₂ films deposited on TiO₂-(001) substrate," *Mater. Res. Bull.* (2018).
127. A. X. Gray, J. Jeong, N. P. Aetukuri, P. Granitzka, Z. Chen, R. Kukreja, D. Higley, T. Chase, A. H. Reid, H. Ohldag, M. A. Marcus, A. Scholl, A. T. Young, A. Doran, C. A. Jenkins, P. Shafer, E. Arenholz, M. G. Samant, S. S. P. P. Parkin, and H. A. Dürr, "Correlation-Driven Insulator-Metal Transition in Near-Ideal Vanadium Dioxide Films," *Phys. Rev. Lett.* **116**, 116403 (2016).
128. A. D'Elia, C. Grazioli, A. Cossaro, B. Li, C. Zou, S. J. Rezvani, A. Marcelli, and M. Coreno, "Detection of Spin Polarized Band in VO₂ / TiO₂ (001) Strained Films via Orbital Selective Constant Initial State Spectroscopy," *Condens. Matter* **5**, (2020).
129. A. Sohn, T. Kanki, H. Tanaka, and D. W. Kim, "Visualization of local phase transition behaviors near dislocations in epitaxial VO₂/TiO₂ thin films," *Appl. Phys. Lett.* **107**, 171603 (2015).
130. D. Shiga, M. Minohara, M. Kitamura, R. Yukawa, K. Horiba, and H. Kumigashira, "Emergence of metallic monoclinic states of VO₂ films induced by K deposition," *Phys. Rev. B* **99**, 125120 (2019).
131. Y. Sharma, M. V. Holt, N. Laanait, X. Gao, I. N. Ivanov, L. Collins, C. Sohn, Z. Liao, E. Skoropata, S. V. Kalinin, N. Balke, G. Eres, T. Z. Ward, and H. N. Lee, "Competing phases in epitaxial vanadium dioxide at nanoscale," *APL Mater.* **7**, 081127 (2019).
132. R. Eguchi, M. Taguchi, M. Matsunami, K. Horiba, K. Yamamoto, Y. Ishida,

- A. Chainani, Y. Takata, M. Yabashi, D. Miwa, Y. Nishino, K. Tamasaku, T. Ishikawa, Y. Senba, H. Ohashi, Y. Muraoka, Z. Hiroi, and S. Shin, "Photoemission evidence for a Mott-Hubbard metal-insulator transition in VO₂," *Phys. Rev. B - Condens. Matter Mater. Phys.* **78**, 075115 (2008).
133. S. Kittiwatanakul, S. A. Wolf, and J. Lu, "Large epitaxial bi-axial strain induces a Mott-like phase transition in VO₂," *Appl. Phys. Lett.* **105**, 073112 (2014).
134. H. Paik, J. A. Moyer, T. Spila, J. W. Tashman, J. A. Mundy, E. Freeman, N. Shukla, J. M. Lapano, R. Engel-Herbert, W. Zander, J. Schubert, D. A. Muller, S. Datta, P. Schiffer, and D. G. Schlom, "Transport properties of ultra-thin VO₂ films on (001) TiO₂ grown by reactive molecular-beam epitaxy," *Appl. Phys. Lett.* **107**, 163101 (2015).
135. G. J. Paez, C. N. Singh, M. J. Wahila, K. E. Tirpak, N. F. Quackenbush, S. Sallis, H. Paik, Y. Liang, D. G. Schlom, T.-L. Lee, C. Schlueter, W.-C. Lee, and L. F. J. Piper, "Simultaneous Structural and Electronic Transitions in Epitaxial VO₂ / TiO₂ (001)," *Phys. Rev. Lett.* **124**, 196402 (2020).
136. H. Qiu, M. Yang, Y. Dong, H. Xu, B. Hong, Y. Gu, Y. Yang, C. Zou, Z. Luo, and C. Gao, "The tetragonal-like to rutile structural phase transition in epitaxial VO₂/TiO₂ (001) thick films," *New J. Phys.* **17**, 113016 (2015).
137. M. M. Qazilbash, A. A. Schafgans, K. S. Burch, S. J. Yun, B. G. Chae, B. J. Kim, H. T. Kim, and D. N. Basov, "Electrodynamics of the vanadium oxides V O₂ and V₂ O₃," *Phys. Rev. B - Condens. Matter Mater. Phys.* **77**, 115121 (2008).
138. L. L. Fan, S. Chen, Z. L. Luo, Q. H. Liu, Y. F. Wu, L. Song, D. X. Ji, P. Wang, W. S. Chu, C. Gao, C. W. Zou, and Z. Y. Wu, "Strain dynamics of ultrathin VO₂ film grown on TiO₂(001) and the associated phase transition modulation," *Nano Lett.* **14**, 4036–4043 (2014).
139. M. Dressel and G. Gruner, *Electrodynamics of Solids*, 1st ed. (Cambridge

University Press, 2002).

140. H. W. Verleur, A. S. Barker, and C. N. Berglund, "Optical properties of VO₂ between 0.25 and 5 eV," *Phys. Rev.* **172**, 788–798 (1968).
141. T. J. Huffman, P. Xu, A. J. Hollingshad, M. M. Qazilbash, L. Wang, R. A. Lukaszew, S. Kittiwatanakul, J. Lu, and S. A. Wolf, "Modification of electronic structure in compressively strained vanadium dioxide films," *Phys. Rev. B - Condens. Matter Mater. Phys.* **91**, 205140 (2015).
142. J. Sun and G. K. Pribil, "Analyzing optical properties of thin vanadium oxide films through semiconductor-to-metal phase transition using spectroscopic ellipsometry," *Appl. Surf. Sci.* **421**, 819–823 (2017).
143. R. Krutokhvostov, A. A. Govyadinov, J. M. Stiegler, F. Huth, A. Chuvilin, P. S. Carney, and R. Hillenbrand, "Enhanced resolution in subsurface near-field optical microscopy," *Opt. Express* **20**, 593 (2012).
144. M. M. Qazilbash, K. S. Burch, D. Whisler, D. Shrekenhamer, B. G. Chae, H. T. Kim, and D. N. Basov, "Correlated metallic state of vanadium dioxide," *Phys. Rev. B - Condens. Matter Mater. Phys.* **74**, 205118 (2006).
145. H. T. Kim, M. Kim, A. Sohn, T. Slusar, G. Seo, H. Cheong, and D. W. Kim, "Photoheat-induced Schottky nanojunction and indirect Mott transition in VO₂: Photocurrent analysis," *J. Phys. Condens. Matter* **28**, 085602 (2016).
146. A. Gozar, N. E. Litombe, J. E. Hoffman, and I. Božovi, "Optical Nanoscopy of High-T_c Cuprate Nano-Constriction Devices Patterned by Helium Ion Beams Supplement," *Nano Lett.* 1–7 (2017).
147. L. G. Parratt, "Surface studies of solids by total reflection of x-rays," *Phys. Rev.* **95**, 359–369 (1954).
148. K. Sakurai, M. Mizusawa, and M. Ishii, "Significance of Frequency Analysis in X-ray Reflectivity: Towards analysis which does not depend too much on models," *Trans. Mater. Res. Soc. Japan* **33**, 523–528 (2008).